FISSION IN THE LEAD REGION

By

Adam K. Anthony

A DISSERTATION

Submitted to
Michigan State University
in partial fulfillment of the requirements
for the degree of

Physics—Doctor of Philosophy

2023

ABSTRACT

Since its discovery in the 1930s fission has been a key tool in the quest to better understand nuclear physics. The dynamics of fission depend on the interplay of the nuclear and Coulomb forces. The masses and charges of the resultant fission fragments are driven by the microscopic (quantized) nature of nucleons in the nucleus. Here we explore a new method for measuring fission properties of radioactive nuclei in inverse kinematics using an Active Target (AT) Time Projection Chamber (TPC). The experiment was performed at the National Superconducing Cyclotron Laboratory (NSCL). It measured the He fusion-induced fission of neutron-deficient nuclei in the lead region. We present initial charge (Z) distributions for ^{204}At, the most abundant species measured, at excitation energies less than 52 MeV. A complete analysis of the data from the experiment will provide cross-section and charge distribution measurements along the transition region from symmetric to asymmetric fission in this region of the charge of nuclei.

To facilitate this work, a new beam particle identification system was developed. We call this system the HEavy Isotope Tagger (HEIST). Here we successfully demonstrate the tagging of heavy (Pb-like), incompletely stripped beam particles at ∼ 75 MeV/A. In addition, we also provide measurements of the charge state distributions for some nuclei in the beam. These are compared to the charge state model GLOBAL, where we find good agreement if we adjust the velocity of the beam in the GLOBAL model.

ACKNOWLEDGEMENTS

This will be updated in a future version of this document.

TABLE OF CONTENTS

LIST OF TABLES

LIST OF FIGURES

CHAPTER 1

INTRODUCTION

The purpose of this chapter is to introduce the reader to the topics and physics discussed in the remainder of this thesis. Here we focus on the ideas underlying the physics at the heart of this thesis, rather than on the most detailed description possible. We will begin with a discussion of what is encompassed by the field of nuclear physics. We will then discuss some of the models used to understand nuclei and nuclear matter. Building on that discussion we will turn to fission (the topic of this thesis), how the models introduced earlier can help us understand the fission process, and where those models are inadequate. We end with a discussion about the organization of the rest of the thesis.

Nuclear physics, broadly speaking, is the study of nuclear matter. Nuclear matter is what makes up nearly all the mass of "things" we encounter in our day to day lives (or "ordinary matter"). This, incidentally, is not actually where most of the mass in the universe is located. Astrophysical measurements have allowed us to estimate that the universe is composed $\sim 68\%$ dark energy and $\sim 27\%$ dark energy, with only 5% being the ordinary matter we are familiar with. Anything that we have personal experience with (any object, star, planet, person, cell, etc.) is composed of ordinary matter. This in turn is composed of atoms, which contain a dense central core of nuclear matter surrounded by a cloud of electrons. The dense core we call a nucleus. Despite being a fraction of the total size of an atom, the nucleus contains more than 99.9% of the mass of an atom. If you were to take an atom and blow it up to the size of an American football field, the nucleus would be about the size of a pea, with the rest of the space empty except for the orbiting electrons. The nucleus is itself composed of two types of particles which we call nucleons, protons and neutrons. The two varieties of nucleons are very similar expect for their electric charge where protons have a positive charge equal in magnitude to the charge of an electron, and neutrons, as their name suggests, are electrically neutral. These nucleons themselves are composed of particles in the Standard Model (namely quarks and gluons); however, the substructure of nucleons is not important at the energies typically studied in nuclear physics.

Much like nuclear physics is the study of nuclear matter and its interactions, chemistry is the study of atoms and their interactions (mediated through the electron cloud). Chemistry is primarily a study of charge and the force that acts on charge, the Coulomb force. What matters in chemistry is the charge of the atom, determined by the number of protons. Atoms with different number of protons (the number of protons is typically denoted Z), are said to be different elements. The periodic table is a chemist's map to the elements. One can deduce some of the expected chemical properties of an element based on its location on the table. The location of an element on the table is related to the discretized nature of the energies the orbiting electrons. For example, elements in the far right group, the Noble Gasses, are remarkably stable and react with very little. These elements correspond to those where an electron "shell" is fully filled.

Unsurprisingly then, the number of electrons orbiting the nucleus is important in understanding its chemistry. We denote this piece of information by discussion the atom's total charge, also called its charge state. Because protons and electrons have the same charge, just opposite sign we say the charge state of an atom is equal to the number of protons, Z, minus the number of orbiting electrons, N_e. There is a particular way we write this information. We express the information on the element type by its 2-letter abbreviation, and its charge state as a superscript to the right of the element type. For example, to describe lead atoms (Z = 82) with 81 electrons orbiting we would write Pb^{1+}.

When we move from the study of chemistry to the study of nuclear matter, we now care about more than just the charge of the nucleus (or number of protons). Of equal importance is the number of neutrons in the nucleus. The reasons for this will become clear soon. Just like we denote the number of electrons orbiting the nucleus by the total charge of the atom, we denote the number of neutrons in the nucleus, N, by the the total mass of the nucleus, A, where $A = N + Z$. This is written also as a subscript, but to the left of the element abbreviation. So if we were to take the sample of a lead atom with 81 electrons, and specify it has 126 neutrons, then we would denote that $^{208}Pb^{1+}$. We call atoms, or nuclei, of the same element but different numbers of neutrons different isotopes of an element.

Much like the periodic table is the map of elements for chemists, the chart of nuclei is the map of nuclei for nuclear physicists. The chart (Fig. 1.1) has two dimensions, the number of protons on along the y-axis and the number of neutrons along the x-axis. Each box then describes a specific isotope. Much like how on the periodic table the far right group corresponds to atoms with a closed electron shell, the blue and black bands across the chart indicate closed shells for protons and neutrons, respectively. We can very broadly classify nuclei into two groups: 1)those that are stable (black boxes in Fig. 1.1) and 2) those that are unstable, or radioactive (all non-black boxes in Fig. 1.1).
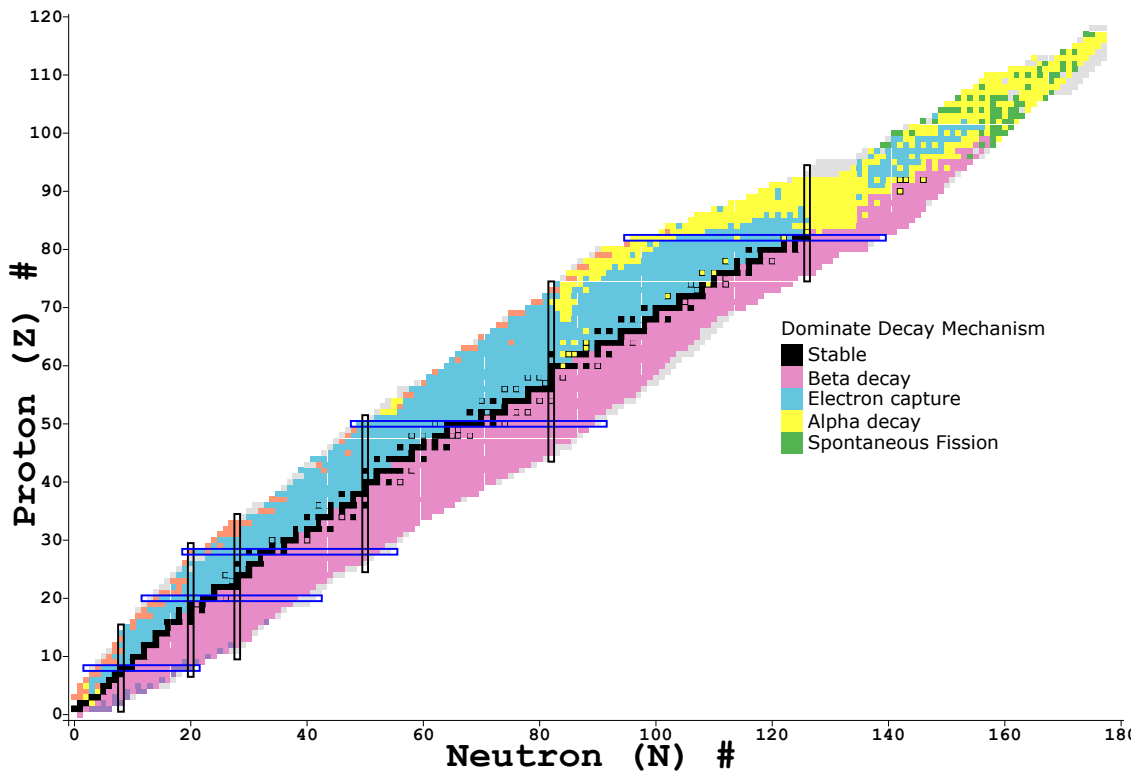
Figure 1.1 Chart of nuclei where isotopes are colored by the dominate decay mode. The blue and black rectangles along certain values of Z and N denote the "magic numbers", or closed shells. Data from [1].

Stable isotopes are those whose identity does not change over time. If you place a pile of ^{208}Pb on a table and check back in a billion years it will still be a pile of ^{208}Pb. This is in contrast to unstable nuclei which can spontaneously change into different isotopes through different decay mechanisms. If you were to instead place a pile of ^{209}Pb on a table and check back even a day later,

you would find you now had a pile of ^{209}Bi, another stable isotope. The mechanisms by which this transformation can occur are varied, but there are four we will focus on as examples as they all crop up later in the discussion.

The first, and most common decay mechanism is beta decay. In this process an electron (also called a beta particle for historical reasons) is emitted from the nucleus along with an anti-neutrino (which has no charge and so little mass we will neglect mentioning it again). As the electron is emitted a proton is converted into a neutron changing the isotope (and element) of the nucleus. The second decay mechanism of importance is alpha decay. In this mechanism an alpha particle (another name for ^{4}He^{2+}) is emitted from the nucleus. The third mechanism is neutron decay. Here a single neutron is emitted from the nucleus, changing the isotope of the nucleus. Unlike the other decay mechanisms discussed, the element of the isotope remains unchanged. The final decay mechanism, and the one we will focus on the most, is fission. In this process, a single heavy nucleus splits into two daughter nuclei of roughly equal mass. There are some, very heavy, nuclei where this process can happen spontaneously. We will primarily focus on induced fission where energy must be put into the system before the nucleus can decay via fission.

So what is it that determines which of these (or any other decay process) an unstable nucleus will undergo? The answer lies in what reactions are energetically favorable, or in other words which reactions will release energy. To understand that in more detail we will turn to describing the energy "stored" in a nucleus by the forces that bind it together, or the binding energy of a nucleus.

1.1   Nuclear binding energy and the Liquid Drop Model

The binding energy of a nucleus is the amount of energy that goes into holding the constituent nucleons together. Another way to state that is the binding energy is the energy released when the constituent nucleons are brought together and a single nucleus is formed. We can define the binding energy, BE, by comparing the mass of the nucleus to the mass of its constituent parts:

$$BE = N * M(^{1}n) + Z * M(^{1}H^{1+}) - M(nucleus) \tag{1.1}$$

where N is the number of neutrons in the isotope, Z is the number of protons, $M(^1n)$ is the mass of a bare neutron, $M(^1H^{1+})$ is the mass of a bare proton, and M(nucleus) is the mass of the nucleus. Here we are being a little loose with units, typically we measure mass in either atomic mass units (amu) or MeV/c^2, where c is the speed of light.

Because the binding energy of a nucleus scales with the total number of nucleus, a more useful measure is often the binding energy per nucleon or BE/A. This is plotted in Fig. 1.2. The BE/A curve peaks at ^{56}Fe, nuclei to the left of this peak (lower mass number) can fuse and have that process be energetically favorable. Nuclei to the right of that peak (higher mass number) can fission and have that process be energetically favorable.
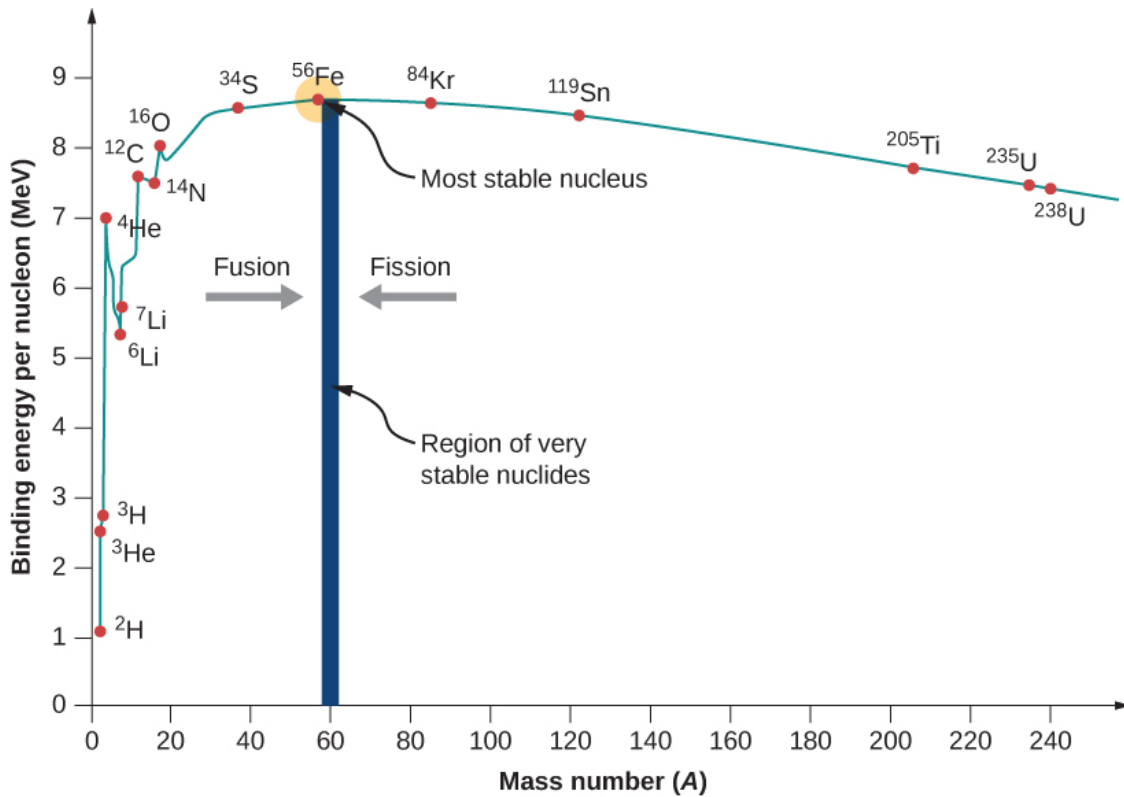
Figure 1.2 Figure showing the binding energy per nucleon and marking the regions where fusion and fission are energetically favorable. Figure from [2].

The first real model for the nucleus and its binding energy came in the 1930s and was initially proposed by Gammow [3], known as the liquid drop model (LDM) of the nucleus. The model was refined and quantified by Weizsäcker and Bethe into the Semi-Empirical Mass Formula (SEMF) in

1935 [4] and remains a useful model of the nucleus to this day.

The LDM considers the nucleus to be a dense, incompressible charged fluid held together by the strong nuclear force. When considering the model, it is important to keep the two forces acting on the liquid in mind. The first force is the nuclear force, a highly attractive force but with a very short range and a hard, repulsive "core". We assume this force treats protons and neutrons the same and is attractive regardless of electric charge. The second force is the long-range Coulomb force which only acts on the positively charged protons. The potentials arising from these two forces for two protons treated as point particles, along with their sum, are plotted in Fig. 1.3. To understand if the potential would lead to an attractive or repulsive force, consider the potential as a track that one can place a ball on. The direction the ball would roll is the same as the direction the proton would travel in that potential. Within ~ 2.5 fm the nuclear force dominates. At larger distances (> 10 fm) the Coulomb force dominates and the nuclear potential is essentially zero.
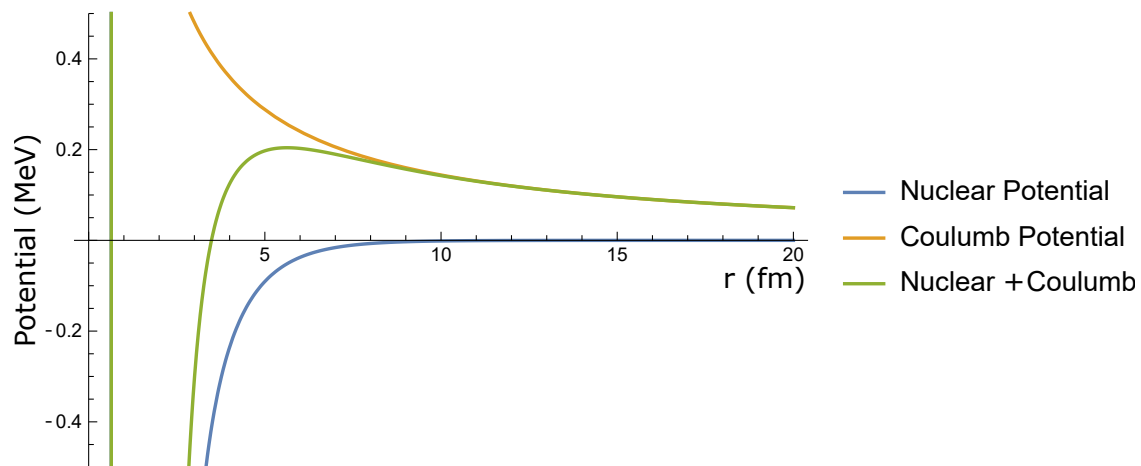
Figure 1.3 Nuclear and Coulomb potential for two protons treated as point particles. At short range, the nuclear potential dominates, and at long range the Coulomb potential dominates.

When trying to model the binding energy of the nucleus in this model, we will start by considering the binding energy for the strong force in an infinite nuclear matter. In this case, each nucleon has some average number of neighboring nucleons that are close enough to be in the attractive well from the nuclear force. Each nucleon then provides the same amount of average

binding energy. We call this the volume term, BE_{vol}:

$$BE_{vol} = \alpha_{vol}A \tag{1.2}$$

where α_{vol} is a constant describing the average binding energy from the nuclear force per nucleon, and A is the number of nucleons in the nucleus.

A nucleus, however, is not infinite and the nucleons on the surface have fewer neighbors on average than the nucleons in the interior. This means our BE_{vol} term is an overestimation of the total binding energy arising from the nuclear force and we need to reduce it by some factor proportional to the surface area of the nucleus. If we assume the nucleus is a sphere, than the surface area will scale as $A^{2/3}$ so we write the correction term (called the surface term) as:

$$BE_{surf} = -\alpha_{surf}A^{2/3} \tag{1.3}$$

These two terms account for the binding energy from the nuclear force. The other force as play here is the Coulomb force, which acts just on the protons unlike the nuclear force. In addition, the Coulomb force is long range, so each proton will "feel" every other proton in the nucleus. The reduction in the binding energy due to the Coulomb force (called the Coulomb term) is given by:

$$BE_{coul} = -\alpha_{coul}\frac{Z(Z-1)}{A^{1/3}} \tag{1.4}$$

There are two additional terms included in the SEMF. Unlike the previous terms, they don't arise from the forces acting on the nucleons but instead from quantum mechanical effects. The first is often called the Pauli, or asymmetry, term. Fundamentally it arises from the Pauli exclusion principle. If there is an imbalance in the number of protons and neutrons in the nucleus, then the more abundant species of nucleon must be at a higher energy level, on average. These "excess" neutrons or protons then decrease the total binding energy of the nucleus. In addition to the Pauli exclusion principle, there is a component to the asymmetry term coming from nuclear interactions. This, rather confusingly, is called the symmetry energy and it becomes very important in systems dominated by a single species such as neutron starts and heavy neutron rich nuclei. Understanding

the symmetry energy is critical to understanding these systems. We write the asymmetry term as:

$$BE_{asym} = -\alpha_{asym}\frac{(N-Z)^2}{A}$$ (1.5)

The second term accounts for pairing effects. Two nucleons with anti-aligned spin occupy a lower energy level than two nucleons with an aligned spin. That is, there is an energetic preference for both neutrons and protons to be paired. The magnitude of this effect is the same for both protons and neutrons. As a result this pairing correction, often denoted $\delta(N, Z)$ is given by:

$$\delta(N, Z) = \begin{cases} +\delta_0 & \text{even Z, N (even A)} \\ 0 & \text{odd A} \\ -\delta_0 & \text{odd Z, N (even A)} \end{cases}$$ (1.6)

where δ_0 is the difference in energy between paired and unpaired nucleons.

Putting all of these terms together we get the modern SEMF:

$$BE(N, Z) = \alpha_{vol}A - \alpha_{surf}A^{2/3} - \alpha_{coul}\frac{Z(Z-1)}{A^{1/3}} - \alpha_{asym}\frac{(N-Z)^2}{A} + \delta(N, Z)$$ (1.7)

The terms in this expression are visualized in Fig. 1.4. The coefficients are extracted by fitting Eqn. 1.7 to the measured masses of nuclei.
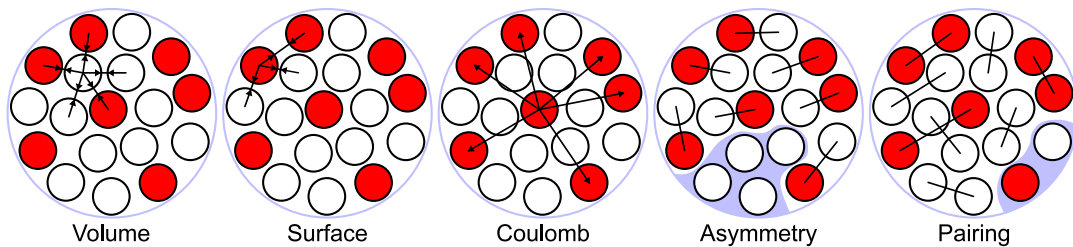
Figure 1.4 Illustration of the various terms in the semi-empirical mass formula. Figure from [5].

1.2 Fission: A story of deformation

The LDM provides the first model of the nucleus that allows us to begin to understand the physics underpinning fission. The LDM, as described above, models the binding energy of a spherical nucleus. Nuclei undergoing fission deform, stretching along the fission axis until the

Coulomb repulsion between the two daughter fragments can overcome the nuclear force holding everything together. At that point the nucleus splits (called the scission point) and the two daughter nuclei are repelled by the Coulomb force. We can understand this quantitatively by examining how the terms in the SEMF change as a function of deformation.

The fist thing to define is what we mean by deformation. In this example, we will examine the leading order perturbation for an axially symmetric distortion which can be written as:

$$R(\theta) = R_0[1 + \alpha_2 P_2(\cos\theta)] \tag{1.8}$$

where α_2 describes the amount of quadruple deformation, P_2 is the second Legendre polynomial, and R_0 is the radius of the undistorted spherical nucleus.

This distortion will primarily effect two terms in the SEMF. First is the term relating to the surface energy (Eqn. 1.3). As the nucleus becomes distorted the surface area increases, increasing the magnitude of BE_{surf} and decreasing the total binding. The second term effected is the Coulomb term (Eqn. 1.4). As the nucleus stretches the protons become, on average, further apart decreasing the magnitude of BE_{Coul}. As a result, the total binding energy increases.

Through an accident of nature, the magnitude of the change of these two terms, one increasing the total binding energy and the other decreasing the total binding energy, are almost the same. In this model, the sum of these terms is the potential energy surface (PES) of the nucleus, or how the energy of the nucleus changes as it is deformed. This is seen in Fig. 1.5 where the change in the two terms, as well as the change in the PES are plotted. We call the maximum value along the PES the fission barrier, and the point at which it occurs the saddle point (or saddle configuration). If the nucleus reaches the saddle configuration then fission will occur. Classically, the excitation energy of the nucleus has to be above the barrier for the nucleus to reach the saddle configuration. The higher the excitation energy above the barrier, the more likely fission is to occur (compared to another decay channel like neutron emission).

9
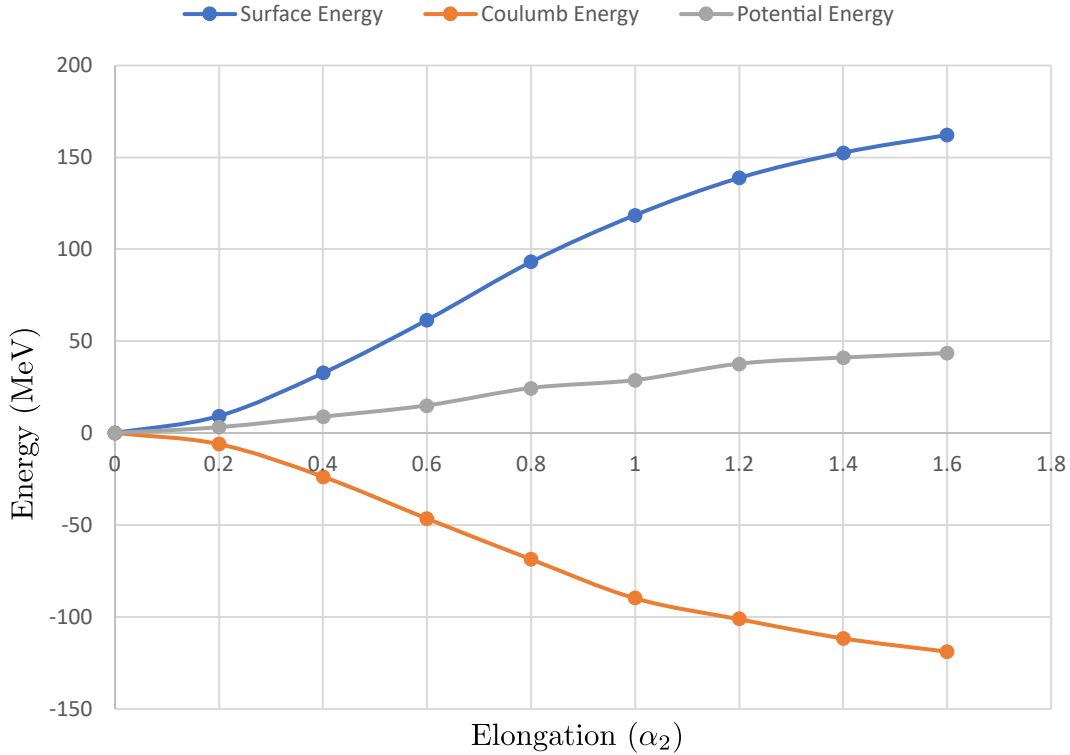
Figure 1.5 Plotted are the change in the Surface and Coulomb terms of the SEMF as a function of increasing quadruple deformation for ^{204}At. The changes almost exactly cancel leading to an increase in the potential energy of the nucleus on the order of 10s of MeV.

1.2.1 Fission fragment asymmetry: deviating from the LDM

The models discussed so far have a glaring omission. They fail to account for the quantum nature of the nucleus which, it turns out, is the driving force behind the resulting mass distribution of the fission fragments.

The LDM discussed above predict that a fissioning nucleus would split symmetrically. From the very first experimental observation of fission by Hahn and Strassman [6] we have known that the mass of the fission fragments can be distributed asymmetrically with one heavy fragment and one light fragment. In the actinide region, it was initially theorized that one can understand the mass asymmetry as being driven by ^{132}Sn, which has both a closed shell of neutrons and protons. This then forms the "core" of the heavier fragment. These closed shells are analogous to the tightly bound and unreactive Nobel Gases. A later description of physics underlying the asymmetry in the actinides was provided by Gustafsson et. al.[7] which relies on the coupling of neutron orbitals in

the deformed nucleus.

It was also observed that nuclei lighter than the actinides would predominantly fission symmetrically. It was long believed that all of these lighter nuclei would fission symmetrically. This prediction proved to be false. Data from the fission of ^{180}Hg showed a dramatic asymmetry in the masses of the fission fragments [8]. This was particularly startling given our understanding up to this point of what drives the mass asymmetry of fission fragments. In the actinide region, the asymmetry is driven by the shell structure of the fission fragments. In the case of ^{180}Hg, a symmetric split would lead to two ^{90}Zr as the daughter fragments which have a closed shell of neutrons. Applying our model for what drives the asymmetry of the fission fragments in the actinide region, we would expect the fission to be symmetric.

This discovery set off a flurry of theoretical work to understand what was driving the observed asymmetry in this region of the chart of nuclei. The consensus that has arisen from this body of work is the asymmetry is driven by shell effects pre-sission [9, 10, 11, 12]. That is, it is the shell effects of the deformed nucleus, and how the shell structure changes as the nucleus deforms (but before it splits) that drives the asymmetry, rather than the shell effects of the daughter nuclei. Building on the proposed explanation for the mass asymmetry in the actinides as being due to coupling of neutron orbitals [7], Ichikawa and Moller point out that the asymmetry in this region could also be due to analogous couplings and not a novel mechanism [13].

Work has been done to calculate the expected asymmetry of the mass distribution of the fission fragments for a broad swath of the chart of nuclei, shown in Fig. 1.6 [14]. The basis of these calculation is predicting the PES surface for nuclei in a higher dimensional space where deformations beyond just a quadruple deformation are explored. The calculations predict a region of asymmetric fission around ^{180}Hg. At the time of the calculations (2014) there were only a few experimental measurements to compare to. The calculations agree with some of the available high statistics measurements, although the authors believed there may be discrepancies along the transition region from symmetric to asymmetric fission.

This thesis focuses on a novel experiment to measure the charge (Z) distribution of the fission
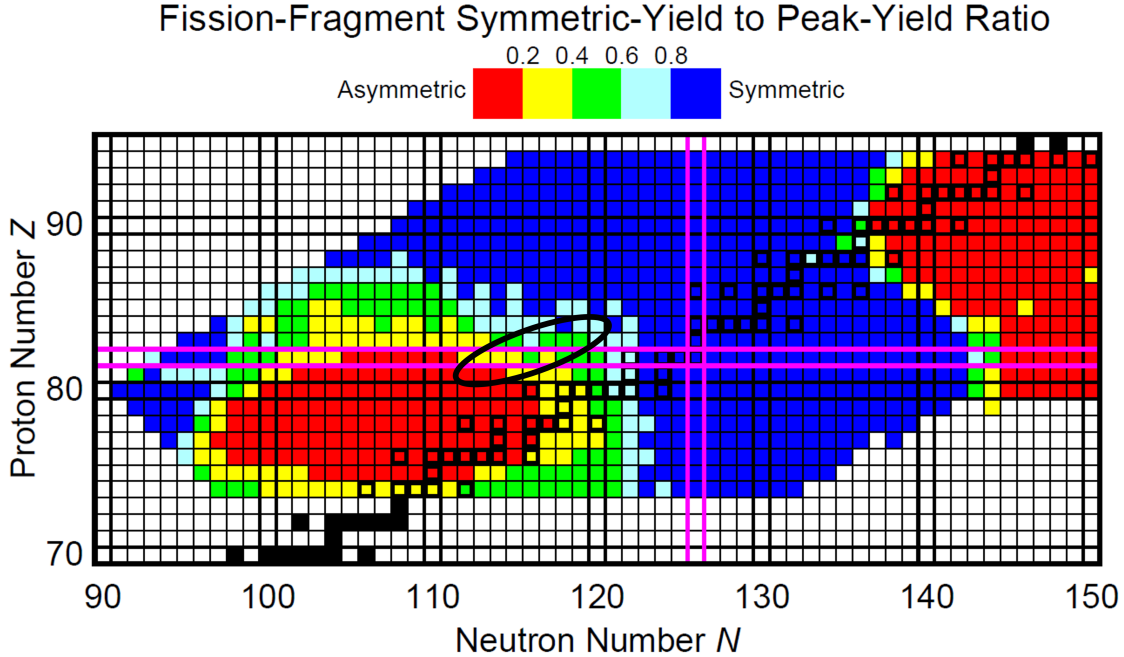
Figure 1.6 Chart of nuclei where nuclei are colored according to theoretical calculations for the expected mass asymmetry of the fission fragments. Red is more asymmetric and blue is more symmetric. Figure from [14].

fragments for nuclei in that transition region. It uses fusion-induced fission using inverse-kinematics with a rare isotope beam. The experiment captured the region of the chart of nuclei indicated by the black oval in Fig. 1.6. We will focus in particular on the fission of ^{204}At, the nuclei where we have the highest statistics. Previous measurements have been made of the charge distribution of neighboring nuclei ^{205}At and ^{206}At [15], allowing us to validate our novel experimental method.

1.3 Thesis Organization

The body of this thesis is split into three main chapters. The first (Sec. 2) deals with the development of the rare isotope beam used in the experiment, along with the development and commissioning of a new detector system (HEIST) to identify the beam on an event-by-event basis. The second chapter (Sec. 3) introduces Active-Target Time Projection Chambers (TPCs) and the analysis techniques used to analyze and simulate data for that class of detector. The third chapter (Sec. 4) details the experiment and the analysis techniques developed to extract charge distributions from energy loss in the TPC, along with the measured charge distribution of ^{204}At. Finally a summary and future outlook is given in the final chapter (Sec. 5).

CHAPTER 2

IDENTIFYING RARE ISOTOPE BEAMS - HEIST

2.1 Identification of rare isotope beams at the NSCL

In order to measure the fission proprieties of unstable nuclei in inverse kinematics a rare isotope beam must be produced and identified on an event by event basis. This work was performed at the NSCL where there was limited experience with beams of this mass, the only previous experiment using a ^{208}Pb beam studied production yields in the fragmentation process [16]. The methods and devices typically used to identify beam species on an event-by-event basis, i.e. particle identification (PID), would not have been sufficient to uniquely identify the beam species at the required energy.

For many beams and fragment separators, an appropriate choice of separator settings can remove most unwanted ions in the beam. Measuring the time of flight (ToF) from the fragment separator to the experimental setup can then allow the remaining rare isotopes in the beam to be uniquely identified (i.e. tagged). Such identification becomes more difficult when these secondary beams are heavy and the beam particles have overlapping velocity distributions. In this case, a ToF measurement is not sufficient to resolve the beam species. Beam species can still be distinguished by an additional measurement of the energy deposited in an ion chamber, ΔE. The mass region where overlapping velocity distributions become a problem is heavily dependent on the specifics of a given experiment, depending on the energy of the beam and the materials, if any, that are used to degrade the beam, and the specific setting of the fragment separator.

Heavy beams are routinely tagged by this ΔE-ToF-Bρ method at the RIBF [17] and GSI [18] facilities. At those facilities, beams energies are $E/A \geq 200$ MeV, and beam ions are often fully stripped. Slower beams, where the ions are not fully stripped complicate the picture. At the energy regime of interest, $E/A \approx 74$ MeV, such heavy ions typically retain both their 1s electrons, making them "helium-like" nuclei with Q/e = Z-2, but with non-negligible probabilities for them to be "lithium-like" ions with Q/e = Z-3 or "hydrogen-like" with Q/e = Z-1. We chose to perform the separation and tagging of the beam at the highest energy possible at the NSCL to minimize the charge state problem. Following the identification of the beam, the energy can then be degraded

at the experimental setup to the energy required to make a meaningful measurement of the fission properties of the nuclei. The HEavy ISotope Tagger (HEIST) was developed to tag and track secondary projectile fragments at energies where ions are not fully stripped.

HEIST was coupled to the A1900 fragment separator [19] at the NSCL and consists of three distinct detector systems described in detail in Sec 2.3. The detector systems are: a time of flight (ToF) system composed of two micro-channel plates (MCPs), a Multi-Sampling Ionization Chamber (MUSIC) that provides beam tracking and energy loss (ΔE) information, and a high-purity Ge (HPGe) crystal used to detect isomer γ-rays. The physical locations of the detectors and our experimental end station, the Active-Target Time Projection Chamber (AT-TPC) [20] that we used to measure fission (see Sec 4), are shown schematically in Fig. 2.1. The location of the first MCP (MCP1) at the A1900 focal plane is shown in Fig. 2.2.
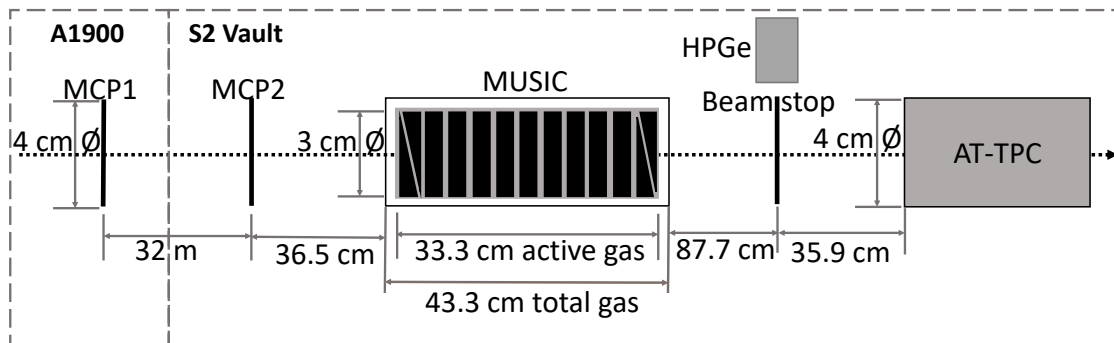
Figure 2.1 Detector locations along the beamline. Not to scale.

2.2 Beam production and separation with A1900

2.2.1 A1900 Setup

At the Coupled Cyclotron Facility (CCF) of the NSCL [21, 19], a primary ^{208}Pb beam was accelerated first in the K500 Cyclotron, striped and injected into the K1200 Cyclotron where it was accelerated to its final energy of E/A = 85 MeV. Rare isotopes were then produced by bombarding the ^{208}Pb^{+63} beam on a ^{9}Be production target, with an areal density of 22.5 mg/cm^2, located outside of the K1200 Cyclotron [19]. This produces a mixture of primary and secondary beams that enter the A1900 fragment separator [19], shown in Fig. 2.2.

The unreacted primary beam is outside the $B\rho$ acceptance of the A1900, and so is not transmitted

14

A1900 Fragment Separator
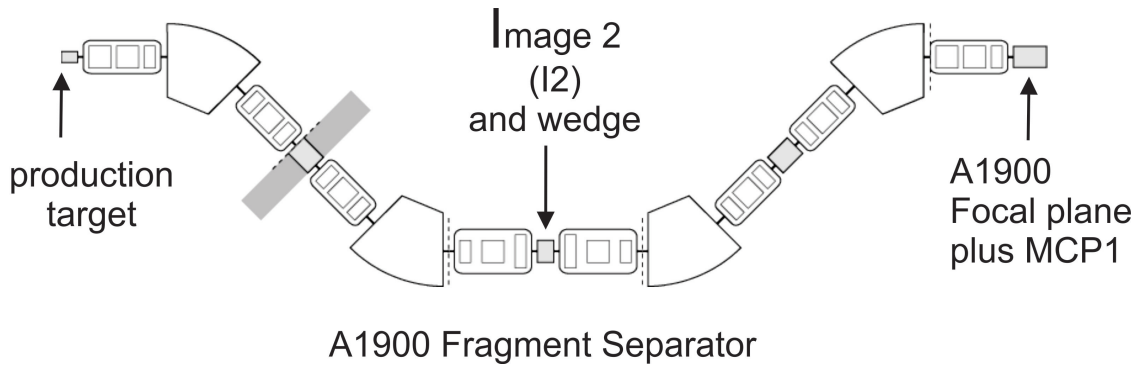
Figure 2.2 A1900 Fragment Separator: The locations of the production target, Image 2 dispersive focus and the 1900 focal plane are shown.

through the fragment separator. Midway through the A1900 magnetic separator, there is a dispersive focus at Image2 (I2) where the beam particles are focused to different points depending on their rigidity. Using a set of thin narrow slits at I2 to define a 2 mm aperture, we selected ions that have a magnetic rigidity of $B\rho$ = 3.271 Tm with a precision of ± 0.035%. This rigidity transmits ^{192}Hg ions with Q/e = 77 at an energy of E/A = 79.7 MeV, as well as other ions with a similar rigidity.

The isotopic selection was improved by passing the remaining ions through a 23.5 mg/cm^2 Polyimide foil to degrade the energy. Ions with different atomic numbers emerge from the foil with different rigidities [19]; slits at the second dispersive focus at the A1900 focal plane removed unwanted ions with magnetic rigidities that differ from the desired rare isotope [19]. This second set of slits was set to select particles with rigidity of $B\rho$ = 3.117 Tm ± 0.18% corresponding to ^{192}Hg ions with a charge of Q/e = 78 and energy of E/A = 74.4 MeV. Any other ions with a magnetic rigidity in the acceptance of the slits is also transmitted down the beamline to the experimental setup with the same energy.

The selected isotopes then pass through the first MCP (MCP1) that served as a start detector for the ToF system and go on to the second MCP (MCP2), placed 32 m downstream of MCP1 that served as the stop detector, as shown in Fig. 2.1. Using the two MCPs we measured the ToF and the velocity of the beam particles before they passed into the MUSIC detector and the AT-TPC.

2.2.2 PID through ΔE-ToF-Bρ Method

The momentum cut at the dispersive focus of the A1900 separator is related to the A1900 rigidity setting, the beam momentum, beam charge and mass as follows:

$$B\rho = \frac{p}{q} \simeq \frac{mv}{q},$$

(2.1)

Here p is momentum, q is charge, m is mass, and v is velocity. The energy loss of a charged particle through a material, ΔE, is related to its velocity and atomic number by

$$\Delta E \approx C\frac{Z^2}{v^2}f(v)\,,$$

(2.2)

where $f(v)$ is a slowly varying function of the velocity v [22].

Combining the energy loss in the ion chamber, ΔE, with the velocity determined by ToF provides uniquely the atomic number, Z, via Eq. 2. Combining the velocity with the magnetic rigidity via Eq. 1 provides the ratio of mass to charge. For reactions where only one charge state is present for each isotope, this allows a unique determination of the mass and atomic numbers of each particle. For slower heavy fragments where multiple charges are probable, one can take guidance from calculations of the charge state distributions and beam optics calculations that indicate where each charge state should appear in the particle identification (PID) spectrum. In Sec. 2.5.3, we test these charge state models via measurements of characteristic isomer fed γ-rays that uniquely identify the beam fragment independent of charge states.

2.2.3 A1900 Simulation

To design HEIST, we modeled its performance with the LISE++ beam simulation program [23]. The width of the I_2 slit was optimized by considering the trade-off between momentum resolution and beam rate. The rms time resolution δt of an MCP can be estimated by the relationship $\delta t = \tau_{rise}V_{noise}/V_{signal}$ where τ_{rise} is the rise time of the MCP anode signal, V_{noise} is the rms noise and V_{signal} is the amplitude of the MCP anode signal. From this we estimated that we could achieve a FWHM time of flight resolution of about 300 to 400 ps. Allowing for different path lengths for different ions, we conservatively estimated a time resolution of 500 ps could be achieved. LISE

predicted the energy loss straggling in the MUSIC with 300 torr CF_4 to be somewhat less than 0.7% (FWHM). Using the software package SRIM/TRIM [24], we calculated that an energy loss resolution of 0.85 % (FWHM) could be achieved. The energy straggling in the entrance window of the MUSIC is negligible compared to the momentum resolution of the beam and the energy loss straggling in the detector gas.
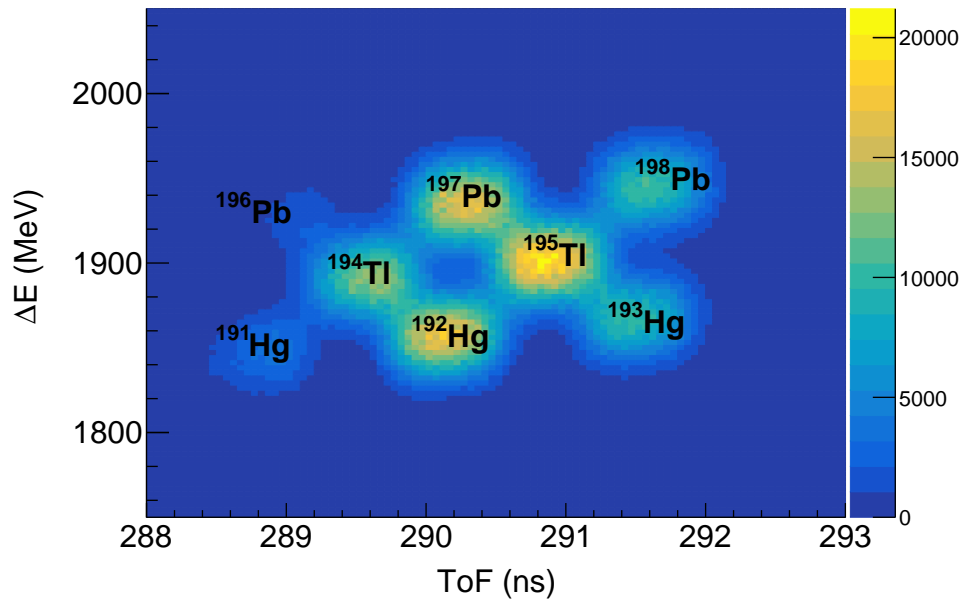
Figure 2.3 The LISE++ simulated PID of several secondary beam isotopes. The charge states are helium-like.

The beam optics and detector response were simulated with LISE++ to determine our predicted ability to successfully identify beam particles. Fig. 2.3 shows the ΔE vs ToF PID plot simulated with LISE++ assuming the A1900 configuration discussed in Sec. 2.2.1. The energy loss plotted is for the entire active volume of the MUSIC detector. For the simulation, we assumed a conservative ΔE resolutions of 2 % (FWHM), significantly larger than the pure energy straggling calculations made with SRIM or LISE++, to include fluctuations from secondary effects, such as high energy delta electrons that escape the detector volume. With these assumptions, we predicted that the various isotopes in the beam could be adequately resolved.

2.3 HEIST construction and operation

2.3.1 MCP

The timing detector was based on a thin emitting foil, 0.5 μm polypropylene, placed along the path of the beam with an MCP readout. These MCPs provide excellent timing resolution and can operate at a rate exceeding 1 MHz without damage. Using thin foils avoids unnecessary degradation of the beam emmittance.

The design of both MCP timing detectors is similar to that described in Refs. [25, 26]. Fig. 2.4 illustrates the design and operating principles of this MCP timing detector. When a beam particle passes through the thin foil, electrons are released by ionizing atoms and then accelerated away from the foil by a static electric field. The trajectories of the electrons are bent by electric and magnetic fields through an angle of 180° so that they hit a stack of 40 mm diameter MCP electron amplifiers produced by Photonis. The two MCPs in the stack are arranged front to back in a chevron configuration to multiply the primary ionization electrons by a gain factor of approximately 10^6. The amplified charges are collected onto an anode plate located behind the MCP. The multiplication process in the MCP is fast, and the corresponding signals have a rise time of about 3 ns.

A series of electrodes, shown by the dashed black lines in Fig. 2.4, are connected with a resistor chain. When biased, they generate the electric field that, in conjuncture with a permanent magnetic field, bends the electrons. The highest potential electrode was biased to $V_{E-field} \approx 2$ kV. The permanent magnetic field is generated by attaching high-field, permanent neodymium magnets on two nickel-plated iron plates that sandwich the MCP detectors. The locations of the permanent magnets were positioned so that the magnetic field is approximately 100 G and uniform to within 2 % over the electron trajectories. In addition, a -1 kV bias is applied to the foil and a positive bias of $V_{mcp} \approx 2.5$ kV is applied to the MCPs and anode.

For the heavy beams used in the experiment the efficiency of the MCP detector was expected to be nearly 100%. Because MCP2 was used as the trigger, only the efficiency of MCP1 can be directly measured. Using the primary beams discussed in Sec. 2.4, the efficiency of the MCP was determined to be 98.6% with no dependence on the beam energy. We determined the efficiency by

18
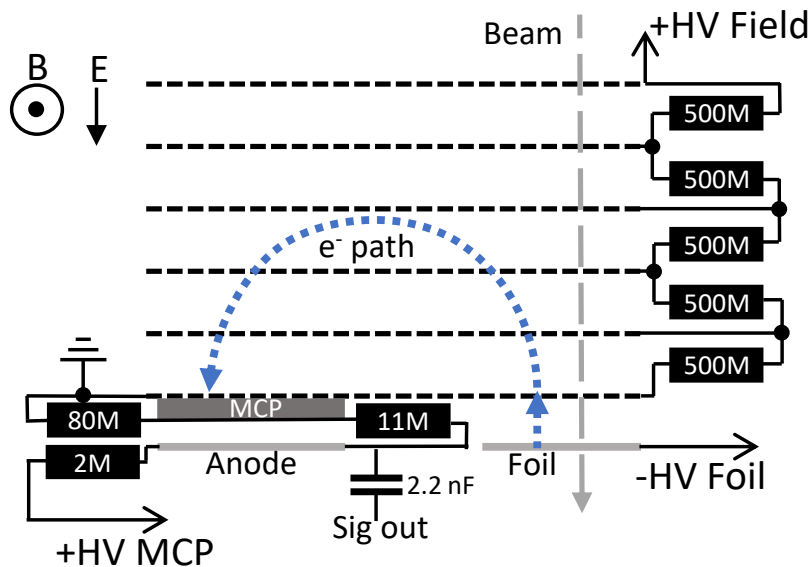
Figure 2.4 (Color online) Drawing of the working principle of the MCP detector. The figure is not drawn to scale.

comparing the number of events with an MCP1 signal to those events with a valid MUSIC energy signal.

No efforts were devoted during the experiment to try to optimize the efficiency. We did not observe any dependence of the efficiency on the energy of the fragment.

Signals from the anode were amplified using a non-inverting fast amplifier (Ortec FTA820A) that amplifies the signals by a factor of 200. The signals were then discriminated using a constant fraction discriminator (Canberra 454) and passed to a TDC (Caen 1190). The signals from MCP1 at the A1900 focal plane were discriminated near the detector, and then sent to the S2 vault at the NSCL where MCP2, the MUSIC, and the TDC to digitize the signals were located.

2.3.2 MUSIC

2.3.2.1 Mechanical Design

The MUSIC detector was constructed to measure the energy loss of the secondary beam particles. Fig. 2.1 shows an overview indicating the horizontal dimensions of the MUSIC chamber
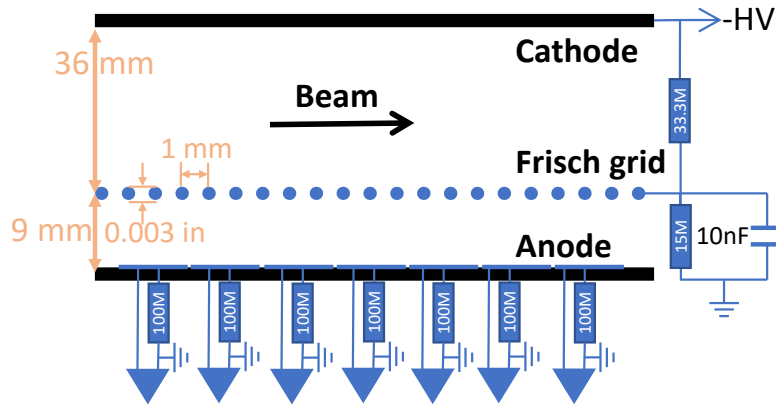
(a) MUSIC schematic
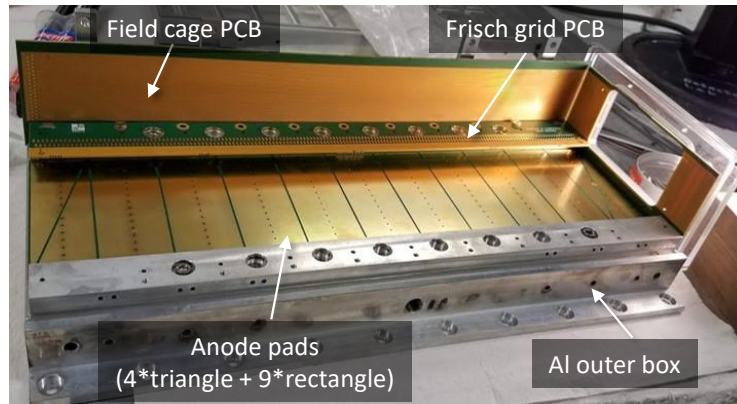
(b) MUSIC picture

Figure 2.5 (Color online) The MUSIC used in this experiment. (a) shows a schematic of MUSIC detector, not to scale. (b) is a photo of the MUSIC during construction. The first two and last two segments are triangular pads used for measuring beam position within the chamber via charge division.

and the physical layout of the anode pads of the MUSIC chamber. Fig. 2.5a shows a schematic side view of the MUSIC chamber indicating the orientation of the anode electrodes, Frisch grid, and cathode. This MUSIC detector is loosely based on the MUSIC80 design employed at GSI to measure the energy loss of heavy beam particles [27].

Fig. 2.5b is a photograph of the inside of the MUSIC taken during construction and the anode structure is visible. The MUSIC detector has an active area of 62 mm × 36 mm and an active length of 333 mm. The anode (333 mm × 84 mm), and cathode (333 mm × 128 mm) are both printed circuit boards (PCBs), mounted onto aluminum plates that are held parallel to each other and separated by 45 mm. The anode PCB is smaller due to the width of the spacer used to mount the Frisch grid PCB. The active area of the detector is further reduced by the Frisch grid PCB extending

10 mm past the edge of the spacer to allow for electrical connections. Both the reduction from the spacer, and Frisch grid PCB can be seen in Fig. 2.5b. The PCBs in this detector were fabricated with a 1.6 mm thick halogen free substrate, IT-170RGA1 and their 1oz copper electrode surfaces were coated with Electroless Nickel Immersion Gold (ENIG) plating. The cathode consists of a single conducting (332 mm × 127 mm) pad.

The anode is split into 9 rectangular segments, with two additional anode segments (the first and the last) that are subdivided into pairs of triangle pads resulting in a total of 13 pads, as shown in Fig. 2.1 and 2.5b. The rectangular middle nine anode segments are 30 mm × 82 mm conducting surfaces separated from each other by 1 mm insulating gaps. The triangular pads (24 mm × 82 mm) provide information about the horizontal beam positions near the entrance and exit of the chamber using the technique of charge division. The beam tracking capabilities of the detector are discussed in detail in Sec. 2.3.2.3.

Each of the thirteen anode pads were individually amplified via Zepto Systems CSA-60-100 charge sensitive preamplifiers and a programmable spectroscopy amplifier (CAEN n568). The slow output from the spectroscopy amplifier is digitized by a peak sensing ADC (Mesytec MACD-32). The fast output from the spectroscopy amplifier was discriminated using a leading edge discriminator (Philips 7106) and digitized using a TDC (CAEN V1190). The typical signal to noise ratio for the anode signal was 0.07 %.

The Frisch grid was fabricated using 76 μm diameter beryllium copper wires and oriented parallel to, and 9 mm above, the anode. The pitch between neighboring wires was chosen to be 1 mm and is discussed in detail in Sec. 2.3.2.2.

The electric field inside the drift region of the MUSIC detector is generated by the electrode surfaces of the PCBs and of the exit and entrance windows. The side wall PCBs have 0.2 mm wide conducting strips spaced 1mm apart and connected through a resistor chain to the cathode and anode providing a uniform electric field near the side walls that extends from the cathode to the Frisch grid and between the Frisch grid and the anode. In addition, the beam enters and exits the MUSIC field cage through 0.5 μm thick polypropylene windows with an active areas of 30 mm

21

$\times$ 30 mm. By evaporating 1.6 mm wide Al strips, spaced 2.54 mm apart, and biasing them to the same voltage as the side wall PCB we ensured a uniform electric field throughout the MUSIC field cage. The locations of the first and last rectangular anode sections were chosen so that all electrons that drift to these pads pass through a region where the drift field is uniform to better than 1%.

The drift field is defined by the negative high voltage on the cathode and the ground potential of the anode pads which are individually grounded through 100 MΩ resistors. The minimum voltage that can be applied to the cathode is -5 kV without exceeding the maximum voltage drop over the resistors in the field cage. A simplified voltage divider circuit and Frisch grid filter is shown in Fig. 2.5a. An iseg VHQ 203M power supply was used to bias the cathode. Table 2.1 contains the bias voltage, drift field, and electron drift velocity for gas configurations used in this paper which are discussed in detail in Sec. 2.3.2.4.

Table 2.1 Selected gas properties of CF$_4$ at running conditions.

Gas (torr)	Cathode voltage (V)	E_C (V/cm)	e^- drift velocity (cm/μs)	Avg energy per ion pair (eV)
CF$_4$ 150	-1000	192	10.3	34.3
CF$_4$ 200	-1335	256	10.3	34.3
CF$_4$ 294.5	-1000	192	8.3	34.3

This light-weight MUSIC assembly sits within a larger aluminum box that provides additional shielding and serves as a pressure vessel. To minimize gas contamination and recombination in the active region of the detector, gas flows directly from the gas handling system into the active region through numerous small holes in the anode PCB, seen in Fig. 2.5b. This enforces a laminar gas flow from the anode to the cathode and minimizes recombination. Then the gas flows through small holes in the cathode to the outer pressure holding vessel and finally back to the gas handling system. To further minimize loss of signal from recombination, the resistors in the field cage were all placed on the side of PCBs facing the outer gas region, and were covered with EZ-Poxy to reduce outgassing.

2.3.2.2 Frisch Grid Considerations

Beam particles entering the gas volume of the MUSIC detector make a straight line path ionizing the gas and creating a cylindrical distribution of electrons and positive ions along the path of the beam particle. Since the electron drift velocity greatly exceeds that of the ions, positive ions remain in the gas long after the electrons are collected on the anode. Absent a Frisch grid, this positive ion charge induces a negative image charge on the anode that reduces the net anode signal by an amount that depends on the distance of the track from the anode. With a Frisch grid in place, the image charges mainly appear on the Frisch grid instead, and the anode signal is basically independent of the vertical position of the track within the chamber.

Following Bunemann [28], we define the grid "inefficiency", γ, to be a measure of how independent the field strength at the anode, E_A, is to the field created by positive ions in the cathode region, E_Q:

$$\gamma = \frac{dE_A}{dE_Q}, \tag{2.3}$$

where γ is given by Bunemann's expression:

$$\gamma = \frac{d}{2\pi(x_A + r - \pi r^2/d)} \ln \frac{d}{2\pi r}. \tag{2.4}$$

Here, $x_A = 9$ mm is the distance between the Frisch grid and the anode PCB boards, $d = 1$ mm is the wire pitch, and $r = 38~\mu$m is the radius of the Frisch grid wires, shown in Fig 2.5a. This provides a value of $\gamma = 0.026$, effectively suppressing the dependence of the anode signals on the position of the positive ions in the detector.

If the anode were fully shielded, then no electrons would make it past the grid to the anode. The shielding of the anode to the positive space charge must be balanced against the need for most electrons to reach the anode. The proportion of electrons collected on the anode is roughly equal to the proportion of field lines that bypass the Fricsh grid, and terminate on the anode. Bunemann calculated the condition for the relative field strengths in the anode, E_A, and cathode, E_C, drift regions where all field lines by-pass the Frish grid [28]:

$$\frac{E_A}{E_C} \geq \frac{1 + 2\pi r/d}{1 - 2\pi r/d}. \tag{2.5}$$

For our chosen values of d and r, the field in the anode region must be 1.6 times larger than the field in the cathode region to satisfy this condition. We constructed a voltage divider for the field cage accordingly to achieve E_A/E_C = 1.8, satisfying the condition given by Eq. 2.5, and minimizing the loss of signal due to electrons terminating on the Frisch grid instead of the anode.

2.3.2.3 Position sensitivity of the MUSIC

The four triangular anode pads allow the horizontal "x"-position of the track to be determined at the entrance and exit of the MUSIC detector. Each track deposits charge on the pad surfaces that are directly above it. This makes the deposited charge in the triangular pad proportional to the width of the pad at the x-position where the charge is deposited. Defining beam right to be positive x direction and the left pad to be the one that is wider on the beam-left side of the anode plane, one can divide the difference in the charges in the right and left pads by the sum of both charges to get the x-position as follows:

$$x = x_{max} \frac{Q_R - Q_L}{Q_R + Q_L}, \tag{2.6}$$

where Q_L and Q_R is the charge deposited on the left and right triangular pads, respectively, and x_{max} = 41 mm is half the width of the anode plane.

The y-position of the track can also be determined from the time difference between the signal in MCP2 located 40 cm upstream, which records the arrival time of the beam particle and the anode signal which starts when the ionized electrons pass through the Frisch grid. If the drift velocity of electrons in the detection gas is known, then the delay time for the anode signal is a linear function of the drift distance from the track to the anode plane. By combining the x and y positions determined by these anode signals, the location and direction of beam tracks can be reconstructed in 3D space and extrapolated to different points along the beamline.

2.3.2.4 Gas selection and properties

CF_4 was selected as the detection gas. It has the virtues that it is not explosive, has a fast drift velocity, which minimizes pile-up effects, and a large stopping power. Table 2.1 provides relevant counter gas properties for CF_4, including the electron drift field strengths, drift velocities calculated using MagBoltz [29], and average energy required to produce an ion/electron pair [30].

2.3.3 HPGe

For calibration and characterization of the HEIST system, individual isotopes in the beam were uniquely identified by stopping them in an aluminum block after they pass through the MUSIC detector and detecting γ-rays fed by the decay of long-lived isomers in these isotopes. Isomers suitable for this detection method are those which have lifetimes comparable to the beam ToF as it travels down the beamline. For our experiment, this typical range is 100 ns - 100 μs, with a 100 μs timing window from the electronics. These γ-rays were detected in an OR120 Ortec High Purity Germanium crystal (HPGe), which is a liquid-nitrogen cooled GEM series HPGe coaxial detector system. The Ge crystal in this model of detector has dimensions 80.8 mm $\times$ 105.8 mm, with a 4 mm gap between the end cap of the housing and the crystal. A 1 mm thick Aluminum layer and 0.7 mm of inactive Germanium served as absorbing layers. Despite the attenuation of some γ-rays in the absorbing layers, we were able to match the observed coincident γ-rays to known isomers fed γ-rays and thereby uniquely identify many of the isotopes in the beam, as discussed in Sec. 2.5.1. At typical gamma-ray energies observed in this experiment (300 - 1000 keV), a resolution of 1.1 keV (FWHM) was achieved.

2.4 Commissioning HEIST with stable beams

A number of stable primary ^{208}Pb beams were used to commission HEIST, ensuring proper functionality and calibration of the various detector systems described above. The properties of these beams are detailed in Table 2.2.

Table 2.2 Selected properties of stable ^{208}Pb beams used to test detectors.

Beam type	$B\rho$ (Tm)	Charge states
Pilot beam	4.4785	63^+
Calibration beam	2.5782	79^+, 80^+, 81^+, 82^+

2.4.1 ToF Calibration

The absolute time of flight between the two MCP detectors was determined using a ^{208}Pb^{+63} primary beam from the CCF. The resulting ToF spectrum for this beam is shown in Fig. 2.6a. The beam's rigidity, and therefore velocity, is set by the A1900. Using LISE++, the physical ToF for the primary beam can be calculated for the flight path along the beamline. By fitting the ToF spectra, we corrected for unknown cable delays so that the absolute flight times were obtained for all beams.

To provide a further check, the primary beam was degraded prior to the A1900 and transmitted with the magnetic rigidity set to 2.5782 Tm. As the primary beam passes through the degrader, it will exchange electrons with the target producing multiple charge states which after the $B\rho$ selection of the A1900 will have different velocities. We observe the degraded primary beam in four charge states: Q/e=Z, Z-1, Z-2 and Z-3, where Z=82. The ToF values shown in Fig. 2.6b for these four charged states agree with the expected values to within 0.2 ns.

2.5 Rare Isotope Beam Measurements

2.5.1 Beam Identification

Fig. 2.7 shows the correlation between the secondary beam ToF (x-axis) and the sum of the energy losses measured by the nine rectangular anode electrodes in the MUSIC for the secondary beam tuned to $B\rho$ = 3.1173 Tm. Multiple peaks appear in this two dimensional spectrum. Each represents a different isotope, which is marked on the figure. Since this PID plot is unchanged by stopping the beam ions in an aluminum block approximately 30 cm downstream, we can identify these ions by measuring the γ-rays emitted after an isomeric state decay with the HPGe detector.

Fig. 2.8 illustrates the identification of secondary beam isotopes. Gates on each of the PID peaks and coincident γ-ray spectra were obtained for each peak. The black contour in Fig. 2.8a surrounds the ^{198}Pb PID peak with Q/e=80. The middle panel of Fig. 2.8b shows the ^{198}Pb γ-ray
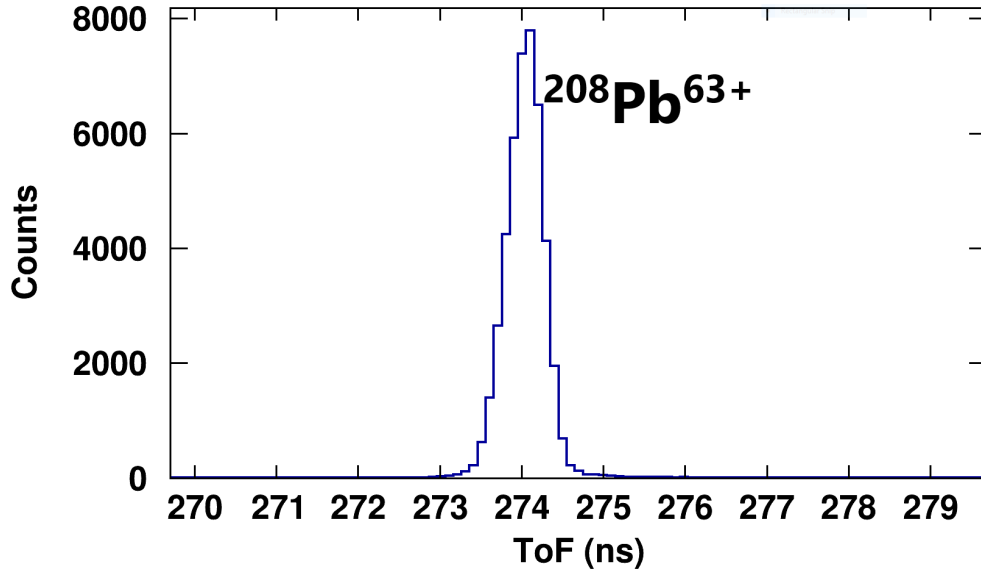
(a) Undegraded ^{208}Pb^{63+} beam.
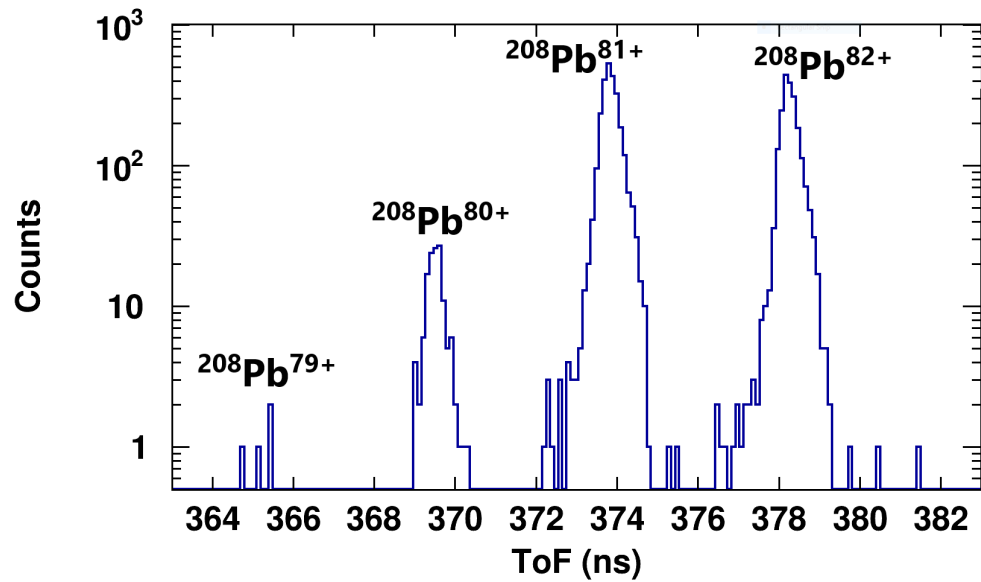
(b) Multiple charge states of ^{208}Pb.

Figure 2.6 ToF spectra for two primary beam settings. Shown in (a) is the ToF spectra for an undegraded primary ^{208}Pb^{63+} beam with Bρ = 4.4785 Tm. Shown in (b) is the ToF spectra for multiple charge states of the ^{208}Pb beam with Bρ = 2.5782 Tm.
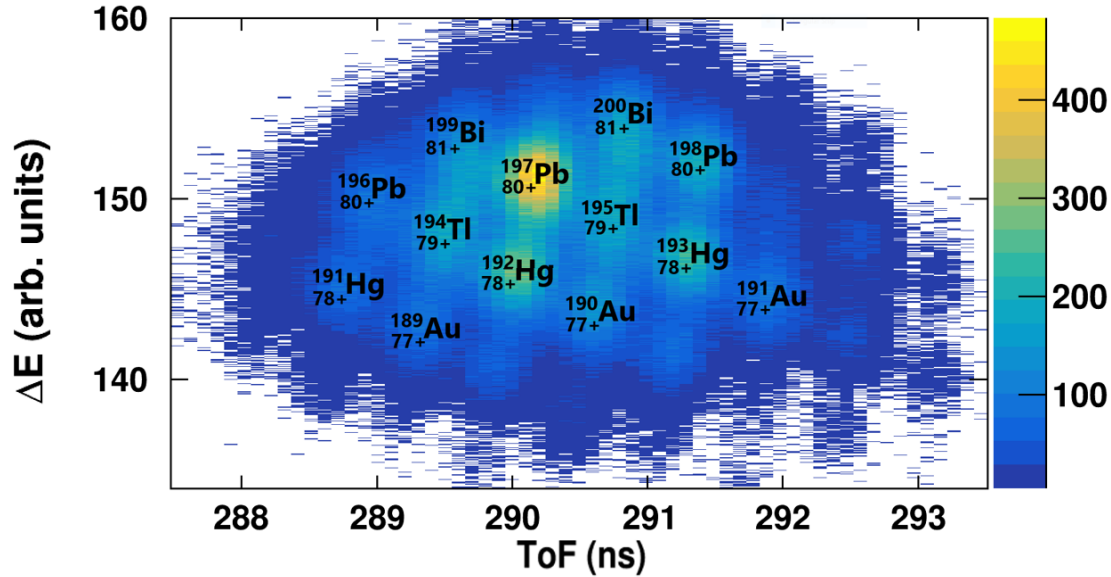
Figure 2.7 The PID plot of secondary beam isotopes.

peaks that were observed for ions detected within the black contour. For isomer decays to feed these γ-ray transitions, ^{198}Pb isomer states must have long enough lifetimes so that some isomers survive the 590 ns flight from the production target.

Fig. 2.8b also shows some other examples of gamma ray spectra that enabled us to identify other isotopes. Table 2.3 lists all the nuclei that were identified via isomer fed delayed γ-rays [31] and their associated energies. While our single HPGe detector does not provide details of the feeding of isomer decays into the delayed γ-ray we observe, there is enough consistent information obtained from all of these decays that there can be no doubt about isotope assignments shown in Fig. 2.7.

2.5.2 Beam Resolution

Fig. 2.7 visually displays the amount of separation between isotopes achieved with HEIST. To make more concrete comparisons to our estimated ToF performance, we first put a gate on the PID spectrum shown by the red dashed line in Fig. 2.9a and plot the enclosed data as a function of the ToF in Fig. 2.9b.

The time resolution for each peak is about 300 ps, which indicates that each of these secondary beams follows its own tightly defined trajectory so that the final time resolution is consistent with
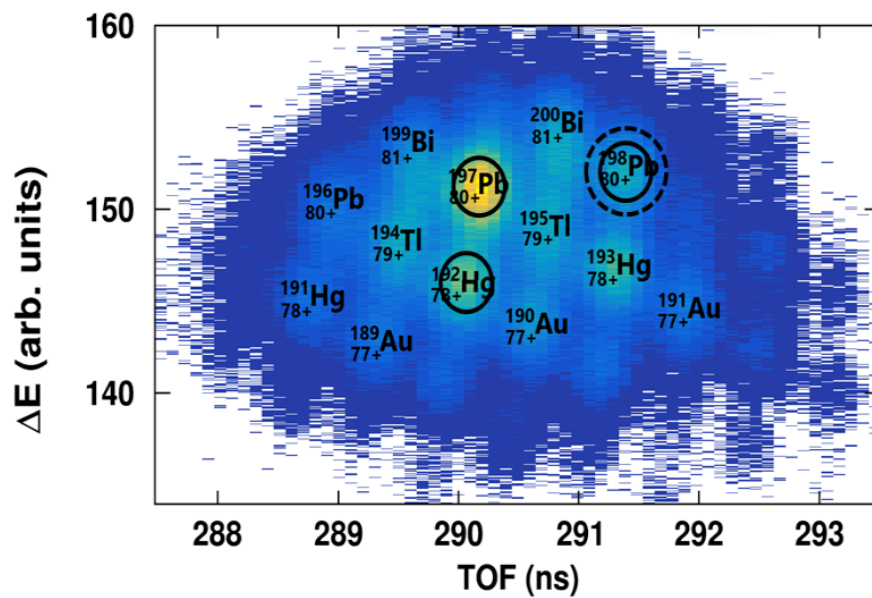
(a) PID with gate on ^{198}Pb^{80+}.
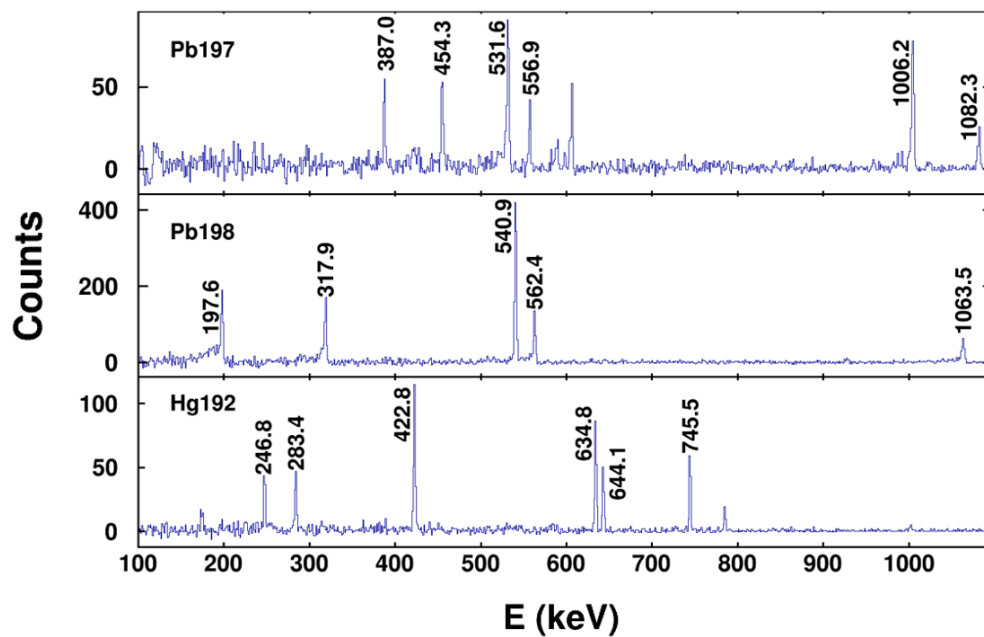
(b) Gamma spectra for various nuclei.

Figure 2.8 Shown in (a) is the secondary beam PID spectra. The dashed gate on ^{198}Pb is typical cut on an isotope. The solid gates drawn were used to produce the gamma spectra shown in (b): ^{197}Pb (top), ^{198}Pb(middle), and ^{192}Hg (bottom).

Table 2.3 A list of isotopes that have been confirmed by isomer tagging, their corresponding charge states measured in the PID, and some characteristic gamma rays seen in the HPGe.

Isomer-tagged Isotopes	Typical Gammas (keV)	Charge States Identified
^{196}Pb	337.3 , 371.9 , 689.0	79+ , 80+
^{197}Pb	387.0 , 531.6 , 589.0	80+
^{198}Pb	197.6 , 317.9 , 450.9	80+ , 81+
^{192}Hg	283.4 , 422.8 , 745.5	78+
^{194}Hg	280.2 , 427.9 , 636.3	78+
^{190}Au	232.3 , 854.9 , 427.8	77+
^{191}Au	264.0 , 420.1 , 725.2	77+ , 78+
^{199}Bi	145.7 , 499.6 , 1002.2	81+
^{201}Bi	185.8 , 411.7 , 967.4	81+

(a) PID with gate for ToF.
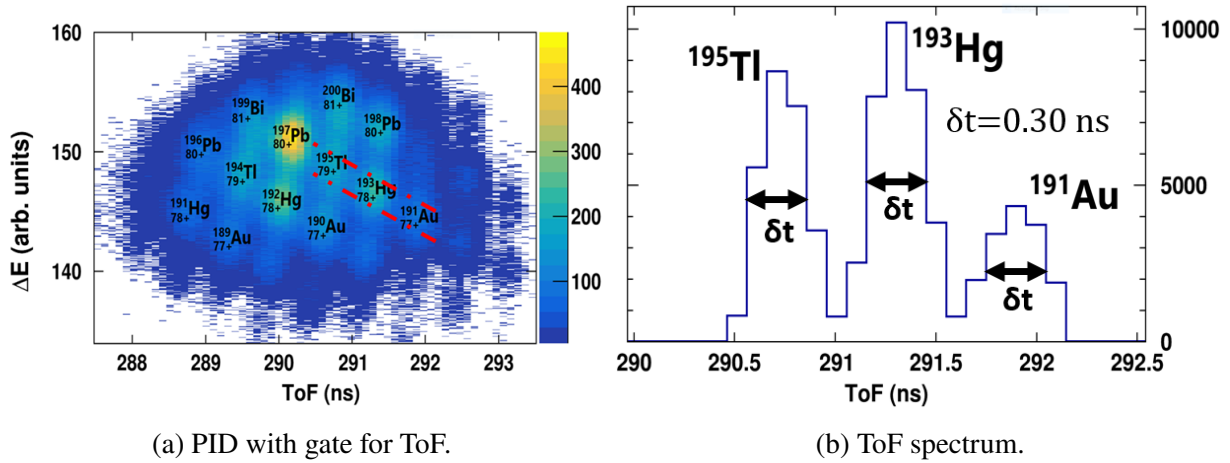
(b) ToF spectrum.

Figure 2.9 Shown in (a) is the secondary beam PID spectrum with a gate (in red) that provides information about the ToF resolution. Shown in (b) is the ToF spectrum for the gated data.

the simple estimate based on the noise and the rise times for the MCP signals made in Sec. 2.2.3.

To make similarly concrete comparisons to our estimated ΔE resolution, we apply the nearly vertical gate on the PID spectrum shown in Fig. 2.10a, and plot the enclosed data as a function of the energy loss ΔE in Fig. 2.10b. The observed ΔE resolution is approximately 2.2 % (FWHM) of the average ΔE deposited in the MUSIC chamber for that isotope. This is about 2.5 times larger than the estimated 0.85 % resolution given by the calculated straggling using SRIM. To explore this discrepancy, a GEANT4 [32, 33, 34] Monte-Carlo simulation was made using the physical detector geometry to explore secondary effects, like delta electron production. The simulation showed an energy resolution of 3 % (FWHM), consistent with, though somewhat larger than, the

(a) PID with gate for ΔE.   (b) ΔE spectrum.
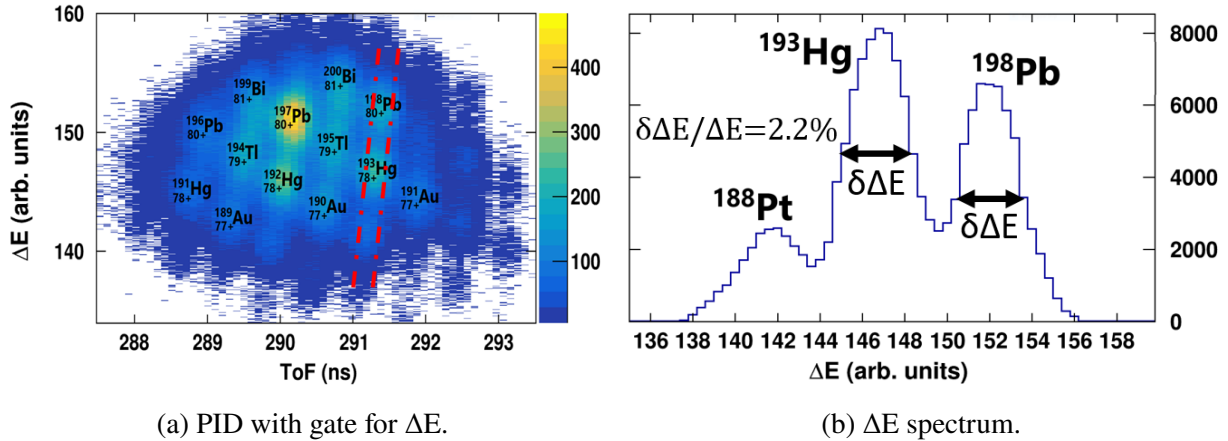
Figure 2.10 Shown in (a) is the secondary beam PID spectrum with a gate (in red) that provides information about the ΔE resolution. Shown in (b) is the ΔE spectrum for the gated data.

experimentally determined resolution.

It is impossible to quantify the performance of HEIST in a single number. Because the tails of the energy and time distributions of different species overlap, the purity of an isotopic selection depends on the cut made. The maximum purity of a cut is determined by the amount of charge state contamination from same Z isotopes. If there is no directly overlapping charge state in the acceptance of the beamline, a cut can be made that has an arbitrarily high purity, at the cost of lost statistics. The typical ^{198}Pb^{80+} cut shown by the dashed gate in Fig. 2.8a contains 89% of all ^{198}Pb^{80+} in the beam, and has a purity of 86%. A purity of $\geq$ 99% ^{198}Pb^{80+} was achieved using a cut containing less than 20% of the all ^{198}Pb^{80+} in the beam.

Table 2.4 Theoretical ToF calculated by LISE++ compared to the measured ToF after absolute time calibration of the MCPs.

Isotope	LISE++ ToF (*ns*)	Data ToF (ns)
^{198}Pb^{80+}	292.14	292.06
^{197}Pb^{80+}	290.88	290.86
^{196}Pb^{80+}	289.61	289.68
^{196}Pb^{79+}	292.75	292.64
^{193}Hg^{78+}	292.07	291.98
^{192}Hg^{78+}	290.77	290.74

2.5.3 Charge State Contamination

One of the challenges of data from a RIB containing high-Z isotopes is the issue of charge state contamination, or the presence of more than one charge state configuration for a given isotope in the beam. The acceptance of our beam line limits the number of charge states of a given isotope to one or two. Most isotopes arrive at the MUSIC in a helium-like configuration with Q/e = Z-2. However, that does not prevent contamination from another isotope with a less probable charge state from contributing to the PID spectrum within the same PID gate.

After identification of the isotopic species through isomer tagging in the HPGe, LISE++ was used to calculate ToF for several different charge states of each isotope. Table 2.4 shows a comparison of the calculated ToF from LISE++ and the corrected experimental data. The measured and calculated ToF agree to within 1 ns, whereas the ToF difference between adjacent charge states for a given isotope is on the order of several ns, allowing for the unique identification of the charge state.

Examples of both lithium-like and hydrogen-like secondary charge states have been detected and identified using the HPGe. Separation of neighboring charge states in ToF allows for the observed ratio of charge states to be measured accurately. Fig. 2.11 illustrates this process when the HPGe selection is set to select ^{196}Pb. The two resulting peaks in Fig. 2.11a indicate the presence of two separated charge state peaks, determined to be the helium-like (80+) and lithium-like (79+) configurations by ToF. The peak from the lithium-like charge state is not immediately obvious in the ungated PID, as seen in Fig. 2.11b. The observed ratio between charge states of the same isotope depends on the acceptance of the beamline and may differ from the actual production ratio at the A1900.

Fig. 2.12 shows measured charge state distributions for the two most common charge states of ^{196}Pb and ^{191}Au. The physical rigidity cut of the A1900 is shown by a vertical bar. Using the GLOBAL [35] model implemented in LISE++, the theoretical charge state distribution across a range of A1900 rigidity cuts was calculated, as seen in Fig. 2.12.

There is a discrepancy between the calculated charge state distributions and experimental
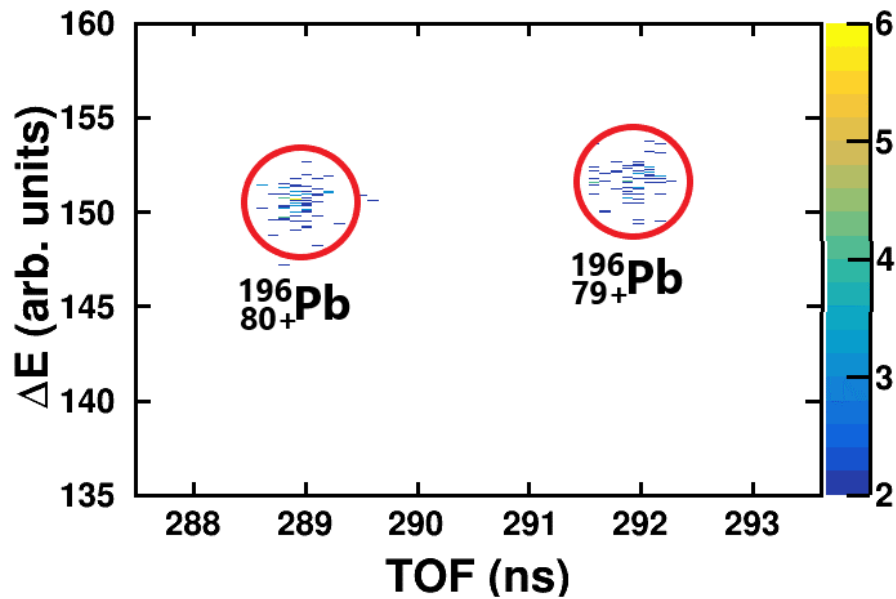
(a) PID with gate on ^{196}Pb γ-rays.
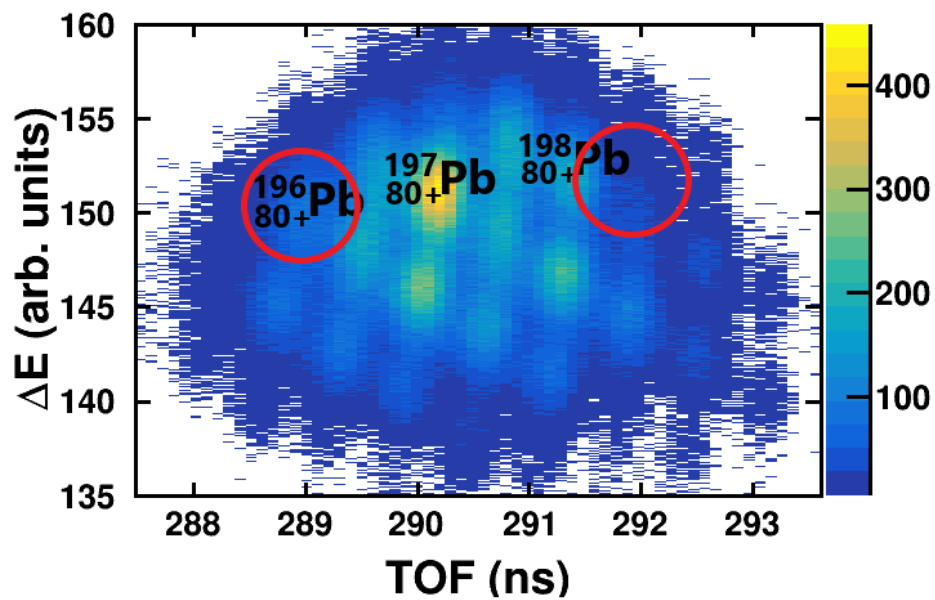
(b) Ungated PID.

Figure 2.11 An example of the presence of multiple charge states in the RIB for ^{196}Pb. The main 80+ charge state is clearly visible in the ungated PID, while the 79+ state is not obvious. (a) shows the the measured PID for events with a gamma ray fed by the decay of an isomer state in ^{196}Pb. (b) shows the full PID with the location of ^{196}Pb charge states circled in red.
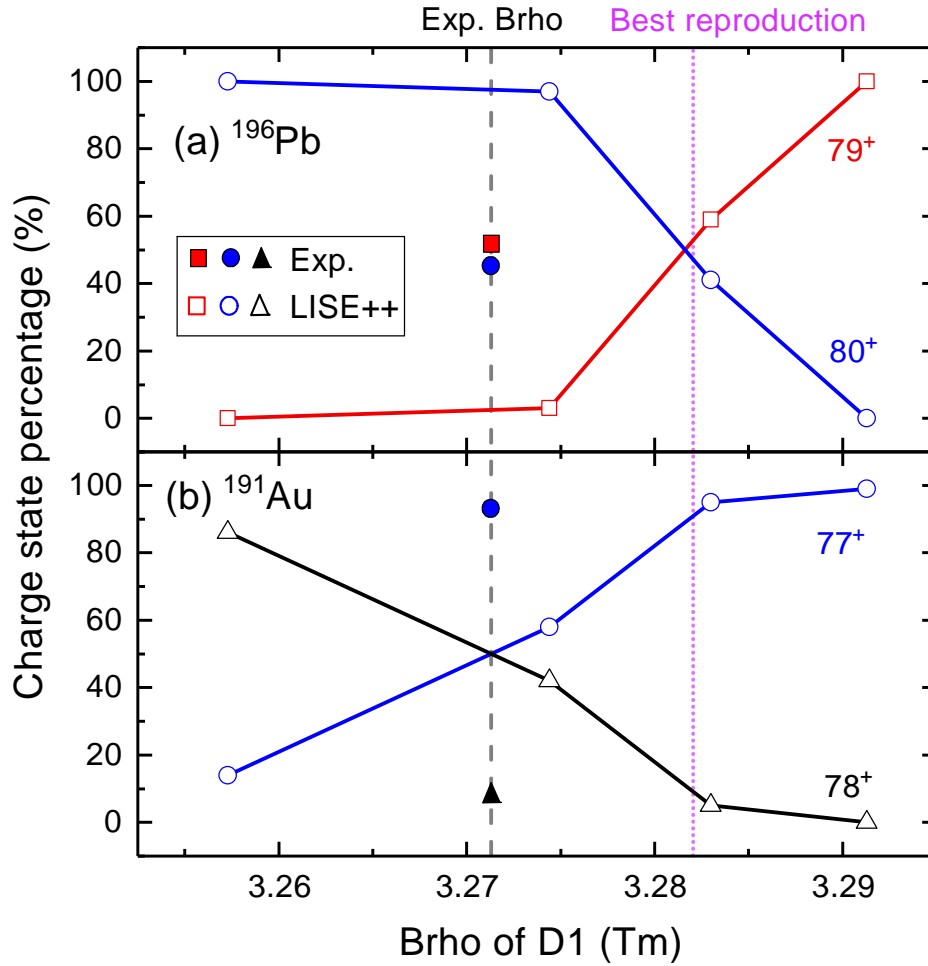
Figure 2.12 The measured charge state distributions of (a) ^{196}Pb, and (b) ^{191}Au are plotted as a function of rigidity in the A1900. The solid symbols indicate the experimental values, while the open symbols shows the LISE++ simulation results using the GLOBAL model.

measurement. The model reproduces the data quite well if the Bρ value of the A1900 and beamline is adjusted upwards in the calculation by 0.3% to 3.283 Tm from 3.271 Tm. A comparison between the calculated and measured charge state distributions at this adjusted Bρ value is shown in Table 2.5. This discrepancy is larger than the uncertainty in the calibration of the A1900 rigidity which is believed to be good to ±0.1%. This discrepancy can be explained by GLOBAL under-predicting the electron capture cross-sections for these nuclei. Regardless of the reason for the discrepancy, the predictions of GLOBAL at the adjusted Bρ value are consistent with all measurements made.

Table 2.5 A comparison between the theoretical and measured charge state distributions of isotopes Pb, Hg, and Au with the charge state $Q = Z - 3$, $Z - 2$, and $Z - 1$. The theoretical charge state distributions were calculated using the GLOBAL model with LISE++ at the adjusted Bρ of 3.283 Tm. The experimental charge state distributions were extracted by gating on the corresponding γ-rays from known isomers.

Isotopes	Calculation			Experiment		
	$Z - 3$	$Z - 2$	$Z - 1$	$Z - 3$	$Z - 2$	$Z - 1$
^{196}Pb	59%	41%		52% ± 3%	48% ± 3%	
^{197}Pb		100%			100%	
^{198}Pb		100%			99% ± 2%	1% ± 1%
^{191}Hg	27%	73%		-	-	-
^{192}Hg		100%			100%	
^{193}Hg		100%		-	-	-
^{189}Au	2%	98%		-	-	-
^{190}Au		100%			100%	
^{191}Au		95%	5%		95% ± 5%	5% ± 1%

2.5.4 Beam Tracking

The MUSIC detector has the capability to measure the position and direction of the beam as it passes through the detector. As discussed in Sec. 2.3.2.3, the x-position is determined by charged division with the triangular pads at the entrance and exit of the MUSIC detector and the y position is determined from the drift time of the electrons to the Frisch grid.

To check the x- and y- position resolution, the last quadrupole magnet along the beamline was turned off so the beam would clip the edges of the MUSIC entrance window. Fig. 2.13 shows the measured beam profile. The MUSIC entrance window's right and upper edges are clearly shown. The corresponding x- and y- position distribution is shown in the upper panels of Fig. 2.14. A numerical differentiation of the spectrum was performed and fit with a Gaussian in order to determine an upper limit to the position resolution, shown in the lower panels of Fig. 2.14. This differentiation method includes non-uniform beam effects. Using this differentiation method, the upper limit of the position resolution was determined to be 1.45 mm in the x-direction and 0.27 mm in the y-direction.

A more accurate measurement of the y position resolution can be made using the 9 independent measurements of the y position, one from each rectangular anode pad. This is done by comparing
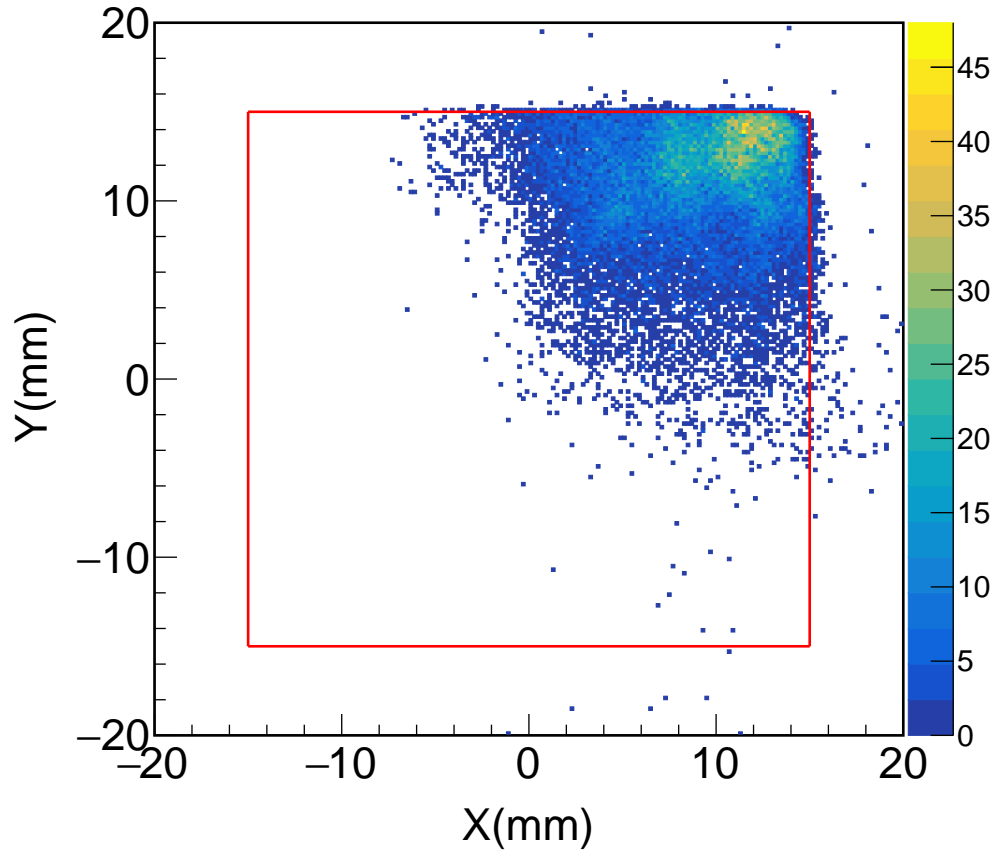
Figure 2.13 (Color online) Experimental beam hit pattern on the entrance of the MUSIC. The red square shows the edge of the MUSIC window.

the measured y position of a particle at a pad with the interpolated y position from the neighboring pads on an event by event basis. Fig. 2.15 shows the y position difference between the average of the $(n+1)^{th}$ & $(n-1)^{th}$ pads, and n^{th} pad. The FWHM of this difference distribution is 0.19 mm, so the y resolution for each pad is $0.19/\sqrt{3/2} = 0.16$ mm.

As seen in Figs. 2.16 and 2.14, within the MUSIC detector there is a structure to the x-position of the beam. Even though the momentum selection at I2 is very precise, the wedge foil modifies the energy of the beam and therefore its rigidity, and different beam particles ultimately enter the MUSIC at different x positions leading to the structure observed.

With accurate measurements of the positions at the entrance and exit window of the MUSIC, the beam particle trajectory can be extrapolated to other detectors along the beamline. Fig. 2.16 shows

36
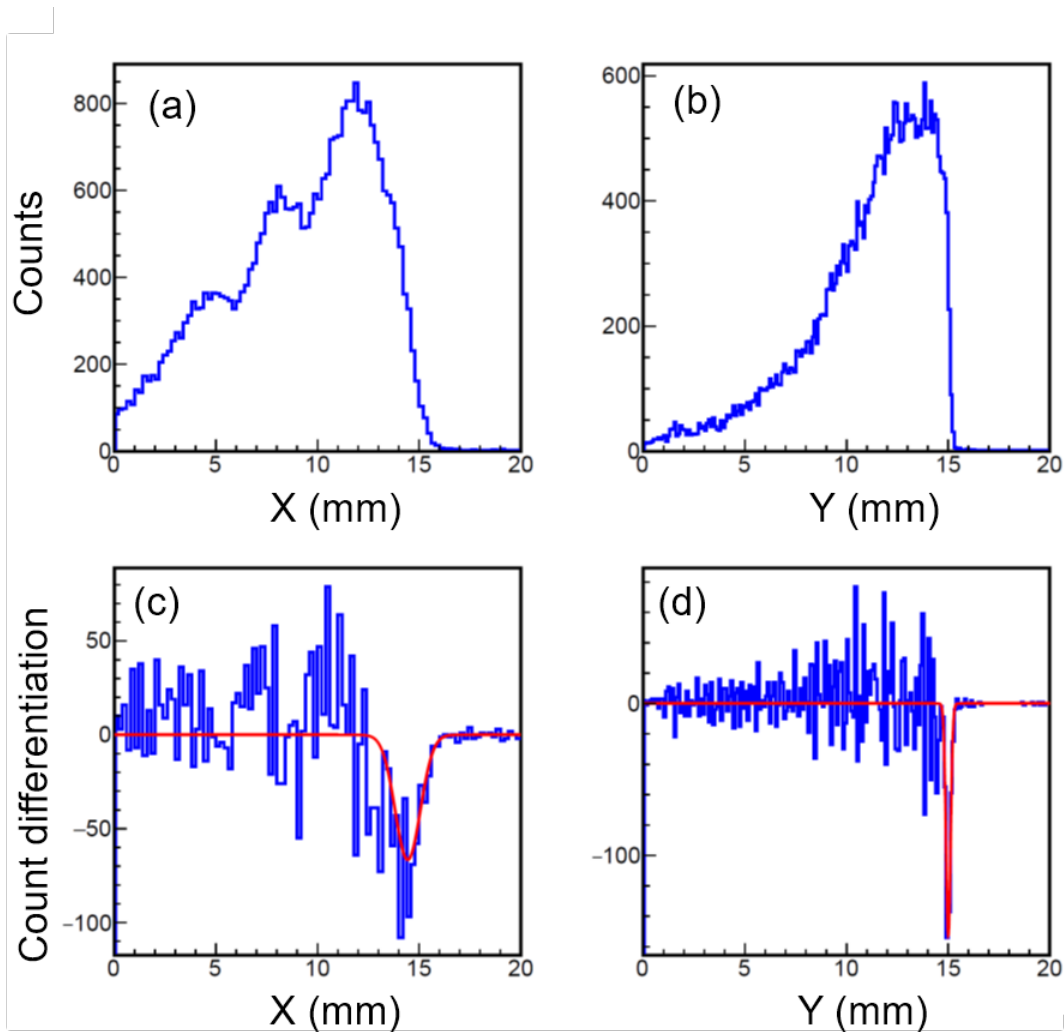
Figure 2.14 (Color online) The position distribution is shown in X direction in (a) and the Y direction in (b). The numerical differentiation of the position spectrum with the edges fitted with a Gaussian function are used to determine the position resolution. (c) shows the differentiated position for X, and (d) shows the differentiated position for Y.
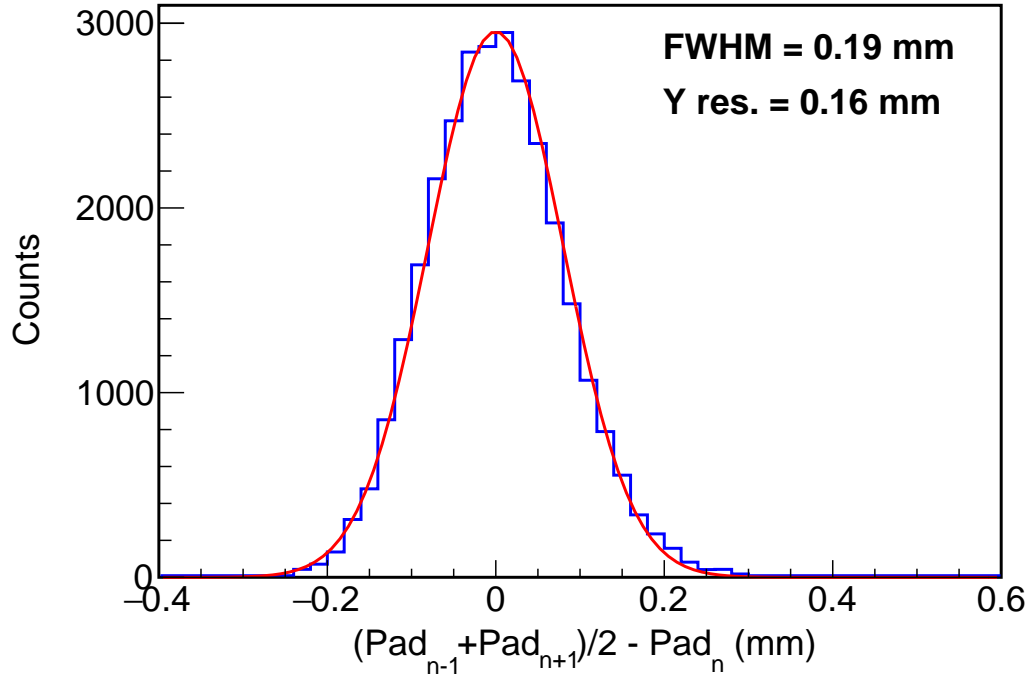
Figure 2.15 The Y position difference between the average of $n + 1$ & $n − 1$ and n rectangle pads.

the beam tracking results with hit patterns at different positions. At MCP2, before the MUSIC, the beam was well focused. In the MUSIC the beam was off-center, indicating a slight misalignment of the apparatus. The beam nonetheless enters the acceptance of the ATTPC entrance window 1.2 m downstream of the MUSIC detector.
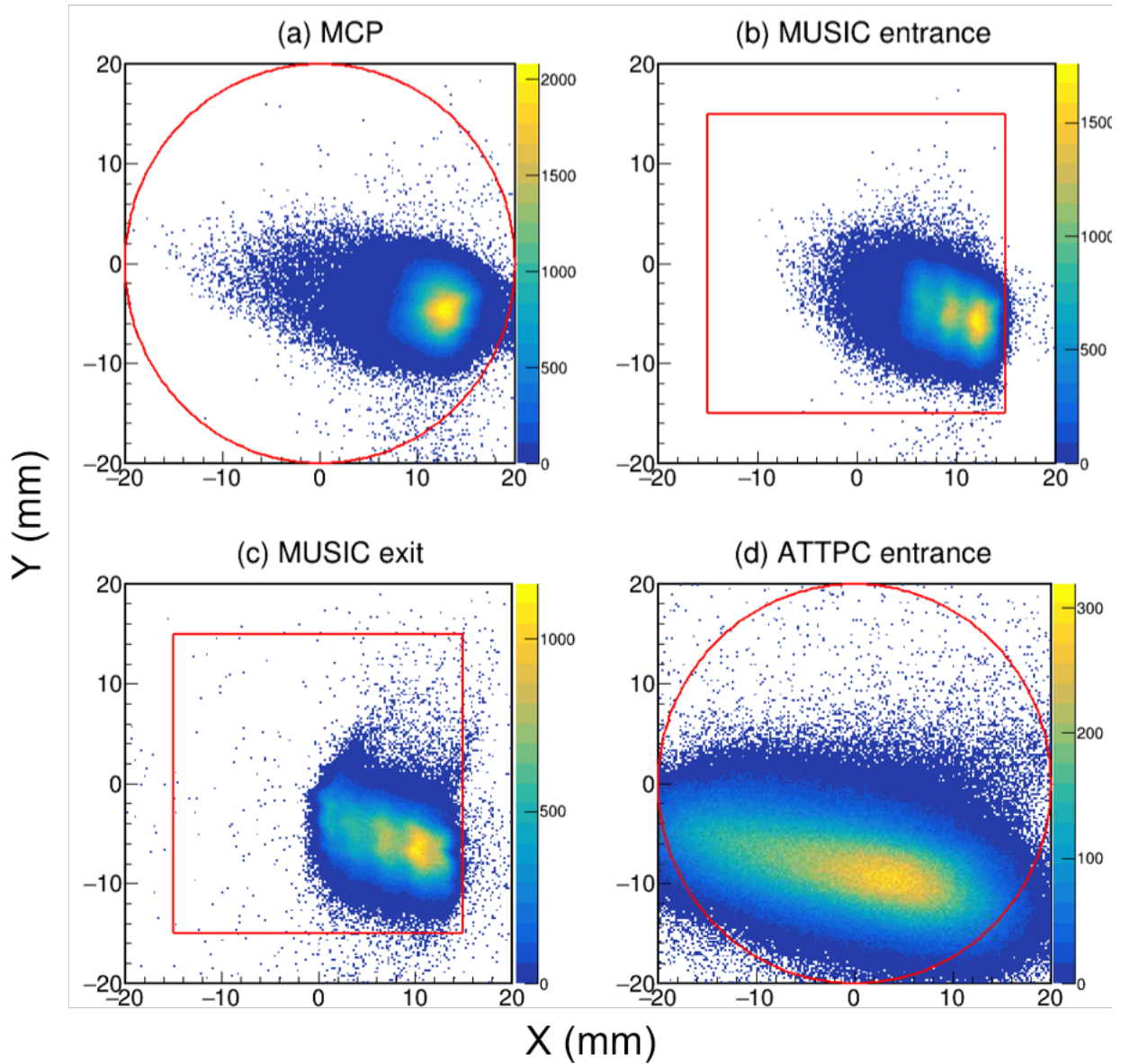
Figure 2.16 (Color online) (a) shows the extrapolated position spectrum at MCP2. (b) shows the position spectrum at the entrance of the MUSIC. (c) shows the position spectrum at the exit of the MUSIC. (d) shows the extrapolated position spectrum at the entrance to the AT-TPC. The red lines show the edge of detector windows.

CHAPTER 3

ANALYSIS TECHNIQUES FOR ACTIVE-TARGET TIME PROJECTION CHAMBERS

3.1   Operating principles of Active-Target Time Projection Chambers

Active-Target (AT) Time Projection Chambers (TPCs) are a class of particle detector used in physics experiments to study the reactions of charged particles. As the name implies, AT TPCs have two main defining features. It is both a target and a Time Projection Chamber (TPC). To start we will discuss the operating principles of a TPC. A TPC is a gas filled detector with a constant electric field applied. As a charged particle travels though the detector it will loose energy interacting with the gas, ionizing gas molecules producing a electron and ion pairs. The electric field will then drift the electrons towards the anode (or pad plane), and the ions towards the cathode. As the electrons near the anode, there is often a region with a very high electric field just above the pad plane that amplifies the number of electrons through of an avalanche process. In many modern detectors, the is achieved with a Micromegas [36], a thick Gas Electron Multiplier (GEM) [37], or a combination of the two.

After amplification, the electrons are collected on the anode. Typically the anode is highly segmented into many pads. Let us assume that these pads are arranged like tiles on an plane, the x-y plane. Typically the electric field, which points in the opposite direction of the electron drift velocity will be perpendicular to the x-y plane, so that electrons will drift from the point of ionization to the pad plane. Relative to the geometry of the pad plane, the direction of the beam is a choice made by the designer of the TPC. In the case of the MSU AT-TPC the direction of the beam is along the positive z-axis. That is, the z-axis points into the pad plane regardless of the beam direction. By recording on which specific pad the electrons are collected, we can determine the x and y position where the initial ionization occurred in the detector. By measuring the time the electrons take to drift to the pad plane we can project back the z position where the ionization originated if we know the drift velocity of electrons in the gas. The magnitude of the signal, or number of electrons collected, also gives us information on the amount of energy that was deposited in the detector. These pieces of information combine to allow us to track the trajectory of charged

particles through the detector, taking a "picture" of the particles involved in the reaction, which we call an event. This event can then be analyzed to extract information about the physics of the reaction being studied. The rest of this chapter is focused on an analysis framework to simulate and analyze these events.

The second defining feature of these detectors is they are Active Target detectors. That is, the detection medium doubles as the target. This has a few advantages over traditional detector setups which often use some thin foil as a target. In an AT detector the geometric efficiency is very high, resulting from the large angular coverage of the detection gas in the detector that often approaches 4π sr. Secondly, by making the target into a detector, we can correct for the energy loss in the detector event by event, thus correcting the reaction kinematics more accurately and preserving resolution. Because the beam (or the particle that induces the reaction by interacting with a nucleus in the gas) looses energy as it passes through the detector the energy of the beam at the point of interaction has a position dependence. Thus with a single beam energy we often measure the reaction of interest over a wide range of energies without re-tuning the beam which can be a time consuming endeavour. If that is the goal of the experiment, this dependence of energy on position is advantageous. Precision measurements of the energy dependence of these reactions are greatly facilitated by the position information in the TPC, which provides an accurate determination of where in the detector the reaction took place, called the reaction vertex.

Such measurements can often be improved by the introduction of a constant magnetic field parallel to the electric field. It serves a few purposes. First, it exerts a force on the charged particles passing through the detector, giving the tracks a helical shape. This spreads the charge deposited over many pads on the anode, and can increase our charge and position resolution while allowing a measurement of the momentum of the charged particle. It also extends the length of the track in the detector. All of these effects can help with particle ID, and identification of the energy of the particle [20]. Second, it decreases the effects of transverse diffusion of the drifting electrons [38]. Inclusion of a magnetic field, however, does complicate the experimental setup and may not be worthwhile for simple reactions like the fission process that we explore in Sec 4.

3.2 Analysis and simulation framework: ATTPCROOT

ATTPCROOT is a general purpose framework for the simulation and analysis of active target detectors using the electronics developed by the Generic Electronics for TPCs (GET) collaboration [39]. It is based on the FairRoot [40, 41] framework developed by the FAIR group at GSI, which itself is based on ROOT [42, 43] from CERN. Figure 3.1 shows a schematic representation of the flow of data from simulation/experiment to the determination of physics observables of interest.
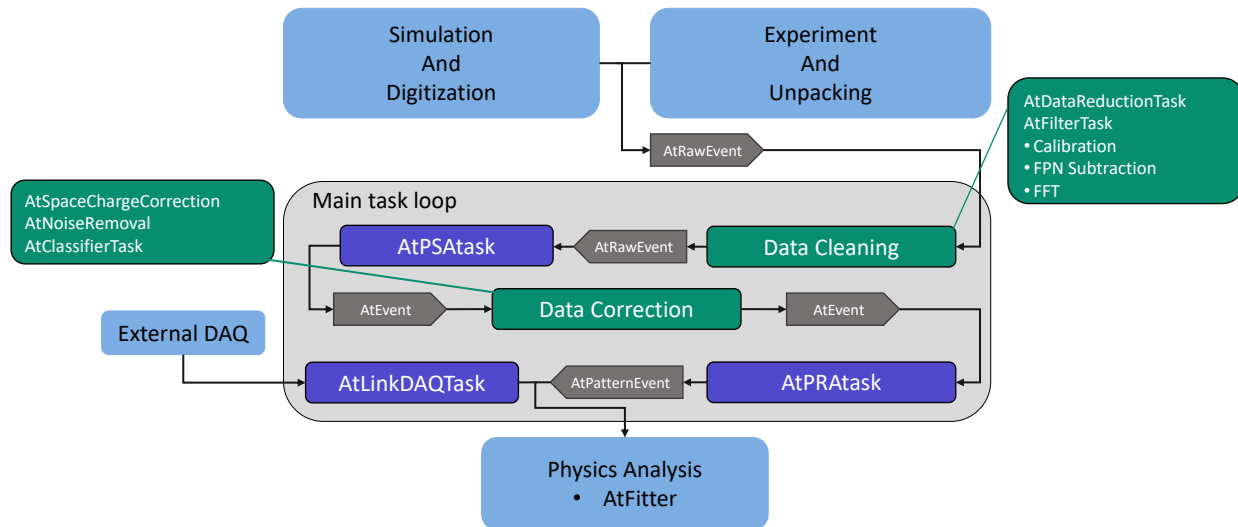
Figure 3.1 Schematic overview of the flow of data through the analysis framework. Grey boxes indicate data structures (or representations) used to pass information between task. Green boxes indicate analysis tasks that operate on a particular representation of the data. Purple boxes represent tasks that transform data into a new representation.

One of the fundamental assumptions of the ATTPCROOT framework is its agnostic nature to the source of the data being analyzed. This means that simulated and experimental data are treated the same during the analysis, shown schematically in Figure 3.1 where both simulation and experiment feed into the analysis framework at the same point. This feature allows us to use simulated data to calculate detector efficiencies by injecting these simulated tracks into the experimental analysis pipeline. The framework can accept GET data in a number of formats, and convert it into the generalized internal data structure. Likewise, simulations of experimental measurements are possible with many different detector systems using the GET hardware, and after the simulation of the detector response the data ends up in the same generalized data structure

as experimental data. From this shared point, the analysis of either simulated or measured data continues in an identical manner for all input sources. The details on the simulation of both physics and detector response is detailed in Section 3.3.

The framework is task based, like FairRoot, and data flows through the task list on an event by event basis with each task being executed sequentially. The framework employs a set of data structures common to all detectors and experiments for this transfer of data. An event at any of these transitional points between tasks can be written to disk for later analysis, or just kept in memory. The data structures used to pass an event between tasks, shown as gray arrow boxes in Figure 3.1, split the analysis into three distinct stages each using a particular representation of the data. Analysis tasks that act on a single representation of the data are shown as green boxes in Figure 3.1, and tasks that transform the data from one representation to another are shown as purple boxes in Fig. 3.1.

The three representations of the data that drive the structure of the framework are: Raw events, which are the waveforms that are directly digitized by the GET electronics or are the output of the simulation. These are then converted into a 3D (x,y,z) "hit cloud" in the detector which constitutes the second representation. These hits in the hit cloud then get grouped into track candidates which describe the ionization along the path of particles passing though the detector, which constitutes the third representation. In Figure 3.1, these three representations are indicated by the data structures AtRawEvent, AtEvent, and AtPatternEvent, respectively.

There are two "linking" tasks used to convert the data from one representation to another. The first is the Pulse Shape Analysis (PSA) task responsible for taking a waveform and transforming it into a single, or series, of points in 3D space each with an associated amplitude proportional to the charge deposited at that point. The second task is Pattern Recognition Analysis (PRA) which is responsible for identifying track candidates in the hit cloud. There are a number of implemented algorithms for these two task, which are detailed in Section 3.4.2 and 3.5, respectively.

Common across the framework are a number of parameters that are used in the simulation and analysis that are experiment or detector specific. Table 3.1 lists those parameters and their units.

These parameters will be referred to by name throughout this section.

3.3 Simulation

There are two distinct steps involved in simulating a physics event with the ATTPCROOT framework. First, is the simulation of the nuclear reaction of interest, and the subsequent interactions of the particles produced in the reaction with the gas in the active detector volume, see Sec. 3.3.1. Second, is the simulation of the detector response given the energy deposition in the active volume of the detector from the first half of the simulation, see Sec. 3.3.2.

3.3.1 Simulating particle transport

In this stage of the simulation, our goal is to calculate the amount of energy deposited by the charged particles moving through the detector, and where that energy is deposited. For each point in space, an instance of `AtMCPoint` is created to track this information along with additional information on the particle at that point in space. There are two methods of simulating events. One is to use Geant [44, 32, 33, 34] wrapped in ROOT's Virtual Monte-Carlo (VMC) [45] package (see Sec. 3.3.1.1). The other is a simple particle transport model that uses user-provided tabulated values of energy loss models to simulate the deposited energy in the detector (see Sec. 3.3.1.2). Shared between the two methods is the detector geometry. Typically, this geometry is defined using the ROOT geometry package and pre-generated for use in the simulation. It is here where the active

Parameter Name	Description	Units
E_{ext}	Applied electric field	V/cm
B_{ext}	Applied magnetic field	Tesla
TB_{win}	Detector entrance in time	Time buckets
z_{max}	Distance from entrance to pad plane	mm
w	w-value of detection gas	eV
F_{gas}	Fano factor of detection gas	-
D_L	Longitudinal diffusion coefficient	cm^2/us
D_T	Transverse diffusion coefficient	cm^2/us
v	Electron drift velocity	cm/us
$\overline{G}_{\mu m}$	Average micromegas gain	-
t_{clock}	GET clock period	us
C_{GET}	GET gain	F
τ	GET peaking time	us

Table 3.1 Parameters used in ATTPCROOT analysis package.

volume is defined, as well as the detection medium.

3.3.1.1 Virtual Monte Carlo Simulation

The VMC package, formerly a part of ROOT, allows for a Monte-Carlo simulation of the transport of particles through the detector. It acts a wrapper for various Monte-Carlo engines, including Geant4 and Geant3, and allows the user to change the Monte-Carlo engine with minimal change to the source code.

In a VMC calculation ancillary detectors can be added for detection of other particles such as gamma rays, in addition to the main active target detector. For example, in simulations with GADGET II, the simulation of gamma detection by SeGA is added in addition to the simulation of the Proton Detector (a TPC). Along with the detector geometry, a reaction generator needs to be defined for the interaction of interest. The generator is responsible for creating the reaction products (defining their initial positions and momenta) that will then be transported through the detector using the VMC package. Many experiments create a custom generator to describe the specifics of the reaction they are studying.

In the framework, the simulation of each event is split into two halves. The first half is the transport of the beam to the reaction vertex. The second half is the transport of the reaction products from the reaction vertex out to when they leave the detector volume, or stop in the gas. The class `AtVertexPropogator` is used to communicate information on the beam momentum at the reaction vertex to the reaction generator.

The end result of the VMC calculation is a collection of points in 3D space, with an associated energy loss at each point. These are the `AtMCPoints` discussed above. One point is created per particle being actively transported at each distance step in the underlying VMC engine. This collection of points is then passed to the second stage where the response of the detector is simulated.

3.3.1.2 Simple Particle Transport

In some cases, the full machinery of the VMC calculation is unnecessary and we can use simpler particle transport models. This is required in the current framework for the Monte-Carlo track reconstruction discussed in Sec. 3.7.2, and can be particularly helpful in experiments where

45

there is a large uncertainty in the physics models and one may want to easily swap between different physics models.

Just like the VMC method, the end result is a collection of `AtMCPoint`s. These points are generated using tabulated values of the particle's stopping power rather than the VMC engine. When a particle is added to the event, the framework will transport the particle until it exists the active volume, or stops. At each distance step, the energy loss of the particle is calculated using a cubic spline interpolation of the tabulated values for the stopping power. The framework allows importing energy loss tables directly from LISE++ [46] or SRIM [24], although it can be easily extended to any other energy loss model. Unlike the VMC method, the user is responsible for selecting on a per-particle bases the energy loss model to use and loading it into the framework.

3.3.2 Simulating Detector Response

After generating all of the `AtMCPoints` associated with an event, our task is to now take that information and translate it into waveforms, the same information we digitize when taking real data in an experiment. In the following section, we discuss how these waveforms can be simulated, starting from the distribution of ionized electrons.

3.3.2.1 Production of ion pairs and electron drift

The average number of electrons, N_e produced for amount of energy, E_{dep}, deposited in a gas is given by:

$$N_e = \frac{E_{dep}}{w} \tag{3.1}$$

where w is the average amount of energy it requires to produce an electron ion pair. The variance is given by the expression

$$Var(N_e) = FN_e \tag{3.2}$$

where we introduce a Fano factor F. If the process was purely statistical, and followed a Poison distribution, F would be equal to one. However, because the production of electron-ion pairs is due to interactions with electron shells in the gas, which are quantized and only a finite number are involved in the interaction, the true variance observed is less [47]. For typical detection gasses the

Fano factor is usually on the order of 0.05-0.2 [47].

For a given gas composition, w and F are near constant over a large range of particle types and particle energies. For each `AtMCPoint`, with energy deposition E_{dep} the number of electrons produced at that point will follow the Gaussian distribution with mean N_e (Eqn. 3.1) and variance FN_e (Eqn. 3.2). In this section, we will denote Gaussian distributions with mean μ and standard deviation σ as $G(\mu, \sigma)$. The number of electrons produced is then determined by randomly sampling the Gaussian $G(\frac{E_{dep}}{w}, \sqrt{F\frac{E_{dep}}{w}})$. We assume this entire collection of electrons is produced at a single point in space. This assumption works well as long as the expected amount of diffusion in the gas is large compared to the initial spread of the electrons at the ionization site.

The cloud of electrons produced is then drifted to the pad plane, applying the effects of diffusion in the gas. The average time, t_{avg} (μs), it takes for the electron cloud to drift to the pad plane is given by

$$t_{avg} = \frac{z_0}{v} \tag{3.3}$$

where v (cm/us) is the drift velocity of electrons in the gas and z_0 (cm) is the displacement from the interaction point where the gas is ionized to the pad plane. In the experiment that is the focus of this thesis the drift velocity of electrons in the He gas is 0.82 cm/us.

The actual arrival time of electrons produced at the interaction point (x_0, y_0, z_0) will follow distribution determined by the diffusion of the electrons in the gas. The arrival time of the electrons will follow the Gaussian distribution:

$$G(t_{avg}, \frac{\sqrt{2D_L t_{avg}}}{v}) \tag{3.4}$$

where D_L is the longitudinal diffusion coefficient in the typical units cm^2/μs.

Likewise, the electron cloud will also diffuse in the transverse direction. The position on the pad plane will be centered at the same x/y position as the interaction point, (x_0, y_0). The density distribution is given by the two dimensional Gaussian:

$$f(x, y) = \frac{1}{4\pi D_T t_{avg}} \exp -\frac{(x - x_0)^2 + (y - y_0)^2}{4D_T t_{avg}} \tag{3.5}$$

where D_T (cm^2/μs) is the transverse diffusion coefficient in the typical units cm^2/us [38].

At the pad plane, each electron needs to be assigned an arrival time and assigned to a pad. It is cumbersome and computationally inefficient to individually track each electron produced. Instead we assign electrons to pads by integrated their expected distributions at the pad plane. We start by assigning electrons to pads by integrating the transverse distribution (Eqn. 3.5) centered at (x_0, y_0) over each pad whose center point is within 3 standard deviations (from Eqn. 3.5) of (x_0, y_0). Because each detector has its own pad plane with arbitrary pad shapes we perform this integration through a Monte-Carlo process. The arrival time of the electrons at the pad plane is discretized by integrating Eqn. 3.4 over each time bin within 3 standard deviations (from Eqn. 3.4) of the average arrival time. The width of the time bins is chosen to be equal to the clock time of the electronics.

After this is performed for each `AtMCPoint`, we obtain the charge collected on each pad in the pad plane as a function of time. An example of the resulting charge distribution is shown in Fig. 3.4. The final step in simulating the detector response is simulating the response of the electronics to the collected charge.

3.3.2.2 Simulating the electronic response

Now that we have the collected charge on each pad as a function of time, the final step in the simulation is transforming that charge into a trace, or waveform. This is done by convolving the charge as a function of time with the response of the GET electronics:

$$s(t) = (i * r)(t) \equiv \int_{-\infty}^{\infty} i(\tau)r(t - \tau)d\tau \tag{3.6}$$

where $s(t)$ is the trace, $i(t)$ is the current on the pad, and $r(t)$ is the response function of the electronics to a delta function of charge at $t = 0$.

The nominal response function to charge collected at $t = 0$ is given by:

$$r(t) = A \exp\left(-3\frac{t}{\tau}\right)\left(\frac{t}{\tau}\right)^3 \sin\frac{t}{\tau}\Theta(t) \tag{3.7}$$

where A is related to the gain, τ is the peaking time of the electronics, and $\Theta(t)$ is the Heaviside step function [48]. This serves as a decent approximation of the response function, as seen in Fig. 3.2 and is sufficient for most simulations, including the simulation presented in the following. However, if high accuracy is needed one may need to determine the response function channel by

48

channel. The actual response function is channel dependent and Eqn. 3.7 underestimates both the fall time of the signal (seen in Fig. 3.2) as well as how long the response function takes to return to baseline after the pulse (seen in Fig. 3.3). We have found the response function is consistent within a single AsAd, exemplified by the small error bars in Fig. 3.2, which can simplify the response function analysis.
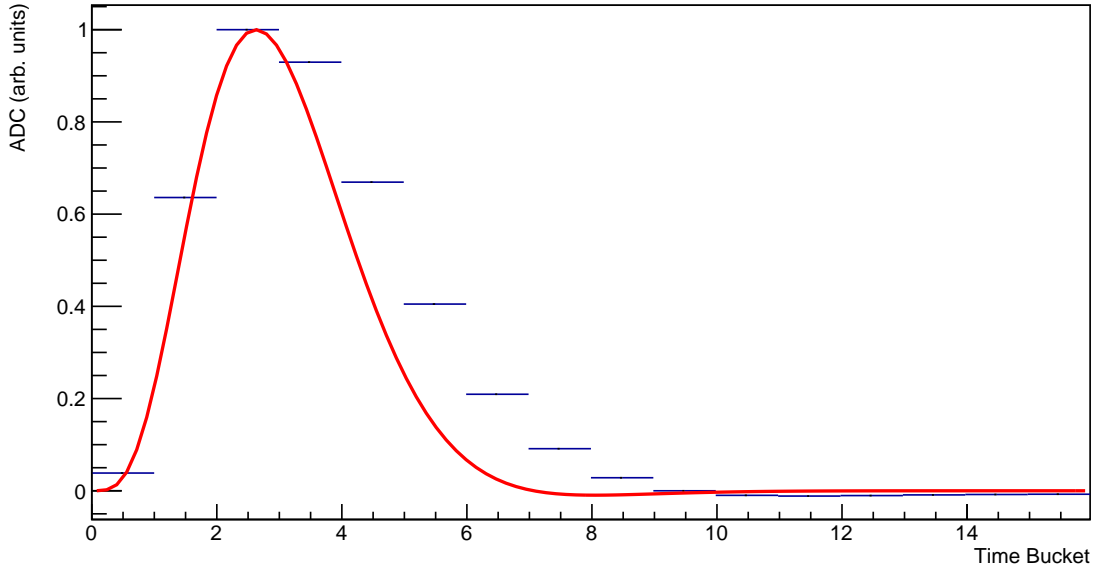
Figure 3.2 Figure showing the nominal response function (Eqn. 3.7 in red and the average response function for a single AsAd in blue. The 1 sigma error bars are hidden by the marker. The rise is well described by the nominal; however, the measured response function has a larger fall time.

The convolution required to acquire traces is done numerically for each channel using the binning intrinsic to the electronics, the clock time. For each pad the trace, s_i, is given by

$$s_i = Q_i \sum_{j=i}^{512} r(t_{clock} * (j - i)) \tag{3.8}$$

where i indexes the time buckets in the trace, Q_i is the current integrated over time bucket i, and t_{clock} is the clock time of the electronics (i.e. the length of time that corresponds to a single time bucket).

After the raw trace is calculated, two corrections are applied. First, we apply the electron amplification by the micromegas and ThickGEM. These are two distinct gain stages however we
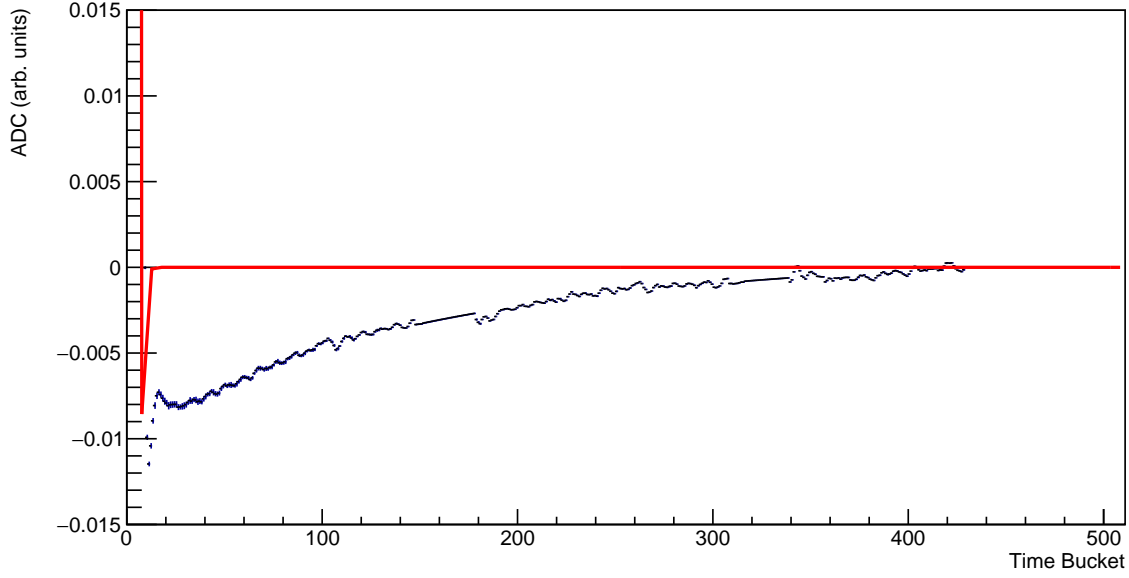
Figure 3.3 Figure showing the nominal response function (Eqn. 3.7) in red and the average response function for a single AsAd in blue with 1 sigma error bars. The measured response function has a larger undershoot and takes significantly longer to return to the baseline than the nominal response function. In this figure the vertical scale has been increased by a factor of about 70 compared to Fir. 3.3 to see small variations in the signal.

treat them as a single amplification stage for the sake of simplicity. The amplification factor for a single electron in one of these amplification stages can be approximated by the Polya distribution [49]:

$$P(N_e) = \frac{(1+\theta)^{1+\theta}}{\Gamma(1+\theta)} \left(\frac{N_e}{\overline{G}_{\mu m}} \right)^{\theta} \exp \frac{-(1+\theta)N_e}{\overline{G}_{\mu m}} \tag{3.9}$$

where θ is the Polya parameter (typically taken to be 1), and $\overline{G}_{\mu m}$ is the average gain. In the case where more than 10 individual electrons are being amplified in a single time bucket (which is almost always) we can simplify the gas gain calculation through the Central Limit Theorem. In that case (and assuming $\theta = 1$), the average gain for each electron is given by a Gaussian distribution with mean $\overline{G}_{\mu m}$ and variance $\frac{\overline{G}_{\mu m}}{2n}$ where n is the number of electrons being amplified in a time bucket. $\overline{G}_{\mu m}$ is selected empirically by tuning the value until the magnitude of simulated traces matches the experimental traces.

The second correction applied is to scale the trace for the gain of the electronics (the A in Eqn. 3.7). There are two different factors hiding in this one parameter. The first is the intrinsic electronic

50

gain, or what voltage is output by the electronics for N_e electrons at the input. This is parameterized by a capacitance C_{GET} in Farads and is equal to

$$V_{GET} = \frac{N_e e}{C_{GET}} \tag{3.10}$$

where N_e is the number of electrons collected and e is the charge of an electron. The second factor is the conversion factor from voltage to ADC units assuming a 12-bit ADC.

Finally, one can optionally add a high frequency noise component to the trace. This is done by sampling a Gaussian centered at 0 with a user-specified variance for each time-bucket and adding that to the final value of the trace (the units of the variance are squared ADC units). This can be useful in evaluating some PSA methods like the one discussed in Sec. 3.4.2.1.

The end result of the simulation is an `AtRawEvent` containing the simulated traces for each pad. From this point on, the simulation and experimental analysis pipelines join and the simulated data can be treated in the same way as the experimental data. Fig. 3.4 shows the charge collected on a single pad and the resulting simulated trace for that pad.
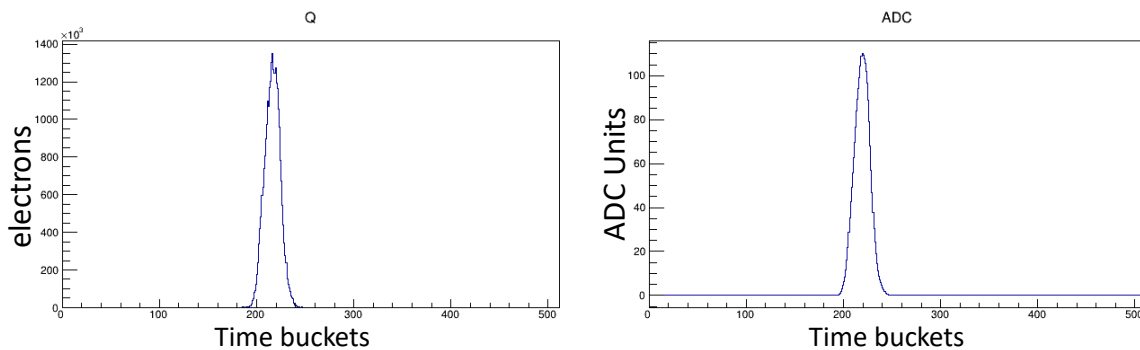
Figure 3.4 Figure showing the number of electrons collected on a pad in the simulation, and the resulting simulated trace assuming the nominal response function.

3.4 Charge and position reconstruction

Our starting point for any analysis is the collection of traces in an event stored in the data structure `AtRawEvent`. This collection can either be from simulation or experimental data.

3.4.1 Corrections to traces

At this stage, there are often a series of corrections applied to the data, particularly when the source is experimental data. First, to correct for variations in gain in different electronic channels the data must be gain matched using pulser data. In addition, the GET electronics has two non-linear background components. In the GET electronics chain, the trace of each channel is stored in capacitors in a switched capacitor array (SCA) until it can be digitized by one of the ADCs on the AGET chip. Each capacitor in the SCA corresponds to a single time bucket in the readout trace. This SCA is one origin of this background. In particular, a component of the background is related to where in the SCA the signal starts. This is often known as the phase-effect. Second, there is a non-linear baseline that is independent of the phase effect. A detailed description of these effects and some correction mechanisms are described by Giovinazzo et al. in [48]. Often the term "Fixed Pattern Noise" is used to refer to the combined effect of these two background components

We will briefly describe the two methods for correcting these effects implemented in the framework. They both rely on correcting for these effects through the subtraction of a signal that acts as a proxy for the combined effects described above.

The first, and simplest, method involves subtracting the Fixed Pattern Noise (FPN) channels on each AGET. Each AGET contains 4 FPN channels, which are fully outfitted channels from pre-amp to SCA that are not connected to any external input. They measure the baseline variation on an event-by-event and AGET-by-AGET basis. If the FPN channels are available, the baseline correction can be done through a simple subtraction:

$$s_{corr}(t) = s(t) - FPN(t) \tag{3.11}$$

where $s(t)$ is the raw trace, $s_{corr}(t)$ is the baseline subtracted trace, and $FPN(t)$ is the average of the four FPN channels in a single AGET chip.

If the recorded data is sparse then reading out the FPN channels can have a significant effect on the rate data can be recorded to disk. As an example, the AT-TPC is instrumented with 10 CoBos, each containing 4 AsAds, This means there are 640 FPN channels to read out each event. Often an event in the detector will only trigger the readout of a few hundred channels. So including the

digitization and readout of the FPNs can more than double the rate of data, decreasing the maximum number of events per second that the DAQ can handle. To reduce this amount of extra data, the zeroth channel in each AGET is force read in lieu of reading out the FPN channels. Because the phase effect due to the SCA is correlated within each AsAd, there is a tight correlation between the traces in each force read ch 0 assuming no charge was deposited on the pad, as seen in Fig 3.5. The average of the four force-read channels in each AsAd can be used as a psuedo-FPN channel for the AsAd, allowing for the bulk of the phase and non-linear background effects to be corrected while only increasing the number of channels that have to be read out by at most 160 in the AT-TPC. The results of the channel zero subtraction are shown in Fig. 3.6.
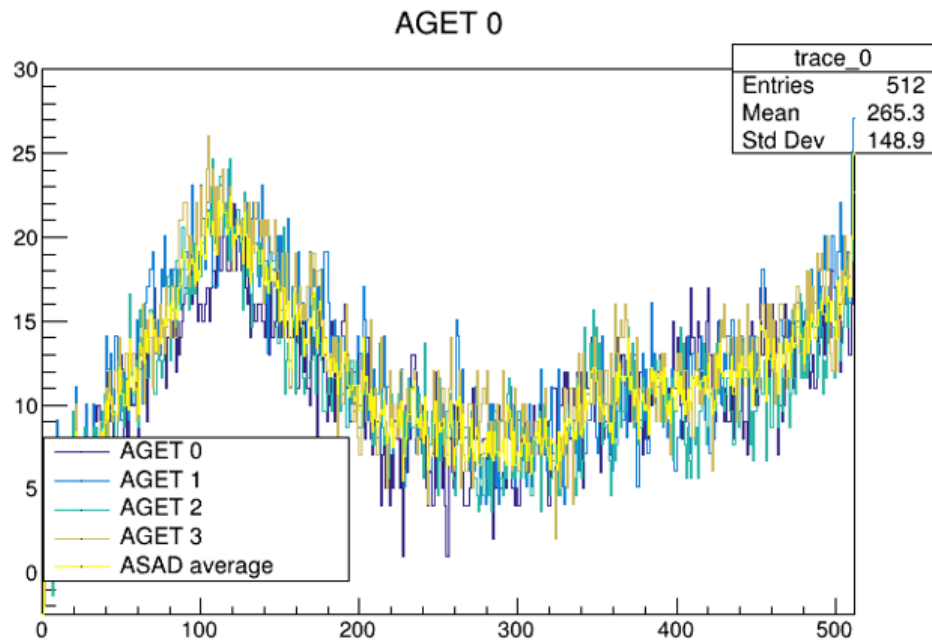
Figure 3.5 Figure showing the traces in the zeroth channel for all four AGETs in a single AsAd, along with the average of the four zeroth channels in yellow.

Most time buckets in each trace do not contain a signal from a charged particle in the detector. A more compact representation of the data would be a collection of "hits" in 3D space, representing the location and magnitude of charge created in the active volume of the detector. The conversion from trace to hits will be referred to as the pulse shape analysis (PSA) task.
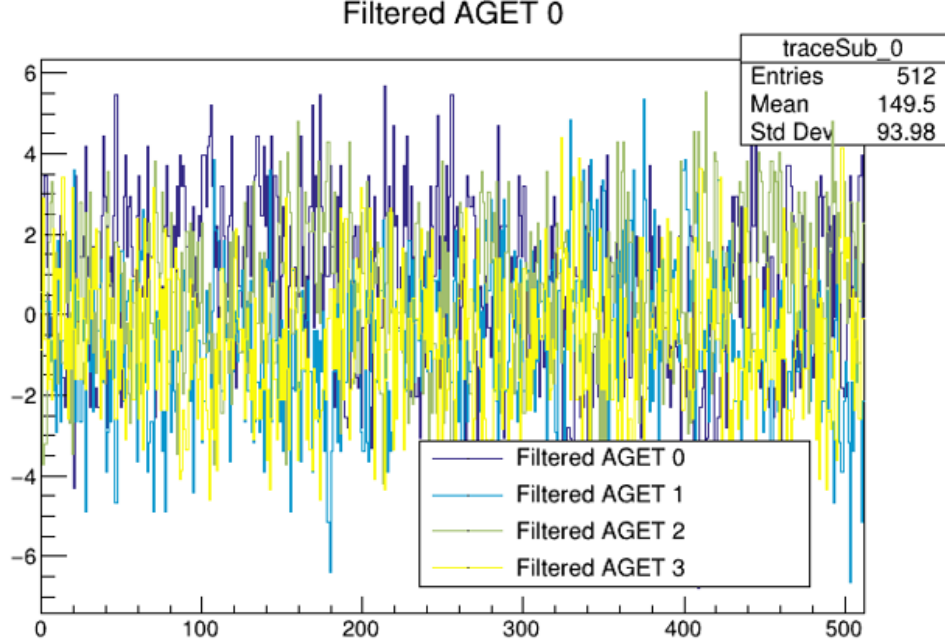
Figure 3.6 Figure showing the zeroth channels for all four AGETs in a single AsAd after the average of the four zeroth channels has been subtracted.

3.4.2 Pulse Shape Analysis

In the simplest case, PSA can simply involve identifying the peak height and location in the trace. When the charge collection time is small compared to the shaping time of the electronics, then the peak height of the trace is proportional to the collected charge [47], and the location of the peak in time can be translated directly into the z-location of the charge deposition through the relation:

$$z = z_{max} - (TB_{win} - t) \cdot v \cdot t_{clock} \tag{3.12}$$

where t is the peak location in TB and the other parameters are given in Table 3.1.

Important to note is this can be complicated somewhat depending on the trigger of the experiment. If the trigger is locked in time with respect to the beam entering the TPC, then the absolute z-position of the hit can be identified. If there is not a way to determine when the beam enters the TPC (that is, the value of TB_{win}), then we would only know the relative z position of hits in an event. Often this external timing information can come from the ionization of the beam itself or an external detector whose signal is fed into the TPC data acquisition system. In the experiment that

is the focus of this thesis, we can see the rise of the signal that corresponds to the beam entering the TPC window.

The assumption that the charge collection time is small compared to the electronics shaping time is an approximation that is often false in AT-TPC data, either because the angle of the track with respect to the beam is too small, or the ion is too far from the pad plane. In either case, the peak height for a given pad scales roughly as the inverse of the collection time of the charge. This can be seen in Fig. 3.7 where we plot the ratio of the peak height of the trace to the total charge collected on a pad for a Gaussian charge profile of varying widths.
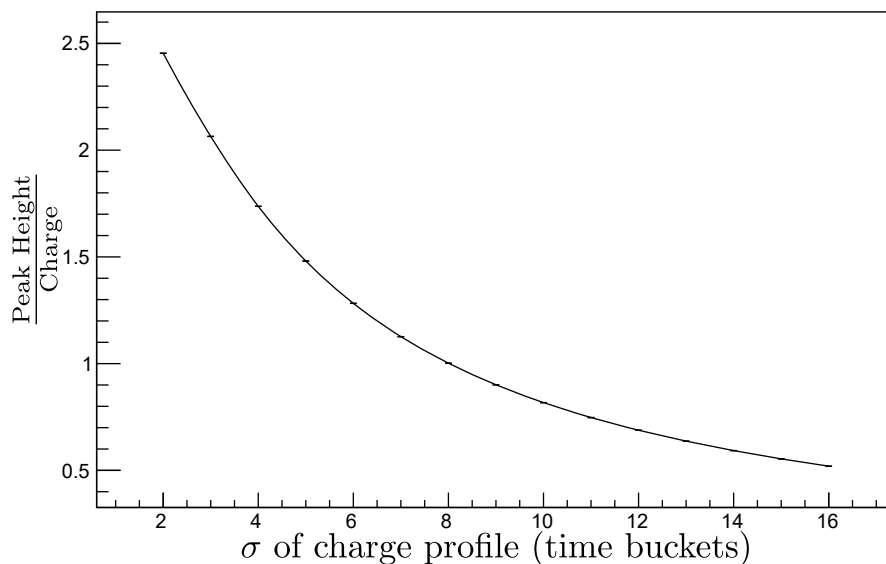
Figure 3.7 Plotted is the ratio between the peak of the expected trace vs the width of the charge profile assuming a Gaussian profile. The peak height is calculated using the nominal electronics response function and the total charge collected is held constant. The peak heights were normalized so the ratio was equal to one when the width (standard deviation) of the charge profile was 8 TBs.

When there is an external magnetic field, these effects change. The diffusion of electrons transverse to the magnetic field is greatly suppressed, while diffusion along the direction of the magnetic field is unchanged. A magnetic field has an additional beneficial effect on tracks that go at an angle with respect to the magnetic field. Even at small angles, the track becomes helical with the major axis parallel to the magnetic field. The curvature of the track means the track does not spent particularly long over any given pad thereby reducing the width of the charge profile. The curvature

55

of the track provides information about the momentum of the charged particle, providing a hook into the energy loss of the particle in the TPC (and by extension the ionization of the TPC gas) beyond what is accessible from the trace. As this thesis focuses on an experiment where an external magnetic field was not applied, we will defer further discussion of diffusion in the presence of a magnetic field to future publications involving data measured with a magnetic field in the AT-TPC.

For experiments, like the fission experiment detailed in Sec 4, where there is no external magnetic field we can nonetheless obtain information about the charge by decomposing the PSA task into two sub-tasks: 1) recovering the charge collected as a function of time from the trace (that is removing the effect of the signal shaping in the electronics) and 2) creating hits in 3D space from the reconstructed charge undistorted by the electronics response.

3.4.2.1 Reconstruction charge from traces

Here we seek to invert the operation discussed in 3.3.2.2. The inversion of a convolution in the time domain is a non-trivial task; however, we can re-frame the problem in the frequency domain to make the problem more tractable.

As a reminder, in the time domain the convolution looks like:

$$s(t) = (i * r)(t) \tag{3.13}$$

where $s(t)$ is the trace, $i(t)$ is the current collected on on the pad, $r(t)$ is the response function of the electronics, and the definition of the convolution operator is given in Eqn. 3.6.

If we apply a Discrete Fourier Transform (DFT), then Eq. 3.13 is transformed into:

$$S(k) = I(k) \cdot R(k) \tag{3.14}$$

where S_k, I_k, and R_k are the trace, the current collected on on the pad, and the response function of the electronics in the frequency domain. We will refer to functions in the time domain as a lowercase letter, and functions in the frequency domain by an uppercase letter. The exact form of the DFT (real to complex) applied to any function, $f(t)$ is given by:

$$F_k = \sum_{j=0}^{n-1} f(t_j) \exp\left(-2\pi i \cdot j \cdot k/n\right) \tag{3.15}$$

where k and j index the arrays running from 0 to $n-1$ where n is the length of the array. In the case of our data the array in question is the trace, so $f(t_j)$ refers to the value of the trace at the jth time bucket. The output F_k has Hermitian symmetry where $F_k = F^*_{n-k}$ so only the first $n/2 + 1$ values of the transform need to be calculated [50].

The inverse of Eq 3.15 is given by:

$$f(t_j) = \frac{1}{n} \sum_{k=0}^{n-1} F_k \exp\left(2\pi i \cdot j \cdot k/n\right) \tag{3.16}$$

where the factor of 1/n is required to normalize the transformations so applying 3.16 after 3.15 returns the original real inputs back [50].

We are now at the point where we can reconstruct the input charge. From 3.14 it follows we can reconstruct the charge through

$$I_k = \frac{S_k}{R_k}. \tag{3.17}$$

This expression, while correct, needs to be adjusted to account for numeric effects arising from R_k. As the high frequency components of the response function are very small, the division in Eqn. 3.17 causes an increase in noise in the high frequency components of the reconstructed current which can degrade our data and make it less useful. To counteract this numeric effect, we introduce a low pass filter, H_k and require the filter to be real so it leaves the phase information untouched. With the filter introduced Eqn 3.17 becomes

$$I_k = \frac{S_k}{R_k} H_k. \tag{3.18}$$

Even-ordered Butterworth filters [51] fill the requirements specified above and their functional form is given by the expression:

$$H^n_k = \frac{1}{1 + \left(\frac{k^2}{w_c^2}\right)^n} \tag{3.19}$$

where n is the filter order (must be even), and w_c is the cutoff frequency. Figure 3.8 shows the effect of the high frequency suppression for 2nd, 4th, and 6th order Butterworth filters all with a cutoff frequency of 10.
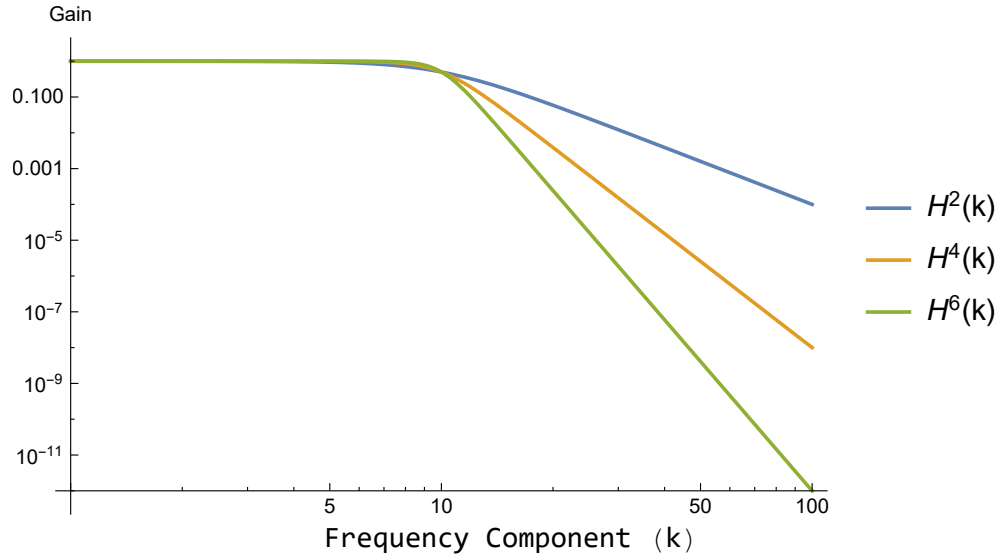
Figure 3.8 Shows the factor each frequency component is multiplied by (gain) for a Butterworth filter of 2nd, 4th, and 6th order all with a cutoff frequency of 10 as a function of frequency component (k).

Eqn. 3.18 using a Butterworth filter allows for the recovery of the useful lower frequency components of the input current on a pad from the trace. Then applying Eqn. 3.16 allows for recovering the current in the time domain. Important to note, this method requires an accurate response function that is experimentally measured. The nominal response given by Eqn. 3.7 is not sufficient to use this method [48].

The introduction of the low-pass filter does introduce some numerical artifacts in the reconstructed charge. Namely an oscillation in the baseline whose amplitude is maximized near the start and end of the charge deposition. Figure 3.9 shows the true and reconstructed charge for a simulated event with different cutoff frequencies. The bulk of the charge in the signal region is well reconstructed. In the case of the low cutoff frequency there are large oscillations in the baseline as seen in Fig. 3.9. Looking at the baseline closely in Fig. 3.10, you can see the increase in the magnitude of the distortion at the edges of the signal as the cutoff frequency decreases and the increase in noise in the reconstructed charge as the cutoff frequency increases. The ideal cutoff frequency will depend heavily on the specifics of the given experiment.
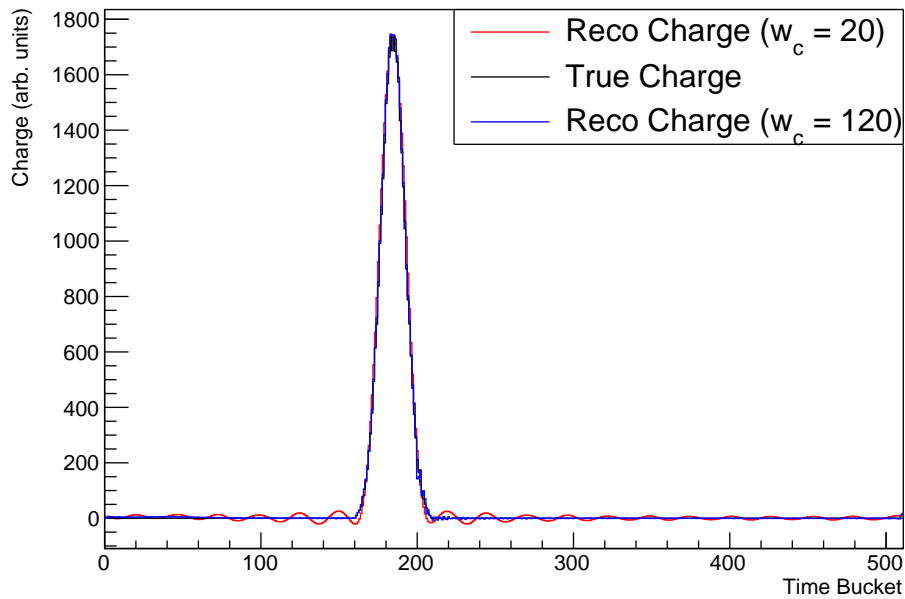
Figure 3.9 Figure showing the true charge (black) and the reconstructed charge using a 6th order Butterworth filter with a cutoff frequency of 20 (red) and 120 (blue). The histograms have been rescaled to emphasize the differences in the line shape.
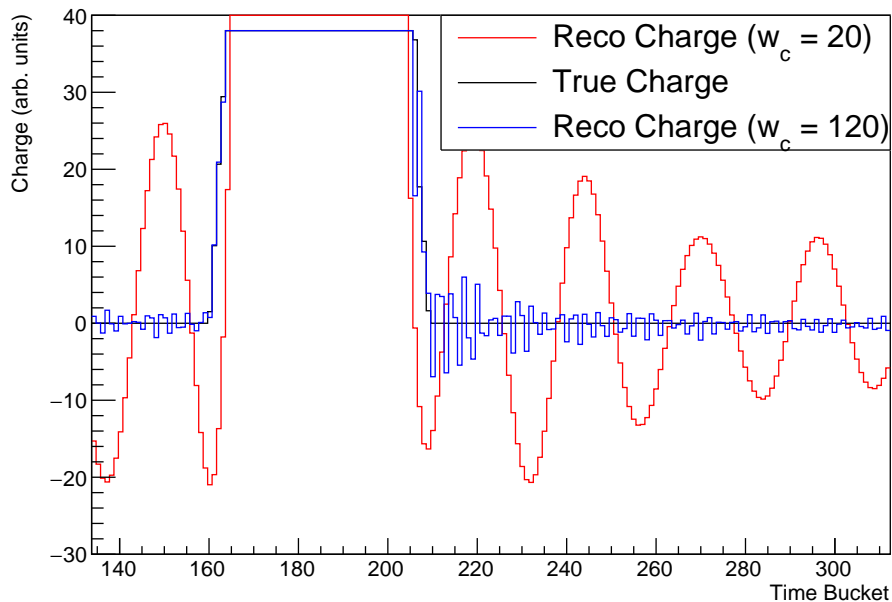
Figure 3.10 Figure showing the true charge (black) and the reconstructed charge using a 6th order Butterworth filter with a cutoff frequency of 20 (red) and 120 (blue). The histograms have been rescaled to emphasize the differences in the line shape.

59

3.4.2.2 Creating hits from reconstructed charge

There are numerous ways to convert from $i(t)$ to hits, and the ideal method will depend on what needs to be optimized for given the goal of the analysis and the nature of the data. Presented here is one method that is usually applicable to constructing hits from reaction products.

Most tracks, other than the incoming beam itself, are at angles sufficiently large or have enough curvature from an external magnetic field, that the track covers a fairly large number of pads. As a result, the ionizing particle spends only a moderate amount of time over any given pad, and due to the effects of diffusion the charge arrives at the pad plane following what is roughly a Gaussian distribution.

By fitting the reconstructed charge with a Gaussian centered around the peak, we can remove much of the noise and many of the artifacts intrinsic to the reconstructed charge. Fig. 4.17b shows an example of the reconstructed charge from an experiment and subsequent fit. The signal is well captured by the fit while the baseline oscillations are suppressed. We then create a hit with x/y position given by the center of the pad and the z position given by the mean of the Gaussian. The charge is taken to be the integral of the Gaussian. We can also provide a measure of the variance in z from the standard deviation of the fit, and estimate the variance in x/y from a combination of the pad shape and the expected magnitude of the transverse diffusion in the gas from the electron drift time, discussed in detail in Sec. 3.6.2.

This fitting method is predicated on the assumption that we have a good a priori understanding understanding of what the collected charge distribution looks like. The method described above works well for most reaction products and can easily be extended to cases where multiple tracks pass over a single pad, but it is ill-suited for the determination of hits in an extended track like the beam or a track with a very forward angle in the absence of significant curvature due to a magnetic field.

3.4.3 Corrections to hit data

Often additional corrections have to be made to the hits (typically to their positions). If the electric field deviates from a uniform field in the z-direction, then we need to correct the hit positions

to account for that deviation. Typically deviations in the electric field arise from the buildup of positively charged ions in the beam region of the detector. We call this positive charge space charge.

The existence of space charge is quite common in studies performed with active-target detectors [52]. Typically the reaction of interest has a small cross-section, and as a result the vast majority of beam particles pass through the detector in more or less a straight line without undergoing a nuclear reaction.

Because positive ions drift so much more slowly than electrons in an electric field, over time a column of positive charge will build up in the beam region. The magnitude of the space charge will increase both with the beam rate and with the amount of energy lost as the beam travels the length of the detector.

The space charge produces an electric field that causes the electrons produced to drift inwards towards the beam region as they drift to the pad plane. Fig 3.11 illustrates this effect. Because there was no magnetic field in the experiment depicted, the charged reaction particles travel in a straight line from the reaction vertex. Far from the reaction vertex, the track appears straight. As the track approaches the vertex, there is a visible curvature due to the space charge. This curvature is manifested by the track bending towards to the beam, whose location is illustrated by the red dashed line in the figure.
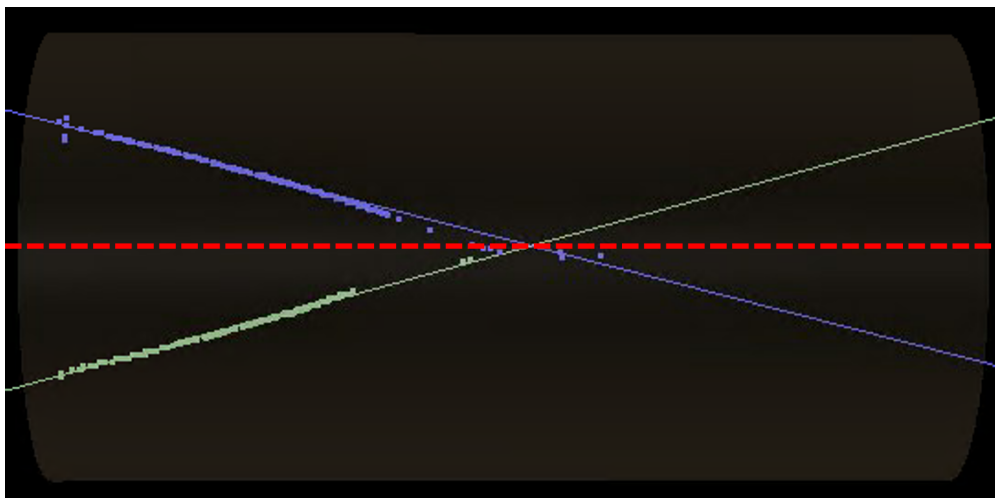
Figure 3.11 3D hit cloud showing the deviation of hits from a straight line near the beam region where they are pulled in towards the beam region due to space charge.

These types of corrections are implemented in the analysis framework through the somewhat poorly named interface `AtSpaceChargeModel`. In fact, all this interface requires is an implementation of a function to covert a 3D point in space to another 3D point in space following the desired correction. I will focus the remainder of the discussion on the most common form of distortion, an electric field with cylindrical symmetry.

3.4.3.1 Correcting hits from a cylindrically symmetric electric field

The correction for any space charge first requires an assumption for the electric field. We will assume the field takes the form

$$\vec{E}_{dis}(\vec{x}) = E_{dis}(\rho, z)\hat{\rho} \tag{3.20}$$

where $\vec{E}_{dis}$ is the distortion to the field. The total field in the detector would be $\vec{E} = \vec{E}_{dis} + \vec{E}_{drift}$. To correct for the E-field we need to calculate the trajectory of the electrons as they drift from the production location to the pad plane. The same method, described below, can be used to both correct simulated data to account for the effects of space charge in the simulation, or to correct experimental data. The only difference is which direction we run time.

The equation of motion for an electron in a gas under the influence of electric and magnetic fields is given by the Langevin Equation:

$$m_e \frac{d\vec{v}}{dt} = e\vec{E} + e(\vec{v} \times \vec{B}) - k\vec{v} \tag{3.21}$$

where k parameterizes a "frictional force" arising from a a series of collisions between the electron and gas particles with a characteristic time $\tau = \frac{m_e}{k}$.

A full description of the dynamics of electrons in gasses for TPCs and TPC-like detectors is given by Blum in [38]. I will focus on the case where there is no magnetic field and Eqn. 3.21 simplifies to

$$m_e \frac{d\vec{v}}{dt} = e\vec{E} - k\vec{v} \tag{3.22}$$

Under these assumptions, we can define the mobility of the electron, μ, where

$$\vec{v} = \mu \vec{E} \tag{3.23}$$

$$\mu = \frac{e}{m_e} \tau \tag{3.24}$$

For most gasses the time it takes an electron to reach the steady state velocity ($d\vec{v}/dt = 0$) is very fast, so we can assume $t \gg \tau$. For He gas, we estimate the characteristic time of an electron in 800 torr He gas at room temperature to be 4.5 ps [53] or the time it would take an electron to drift 37 nm (moving at the steady state velocity).

The assumptions that $t \gg \tau$ and of a electric field that follows the form in Eqn. 3.20 allow us to simplify the solutions of Eqn. 3.22 to a one dimensional ODE where the position of the electron after a short time is given by:

$$\vec{x}(t + \delta t) = \vec{x}(t) + \delta t \mu \vec{E}(\vec{x}) \tag{3.25}$$

where we are using a simple Forward Euler solution to the ODE. This method provides more than sufficient accuracy as shown in Fig. 3.12 where the difference between the exact and numerical solutions are plotted as a function of step size for a line charge at $\rho = 0$.

In reality, the beam is often not directly centered in the TPC, as demonstrated in Fig 2.16. But often the space charge from the beam can still be well approximated by an axially symmetric distribution centered at some point other than (0,0) on the pad plane. The method described above can be simply extended to the case where the beam still travels in the -z direction and is centered at the point $\vec{p} = (x_0, y_0)$ by translating the initial hits by adding the vector $-\vec{p}$ to their position, applying the above method, and then translating the corrected hits back by the vector $\vec{p}$. An example correcting and comparing simulation and data is discussed in detail in Sec. 4.5.3 where this method is applied and validated for the fission experiment that is the focus of this thesis.

3.4.3.2 Reduction of noise in hit clouds

Another common operation on the hit clouds is the removal of spurious noise points in the hit cloud. Often this is done using a K-NN filter [54]. Recent work has been done using machine
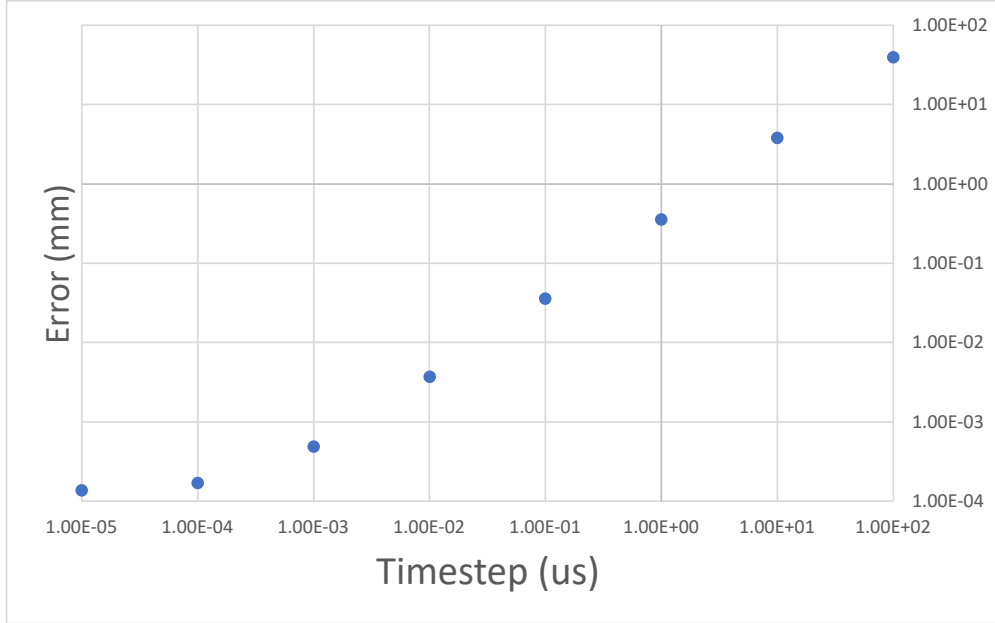
Figure 3.12 Error between exact and numerical solutions for a line charge a $\rho = 0$ as a function of step size in Eqn. 3.25.

learning methods based on the PointNet+ model and the ATTPCROOT framework to improve the efficacy of the noise removal. As none of these techniques are used in the analysis of the fission experiment with the AT-TPC, and are being published in a separate manuscript, we will not discuss them in detail here.

3.5 Track finding through pattern recognition

We define track finding as the task of taking hit clouds and classifying each hit as either belonging to a track candidate corresponding to the path of a single charged particle moving through the detector, or a spurious noise point that is not associated with a particle in the detector. In the language of the framework, this step involves moving from an `AtEvent` containing the hit cloud to an `AtPatternEvent`. The `AtPatternEvent` data structure contains the point-wise identification of every point in the `AtEvent`. The hits that are assigned to a particular track candidate are stored in an `AtPattern` object. Additional validation in the track reconstruction phase is needed to determine if these candidates are true tracks, or if multiple track candidates should be combined into a single track. The `AtPattern` object describes the geometry of the track candidate and contains the logic of drawing 3D representations of the track in the framework's

Pattern Name	Description	Points to define
kLine	Straight line (infinite in both directions)	2
kRay	Ray (straight line infinite in one direction)	2
kCircle2D	Circle projected onto the x-y plane	3
kY	Three rays pointing away from a single vertex	4

Table 3.2 List of implemented patterns that can be used with ATTPCROOT's track finding algorithms and visualization software.

visualization software. A list of implemented patterns (or track shapes the code can currently handle) is given in Table 3.2.

Quite a few methods of track finding have been developed for TPCs over their history. Historically, one of the go-to methods was the Hough transform [55], which was used extensively by low energy nuclear physics experiments like the AT-TPC [20] in the past. It was developed in the 1950s to analyze images of bubble chambers. The Hough transform does not scale well with the number of parameters required to describe the shape of the track, the computational time of the algorithm goes as $O(M^{m-2})$ where m is the number of parameters to describe the shape being searched for and M is the number of values each of the m parameters could take [56]. As a result, the Hough transform becomes cumbersome for shapes more complicated than lines or circles.

Recently, other track finding algorithms have become more commonplace that scale better with more complicated track shapes. At the moment, there are two methods which are currently available for track finding in the framework. The first method is a hierarchical clustering algorithm, TripClust, developed by C. Dalitz et.al. [57]. This algorithm detects and separates curves in 3D space without making any a priori assumptions about their shape. The implementation of this method in the framework is described in Sec 3.5.2. The second method, and the primary focus of this section, is a SAmple Consensus (SAC) algorithm that generalizes the traditional RANdom SAmple Consensus algorithm initially proposed by Fischler and Bolles [58]. It allows for incorporating additional a priori information of the track shapes and constraints on the shapes that are informed by the physics of the reactions being studied. This method is detailed in Sec 3.5.1.

3.5.1 Sample consensus models in active targets

Sample consensus (SAC) is a computer vision technique for identifying shapes (patterns) in hit clouds while excluding outliers. The implementation of SACs in the ATTPCROOT framework is loosely based on the open source Point Cloud Library's implementation of RANSAC [59] and previous work utilizing RANSAC-like algorithms in TPC data [60, 61]. We generalized and specialized the implementation for identifying track candidates in TPC data.

In the original formulation of the algorithm from Fischler and Bolles, the hits in space were sampled randomly and the goal was simply to maximize the number of hits that were consistent with the hypothesised patterns. The method can be made more effective by using additional physics information. An example of this is given in Sec. 4.5.4. There are two main ways to inject additional physics information into the calculation. One is a more intelligent random sampling method, like using a charge weighted distribution to perform the sampling or utilizing some a priori information on where the beam is located in the TPC. The second is in the selection of how we rank the "goodness" of hypothesis, or the estimator. Most commonly this means attempting to minimize a charge-weighted χ^2 rather than maximizing the number of inliers. The effect of exploring some of these generalizations in the analysis of TPC data is discussed in [61].

The implemented algorithm is detailed in Algorithm 3.1. At a basic level, it works by generating a large number of hypotheses for potential tracks in the data using the hit cloud itself. It then tests these hypotheses by how well they describe the data, and identifies which hits are consistent with which of the generated hypotheses. Then we mark the remaining hits as noise. Finally the track shape (or pattern) is fit to the consistent hits. This is an important step as it breaks the constraint that the pattern is defined by the position of hits in the hit cloud.

66

Define method Select parameters to define the model.

Generate Hypothesis Generate N hypothesis by sampling the minimum number of points required to uniquely define the relevant pattern N times.

Rank Hypothesis For each hypothesis calculate its "goodness" by evaluating the estimator. Sort from best (smallest value of the estimator) to worst (largest value of the estimator).

Assign Hits For each of the sorted hypotheses, find the number of remaining hits that are consistent with the hypothesis (n_{con}). If $n_{con} \geq n_{min}$, where n_{min} is the minimum number of hits required to constitute a track, assign those hits to a new track candidate and remove those hits from the hit cloud. After all hypothesis have been checked, tag the remaining hits in the hit cloud as noise.

Minimize Tack Candidates Loop through all track candidates and fit the parameters that describe that pattern using a (optionally charge-weighted) minimization method that is pattern specific.

Algorithm 3.1 Description of SAC algorithm implemented in ATTPCROOT

3.5.2 Hierarchical clustering in active targets

The other primary method of identifying track candidates is through a hierarchical clustering (HC) algorithm. The framework uses TripClust [57] for this task. Since this algorithm is not used by the experiment that is the focus of this thesis, we will only discuss the implementation of this algorithm in the framework and how it compares to the SAC method discussed in 3.5.1.

Unlike the SAC method, the HC algorithm has no intrinsic shape information. It simply looks for clusters of hits in the point cloud. As a result, there is some post-processing that needs to be done to establish the geometric parameters needed to describe the track candidate so we can store the information in an `AtPattern` for further analysis. In addition, if there are any gaps in the track (e.g. the charged particle passed through a dead part of the detector) then often a single track will

be composed of multiple track candidates coming from the TripClust algorithm. A final step in the post processing involves combining track candidates that share sufficiently similar geometric information that they are likely fragments of a single track.

This post processing is done using the SAC method. The HC method has, thus far, only been used in experiments where there is a magnetic field applied to the detector parallel to the drift electric field, so the tracks are helical in nature. For most experiments the $B\rho$ of the reaction products does not change dramatically over the length of the detector. This allows us to use a 2D circle pattern to interrogate the physical properties of the track candidate.

A SAC calculation is done for each track candidate. From this fit, we can extract the position (center) and radius of the helix. This allows us to calculate the arc-length of each point along the helix. By examining the relationship between the arc-length and z for the hits in the track candidate, we can extract the polar angle of the particle, and by extension if the track is forward or backward. After determining the direction of the track, we can extract the initial azimuthal angle of the track as well. The pattern corresponding to the SAC calculation is stored in the track candidate, along with the polar and initial azimuthal angles.

3.6 Clustering hits in tracks

Before tracks can be fit to try and reconstruct physics information about the reactions (See Sec 3.7) it is often beneficial to combine hits into clusters. Some track reconstruction methods, such as a Kalman Filter, require this clustering step. In this case, the cluster is interpreted as a virtual detection plane for the sake of analysis [62].

3.6.1 Identifying hits to cluster

We identify hits to combine into clusters by grouping together collections of hits that are close to each other in space. The goal is to create a list of clusters, whose positions will be denoted as $\vec{X}_i$, where i indexes the cluster ID, from the list of hits whose position will be denoted as $\vec{x}_j$ where j indexes the hit ID. There are two parameters of interest in this model, the first is the radius within which we accept hits as belonging to the cluster, r_{clust}. The second is the minimum distance between two clusters, d_{thresh}. The algorithm is detailed in Algorithm 3.2.

Set parameters Select r_{clust} and d_{thresh}.

Sort hits Sort the hits in the track candidate by their location in z.

Set reference hit Set the first hit $\vec{x}_0$ as the reference hit $\vec{x}_{ref} = \vec{x}_{j=0}$.

Create cluster Create a candidate hit cluster ($\vec{X}_{cand}$) from the hit $\vec{x}_{ref}$. Add each hit ($\vec{x}_j$)
such that $|\vec{x}_{ref} - \vec{x}_j| < r_{clust}$ to the cluster. If $|\vec{X}_{cand} - \vec{X}_i| > d_{thresh}$ for every cluster
already added to the track candidate, then add the candidate cluster to the track. The
creating of clusters is discussed in Sec 3.6.2.

Update reference hit Set the reference hit $\vec{x}_{ref} = \vec{x}_{j=j+1}$ to the next hit in the sorted list.
Return to the previous step.

Algorithm 3.2 Description of clustering algorithm in ATTPCROOT

If the Kalman filter track fitting method is to be used then after the hits have been clustered
according to the above algorithm we apply a smoothing algorithm. The smoothing algorithm is
given in Algorithm 3.3 and increases the number of hit clusters along the track while including
fewer hits in each cluster. The validation of this algorithm is explored in an upcoming paper by the
AT-TPC group where it is used in conjunction with the Kalman filter algorithm briefly discussed
in Sec 3.7.1. We will not explore it further here, as it is not used in the analysis of the fission
experiment that is the focus of this thesis.

Generate reference positions For each pair of neighboring clusters ($\vec{X}_i$ and $\vec{X}_{i+1}$), add $\vec{X}_i$ and $\frac{\vec{X}_i + \vec{X}_{i+1}}{2}$ to the list of reference positions. These reference positions to not at this point represent physical hit clusters.

Create final clusters Remove all clusters currently in the track. For each reference position ($\vec{X}_{ref}$) in the list from the previous step, create a new cluster. Add each hit ($\vec{x}_i$) such that $|\vec{x}_{ref} - \vec{x}_i| < r_{clust}/2$ to the cluster then add the cluster to the track.

Algorithm 3.3 Description of smoothing algorithm in ATTPCROOT

3.6.2 Calculating cluster properties

In order to properly calculate the properties of the hit clusters, care has to be taken when constructing the covariance matrices. This section lays out the logic and mathematics to calculate the properties of hit clusters.

3.6.2.1 Defining hits and hit clusters

A hit, h, is defined as a single point in space, $\vec{x}$, with an associated charge, q. These are generated by the PSA method employed (discussed in Sec 3.4.2). We assume each hit is an independent measurement of a point in space where the charge was actually deposited. The position of each hit has a variance due to the discretization of the pad plane, the initial distribution of where the electrons are ionized (assumed to be negligible here), and the diffusion of the electrons as they drift to the pad plane. Following the work of Shirazi et. al. [63], to each hit, h, we assign the following errors:

$$\sigma_{xy} = \sqrt{\sigma_{0,xy}^2 + Z_{drift}D_T^2},$$
$$\sigma_z = \sqrt{\sigma_{0,z}^2 + Z_{drift}D_L^2}. \tag{3.26}$$

Here $\sigma_{0,xy}$ is the error from spacial resolution of the pad (cm), $\sigma_{0,z}$ is the initial variance in the z distribution stemming from the drift velocity and the PSA resolution (cm), Z_{drift} is the distance the

electrons drifted (cm) and D_T and D_L are the transverse/longitudinal diffusion coefficients of the gas in units (cm$^{1/2}$); specifically, $D_{T/L} = \sqrt{\frac{2\hat{D}_{T/L}}{v_d}}$, where $\hat{D}_{T/L}$ is the normal diffusion coefficient (cm^2/us) and v_d is the drift velocity of electrons in the gas (cm/us).

If we had a TPC with rectangular pads with side length L_{pad}, then [63]:

$$\sigma_{0,xy} \approx L_{pad}/\sqrt{12} \tag{3.27}$$

In principle, the value chosen for L_{pad} should depend on the geometry of the pad plane. Different detectors using the framework used different pad shapes and sizes, and in particular the AT-TPC has a complicated pad plane geometry with triangular pads of two different sizes. For simplicity we take $L_{pad} \approx \sqrt{A_{pad}}$ which would be the width of a square pad of the same area. Since diffusion significantly increases the width of the tracks, this is an adequate approximation. Even though we neglect the pad shape, we do take the pad area into account because it is important in detectors like the AT-TPC where there are pads of varying sizes in the pad plane.

The spread in the position measurement for z from the discritization of the trace is given by:

$$\sigma_{0,z} = v_d \sigma_{0,t} = v_d \sqrt{\frac{nT_c^2}{12}} \tag{3.28}$$

where, v_d is the electron drift velocity (cm/us), T_c is the clock time (period of discretization) in us, and n is the error in time buckets of the PSA method used [64]. The value of $\sigma_{0,z}$ is typically very small, on the order of 1 mm. If we make a measurement of the charge collected over time, like we do in some PSA methods then we can perform a measurement of the variance in the z-direction rather than relying on the estimations in Eqn. 3.26. For example, using the deconvolution PSA discussed in Sec 3.4.2 combined with a Gaussian fit allows us to measure σ_z for the hit instead of estimating it.

A hit cluster is a collection of hits and we can think of the hit cluster as being the underlying distribution that the individual hits are sampling. Like a hit, a hit cluster, denoted H, is defined as point in space $\vec{X}$ with associated charge Q, and with an associated spacial variance. We neglect the inclusion of the charge variance. The estimate for the x-position of this cluster in space we will denote $\hat{H}_x$, with similar definitions for the other spacial coordinates. If N hits combine to make a

single cluster, we denote those hits as the set $\{^1h,^2h,...,^Nh\}$. Each hit has an associated charge, x,y,z position, and variance in spacial position. We will use k to index the hit number in a cluster, and will always mark the hit index as a superscript to the left.

3.6.2.2 Defining weights on hits

There are two weights associated with each hit, one is related to the charge of the hit and the other is related to the spacial variance of the hit. The spacial variance of a hit is given by Eqn. 3.26. In the language of statistics the charge-weighting is a frequency weight and the weighting from the spacial variance is a reliability weighting [65].

Assuming we are in the region where the electronics are linear and gain fluctuations are small, then each ADC count in the data corresponds some number of electrons being collected on the electronics input. As a result, the charge of each hit, q, is proportional to the number of electrons detected. We treat each one of those detected electrons as an independent measurement. For a given hit ^kh, we define the frequency weight (number of independent measurements at the hit position) arising from the charge measurement to be ^kq.

We can think of the position measurement of our hit as being a single measurement of some underlying distribution with an associated mean and variance. For a given hit ^kh with x-position ^kh_x (cm) and variance $(^k\sigma_x)^2$ (cm^2), we define the (reliability) weight of the position measurement to be:

$$^kw_x = \left(\frac{1}{^k\sigma_x}\right)^2 \tag{3.29}$$

following the common convention for reliability weights [66] with similar definitions for the y and z coordinates. In a detector where the variance of the position of hits is roughly the same for each hit in a cluster (i.e. the drift time is about the same, and the spacial resolution of the pads is about the same) then each hit has about the same position weighting and we can safely ignore this complication. For the AT-TPC where there are multiple pad sizes, the inclusion of this position weighting is important, particularly at the boundary from small to large pads.

For the sake of book-keeping and a desire to not have an abundance of summations, we will define the following to be used later in the discussion:

$$Q = \sum_{k=1}^{N} {}^{k}q \qquad (3.30)$$

3.6.2.3 Center of Gravity Estimators

We can now construct the position of the hit cluster $\hat{H}$ as the mean of a set of N hits $\{^1h, {}^2h, ..., {}^Nh\}$. In the case where we are neglecting the weighting from the position variance, the mean in the x position is given by the typical charge-weighted mean:

$$\hat{H}_x = \frac{\sum_{k=1}^{N} {}^{k}q \cdot {}^{k}h_x}{Q} \qquad (3.31)$$

where Q is defined in Eqn. 3.30 and is the total charge of the hit cluster. From [67] the variance is given by the typical estimator for a charge-weighted sample:

$$\widehat{Var}(H_x) = \sum_{k=1}^{N} \frac{{}^{k}q({}^{k}h_x - \hat{H}_x)^2}{Q - e} \approx \sum_{k=1}^{N} \frac{{}^{k}q({}^{k}h_x - \hat{H}_x)^2}{Q}. \qquad (3.32)$$

where Q is defined in Eqn. 3.30 and e is the charge of an electron in the same units as Q. Because $Q >> e$, we can simplify the denominator and neglect the subtraction of e.

If we expand this definition to also include the uncertainty in the position measurement, expressed as the weights ${}^{k}w_x$ defined in Eqn. 3.29, the expression for the mean position in x is given by:

$$\hat{H}_x = \frac{\sum_{k=1}^{N} ({}^{k}q \cdot {}^{k}w_x) \, {}^{k}h_x}{\sum_{k=1}^{N} {}^{k}q \cdot {}^{k}w_x} \qquad (3.33)$$

and the variance is given by:

$$\widehat{Var}(H_x) = \sum_{k=1}^{N} {}^{k}q \cdot {}^{k}w_x({}^{k}h_x - \hat{H}_x)^2 \left/ \left(\sum_{k=1}^{N} {}^{k}q \cdot {}^{k}w_x \right) \right. \qquad (3.34)$$

where the typical expression for the estimator of reliability weighted variance given in [66] been extended to account for charge-weighting. Here we have applied the assumption that $Q >> e$ to simplify the denominator. As a sanity check, its easy to show that Eqn. 3.34 simplifies down to Eqn. 3.32 under the assumption that ${}^{k}w_x$ is the same for all k. In other words, if the variance on the position measurement is the same for each hit in the cluster then it can be safely neglected and

we can just use charge weighting. This assumption is inaccurate in the AT-TPC, particularly along the boundary between different pad sizes.

The arguments above hold for data where there could potentially be a correlation between x, y, and z. If there is a correlation then the off-diagonal elements of the covariance matrix will be non-zero. In principle, these off diagonal elements can be constructed if we knew the position of every individual electron. In that case each hit, $^k h$, would have an associated covariance matrix $^k C$. However, in real TPCs we construct our initial hits of many electrons from a single pad. We cannot know what the covariance between those electrons collected on a single pad is. So for our initial hits before clustering, we assume the off diagonal elements of the covariance matrix are all zero. In that case, we can calculate the covariance of the cluster using the typical charge weighted estimator:

$$C_{ij} = \frac{\sum_{k=1}^{N} {}^k q ({}^k h_i - \hat{H}_i)({}^k h_j - \hat{H}_j)}{Q} \tag{3.35}$$

where i and j index the three spacial dimensions. Here we have again applied the assumption that $Q \gg e$ to simplify the denominator. In this case, we have lost any information we have about the initial spacial variance of the hits. Unfortunately, it is not possible to construct an unbiased estimator of the covariance using reliability weights (i.e. the weights from the position variance) [68]. Ideally we want to be somewhere in-between these two cases. We want to fully use the information we have about the variance of the hits, while not requiring the cluster covariance matrix to be diagonal. As a result, we use the unbiased estimator for the variance using position and charge-weighting (Eqn 3.34) for the diagonal elements of the covariance matrix and the off-diagonal elements are given by the charge-weighted covariance (Eqn. 3.35).

3.6.2.4 Center of Gravity Online Estimators

It is inefficient to calculate the properties of a hit cluster from scratch each time we add an additional hit to the cluster. Ideally, we would like to be able to update the mean, variance, and covariance as we add additional hits.

To start, we will consider the mean. For a hit cluster composed of the set of N hits $\{^1 h, ..., {}^N h\}$ we can define the series $\{^1 H, ..., {}^N H\}$ which corresponds to the mean of the hit cluster after each

74

hit in the set is added. Reworking Eqn. 3.33 to be recursive in nature gives:

$$^{M}H_x = {}^{M-1}H_x + \frac{{}^{M}q \cdot {}^{M}w_x}{\sum_{k=1}^{M} {}^{k}q \cdot {}^{k}w_x}({}^{M}h_x - {}^{M-1}H_x) \tag{3.36}$$

$$^{0}H_i = 0 \tag{3.37}$$

with similar expressions for the other two spacial dimensions.

Likewise we can define a recursive expression for the covariance (Eqn. 3.35). We will denote the numerator of that expression as V_{ij}. If we consider the partial sum to $M \leq N$ in the numerator as $^{M}V_{ij} = \sum_{k=1}^{M} {}^{k}q({}^{k}h_i - {}^{M}\hat{H}_i)({}^{k}h_j - {}^{M}\hat{H}_j)$, then we can define the recursive relationship for the covariance as:

$$^{M}V_{ij} = {}^{M-1}V_{ij} + {}^{M}q({}^{M}h_i - {}^{M}H_i)({}^{M}h_j - {}^{M-1}H_j) \tag{3.38}$$

$$^{M}V_{ij} = 0 \tag{3.39}$$

$$^{M}C_{ij} = \frac{{}^{M}V_{ij}}{\sum_{k=1}^{M} {}^{k}q} \tag{3.40}$$

where $^{M}H_i$ is given by Eqn. 3.36.

Finally, we need a recursive relationship for the full variance (Eqn. 3.34). Following above, we can define the numerator in Eqn. 3.34 to be the partial sum to M:

$$^{M}V_x \equiv \sum_{k=1}^{M} {}^{k}q \cdot {}^{k}w_x({}^{k}h_x - {}^{M}H_x)^2 \tag{3.41}$$

where $^{M}H_x$ is given by Eqn. 3.36. Then we can write the recursive form of the variance:

$$^{M}V_x = {}^{M-1}V_x + {}^{M}q \cdot {}^{M}w_x({}^{M}h_x - {}^{M-1}H_x)({}^{M}h_x - {}^{M}H_x) \tag{3.42}$$

$$\widehat{Var}({}^{M}H_x) = \frac{{}^{M}V_x}{\sum_{k=1}^{M} {}^{k}q \cdot {}^{k}w_x} \tag{3.43}$$

where H_x^{M} is given by the expression in Eqn 3.36 and the sum in the denominator of Eqn. 3.43 can be trivially transformed into recursive relationships.

3.7 Track reconstruction

One of the final analysis steps shared across detectors and experiments is track reconstruction. Here we define track reconstruction to be the task of taking track candidates (found through the methods discussed in Sec 3.5) and extracting the species and energy of the particle. There are two methods for track reconstruction in the framework. The first is based on a Kalman filter (Sec 3.7.1). The second uses a Monte-Carlo process to simulate the detector response to trial events and compares the trial events to the experimental event to identify the track properties (Sec 3.7.2).

3.7.1 Kalman Filter

A Kalman filter is a recursive algorithm that has been used in high energy physics for some time, and is being adapted to low energy physics. It works by examining the "state" of the system at different points (the hit clusters) and predicting the optimal estimation for the state of the system at those same points [62]. The robustness of this method is highly dependent on the physics models used to estimate the transport of the particle through the detector, and on the proper estimation of the covariance matrix for each cluster along the track. As a result, in the context of low energy nuclear physics, it is often used with lighter reaction fragments and at low enough energies where energy loss models are well known. The Kalman filter also benefits from the presence of a magnetic field. The introduction of the magnetic field allows the momentum of the particle to be extracted through the changing radius of the helical track, providing a hook into the energy loss of the particle beyond simply charge information. This reduces the importance of properly reconstructing the enercharge information in the TPC, often one of the more difficult tasks in the analysis of TPC data.

This method is discussed in detail in an upcoming paper by the AT-TPC group. As it was not used in the experiment that is the focus of this thesis, we will leave further discussion of the method to the upcoming paper.

3.7.2 Monte-Carlo Fit

The second method allows for explicitly handling detector effects like missing channels that impact our ability to accurately reconstruct all of the charge that would be required for a Kalman Filter-like method. In this method we use the properties of the track candidate, and any other physics

76

input that may be relevant, to create distributions of the parameters that describe the track. We then simulate numerous events by sampling those distributions and applying the methods discussed in Sec. 3.3. These simulated events are compared to the experimental event looking to minimize some objective function. In the case where the track parameters are poorly constrained by the analysis of the event, this can be repeated where we recenter and reduce the size of the parameter space after a large number of events have been sampled and simulated. A similar method to this was used to analyze the first AT-TPC experiment and is detailed in Bradt et al. [20].

The first step in constructing this method is determining the minimum number of parameters needed to describe the event. For a single track, this is often 6 (3 for the spacial coordinate of the vertex, 2 for the initial direction of the particle's momenta, and 1 for the initial kinetic energy of the particle). For a fission event this would be 10 (3 for the spacial coordinate of the vertex, 2 for the decay angle of one fission fragment in the center of mass frame, 3 for the momentum of the beam at the reaction vertex, and 2 for the A and Z of a single fission fragment). If the beam direction can be safely assumed to be fully in the z-direction, and the vertex location is enough to fully constrain the energy of the beam at the reaction vertex, then this drops to 7 parameters. We will label the vector of these parameters $\vec{\theta}$.

Once the parameters are identified, we then need to create a distribution representing the parameter space for each parameter. In the rare case where we have no constraint from physics or the analysis of an event we will use a uniform distribution. Generally, we use a Student's t-distribution [69], referred to as a t-distribution from here out, for our parameter estimations. The longer tails allow us to still sample (occasionally) far from the mean. If we are wrong in our initial estimation we have a chance to recover the true value of the parameter, while focusing our computational effort near where we think the true value is. The probability distribution function for a t-distribution is given by:

$$P(t) = \frac{\Gamma(\frac{\nu+1}{2})}{\sqrt{\nu\pi}\Gamma(\frac{\nu}{2})}\left(1 + \frac{t^2}{\nu}\right)^{\frac{-\nu+1}{2}} \tag{3.44}$$

where ν is the degrees of freedom, typically taken to be 1 to maximize the tails of the distribution. The variance of the distribution is related to ν where $Var(t) = \nu/(\nu - 2)$ for $\nu > 2$ and infinity for

$1 < \nu \leq 2$.

We assume for each parameter we have both an initial guess, $\hat{\vec{\theta}}$, and standard deviation, $\vec{\sigma}$, from the analysis of the experimental event. We sample Eqn. 3.44 to get t for each parameter and transform it into an estimate for the parameter, θ_i through:

$$\theta_i = \hat{\theta}_i + t\sigma \tag{3.45}$$

where $\hat{\theta}_i$ is our current guess for the mean of parameter θ_i.

Once we have fully sampled the parameters in $\vec{\theta}$ we can simulate the event and detector effects using the simulation code existing in the framework. Importantly, this simulation can account for effects like missing or corrupt channels that we eliminated from the analysis of the experimental event and the effect of space charge on the electrons drifting to the pad plane allowing for the direct comparison of observables between the experimental and simulated events. This comparison is done with an objective function. The objective function is experiment dependent, but usually is composed of similar components laid out in [20].

This process of sampling trial events, and then calculating the value of the objective function is repeated numerous times, often in an iterative fashion. We define the number of trial events to sample with two numbers, the number of rounds (or how many times we recenter the parameter distributions $\hat{\vec{\theta}}$) and the number of iterations in each round. The first round uses a priori parameter distributions. In each successive round, the parameter distributions are re-centered on the trial event that minimized the objective function in the previous round. This allows us to maximize the computation time spent near the true minimum. This method is applied to experimental data in Sec. 4.8.

CHAPTER 4

FISSION IN E12014

4.1 Experimental Design

An experiment was performed at the National Superconducting Cyclotron Laboratory (NSCL) to measure the fission properties of nuclei in the neutron deficient lead region. The setup involved the coupling of HEIST and the AT-TPC. The experiment also served as the commissioning experiment for HEIST. That portion of the analysis, as well as the design and instrumentation of HEIST, is detailed above in Chapter 2. A description of the operating principles behind Active Target TPCs in general can be found in Sec. 3.1 and a brief description of the AT-TPC and its design can be found in Sec. 4.2. The two detector systems used different data acquisition systems and the electronics/software used to link events in the two systems is detailed in Sec. 4.4.

The beam was produced through a fragmentation reaction between a primary Pb^{208} beam, accelerated in the coupled cyclotrons to 85 MeV/A, and a Be^9 production target. The isotopes of interest were then separated using the A1900 fragment separator (see Sec. 2.2) and identified using HEIST (see Sec. 2.5.1). The beam was then slowed down, or degraded, to the energy at which we wished to make the fission measurement. The degradation happened through a combination of energy loss in the detectors in HEIST, particularly the gas in the ion chamber, and a 250 μm iron foil. Finally, the beam entered the AT-TPC running in active target mode with He gas. As the beam passes through the AT-TPC, it can fuse with the He nuclei in the detector. When this happens, the compound nucleus (CN) is in an exited state with some amount of excitation energy (E*). The excitation energy of the CN is dependent on the energy of the beam at the point of the interaction, or reaction vertex. Since the beam looses energy as it passes through the detector, we can measure a range of excitation energies using a single beam energy. This is demonstrated in Fig. 4.1 which plots the expected beam energy as function of depth in the AT-TPC using two different energy loss models. The large variation in the calculated energy loss imply that we need an experimental measurement for the beam energy in the TPC.

Almost immediately after forming, the excited CN will decay. If the excitation energy is above
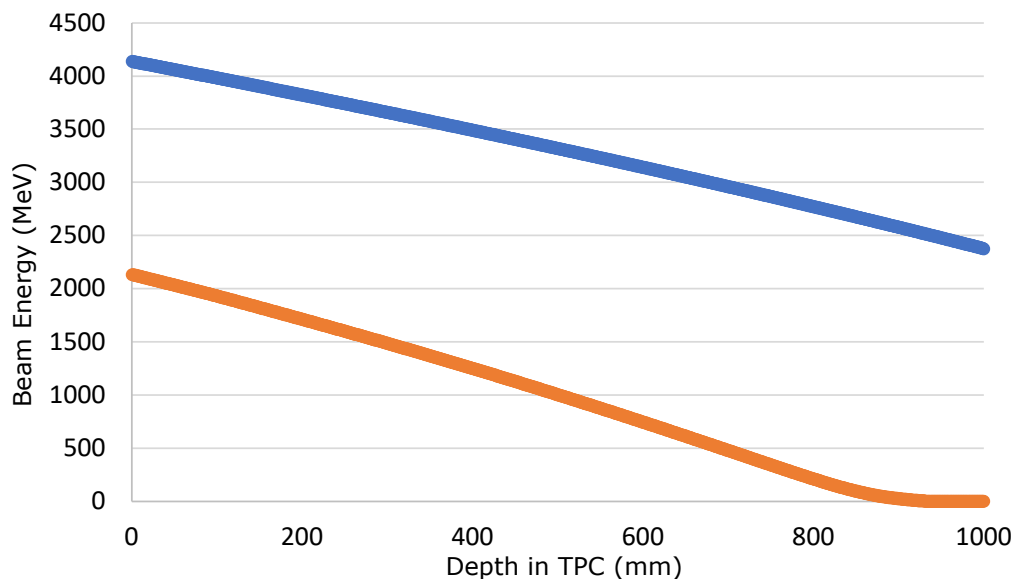
Figure 4.1 Plotted is the energy of the beam as a function of depth in the AT-TPC calculated using the ATIMA energy loss model included with LISE++ (in blue) and SRIM energy loss model (in orange) for ^{200}Bi.

the fission barrier, then the CN can decay via fission. There are other decay mechanisms, but fission, where the CN splits into two fission fragments (FF), is the only one our trigger is sensitive to. These fragments then travel the remaining length of the detector, forming a "V" shape that is characteristic of fission.

The two fission observables this experiment was designed to measure are the probability of fission occurring (the cross-section) and the charge of the fission fragments (element number or Z). Both of these observables depend on how far the excitation energy is above the fission barrier. This thesis will focus on the fission of ^{204}At from a rare isotope beam of ^{200}Bi fusing with ^{4}He, our most abundant species in the beam. We took data using two different energies of the beam entering the TPC. The two different energies were selected by varying the pressure in the ion chamber described in Sec. 2.3.2. We will focus solely on the analysis of the higher energy beam where we have the most statistics.

4.2 Active-Target Time Projection Chamber

The Active Target Time Projection Chamber (AT-TPC) served as the experimental end station for the fission experiment. A detailed description of the AT-TPC and its design can be found in

Bradt et. al. [20]. Here we will give a brief overview of the detector and the salient features of the detector for the analysis of the fission experiment.

As the name implies, the AT-TPC is a TPC that can, and did in this experiment, run in Active Target Mode. Sec 3.1 covers the general operating principles of these types of detectors. The AT-TPC has a cylindrical active volume 1m long, and just over 0.5m in diameter. Fig. 4.2 shows a schematic representation of the detector. The drift field in the AT-TPC is produced by a field cage composed of a series of conductive rings connected with a resistor chain along the edge of the active volume, visualized in green in Fig. 4.2. In this experiment, the voltage applied to the field cage set the magnitude of the drift field to 70 kV/m. There was no magnetic field applied. The detector was filled with 800 torr He gas. Because we were using He with no quenching gas, both a Micromegas [36] and Thick-GEM [37] were used to amplify the electrons before the charge was collected on the pad plane. The entrance window on the AT-TPC was 50 μm PPTA and 4 cm in diameter.
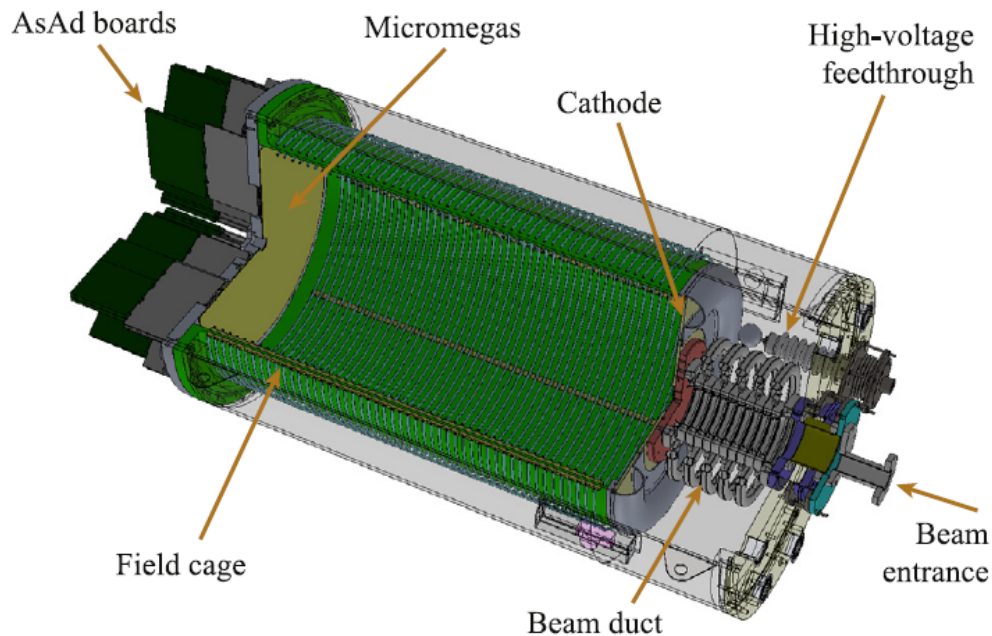
Figure 4.2 Schematic representation of the AT-TPC. Figure from [20].

Important to the analysis is the geometry of the pad plane and the electronics used to instrument the AT-TPC. The pad plane is composed of 10240 triangular pads, seen in Fig. 4.3. The pad plane

contains two different sized pads. The inner hexagonal region it tiled with pads with a height of 0.5 cm, and the outer region is tiled with pads with a height of 1 cm.
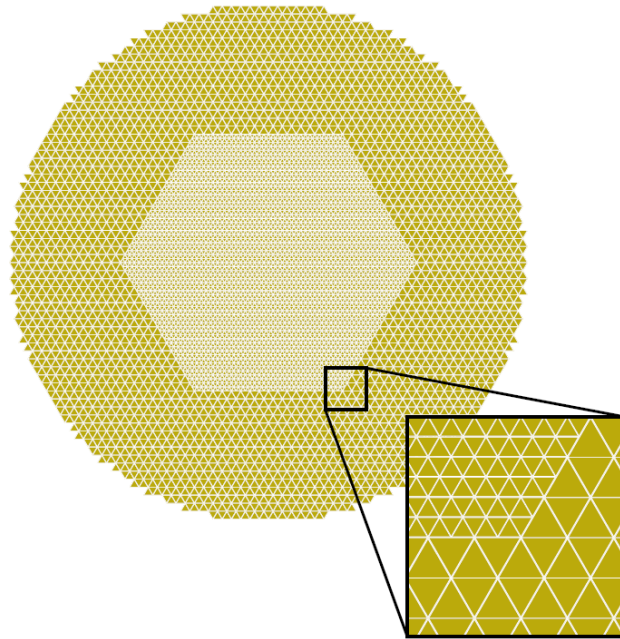
Figure 4.3 Layout of the AT-TPC pad plane. Figure from [20].
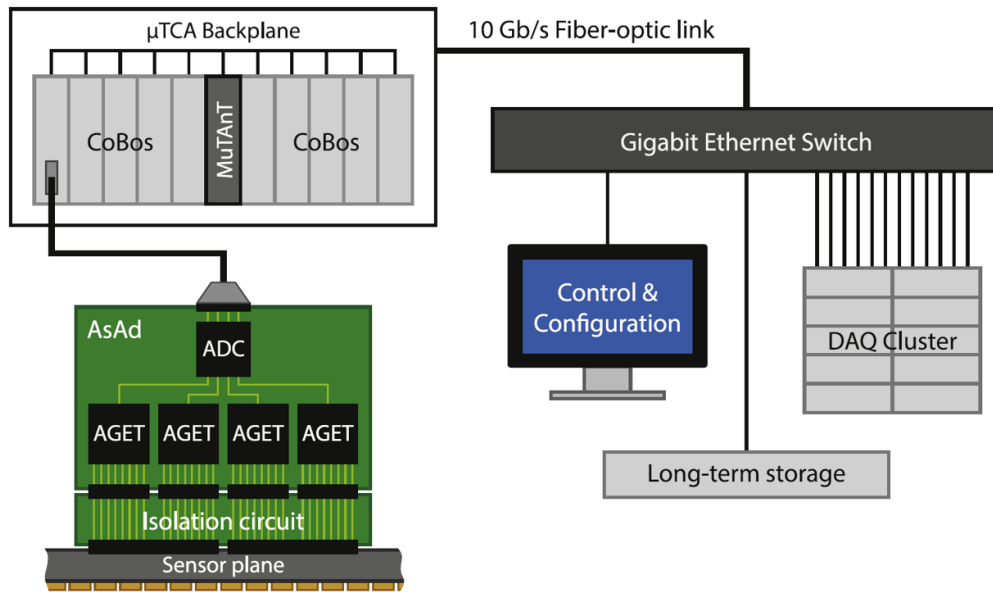
Figure 4.4 Schematic view of the GET system and the ATTPCDAQ. Figure from [20].

The AT-TPC is instrumented using General Electronics for TPCs (GET) [39], and has its own custom data acquisition (DAQ) system which we will call ATTPCDAQ. Fig. 4.4 shows a pictorial

Auxiliary Channel Name	(CoBo, AsAd, AGET, Ch)
MCP US	(10,0,0,0)
MCP DS	(10,0,1,0)
TPC Mesh	(10,0,0,34)
MUSIC	(10,0,2,34)

Table 4.1 List of auxiliary channels used in the experiment and their mapping.

representation of the DAQ. The AT-TPC is instrumented with 10 Concatenation Boards (CoBo). Each CoBo contains four ASIC-ADC boards (AsAd), and each AsAd hosts 4 AGET chips. The AGET chip is a custom ASIC that handles the amplification and shaping of up to 64 input channels, and an additional 4 fix pattern noise (FPN) channels. Each AGET is connected to a 4 channel ADC on the AsAd which is responsible for digitizing the shaped trace. The AsAd then passes the data to the CoBo which sits in a MicroTCA crate. The CoBos are synchronized and triggered by the Multiplicity Trigger and Time (MuTanT), another MicroTCA module. Due to the high data rate each CoBo is read out to its own Mac Mini, indicated by the DAQ Cluster in Fig. 4.4. From there the binary output files (graw files) are merged into a single HDF5 file which is used for the rest of the analysis.

Along with the 10240 channels from the pad plane which are digitized by the first 10 CoBos, we pass a few additional signals in to the ATTPCDAQ through an 11th CoBo. This CoBo is connected to an AsAd that has been modified to allow external signals to be passed in through LEMO connectors. We call these external signals auxiliary channels, and they are treated separately from the other channels in the analysis. Table 4.1 lists the electronic ID and name of the auxiliary channels used in this experiment. The MCP and MUSIC signals are from HEIST. The MCP signals are fanned logic signals from the constant fraction discriminators on the MPC anodes. The MUSIC signal is the output of the charge sensitive preamplifier coupled to the most upstream energy pad that has been split using a linear fan-out. The TPC mesh signal is the output of the charge sensitive preamplifier coupled to the micromegas mesh.

4.3 Trigger

There were two main triggers used throughout the experiment. The first was a simple trigger on the DS MCP anode signal from the MCP that is nearest the TPC, that could be optionally downscaled. This trigger was used extensively in the commissioning of HEIST (see Sec. 2) when the DAQs were decoupled and we were just taking data with the NSCLDAQ.

The second trigger condition was a coincidence between the DS MCP anode and the AT-TPC mesh. Because we expect the beam and fission fragments to both punch through the AT-TPC, the signal on the mesh starts rising at almost the same time as the DS MCP anode signal and remains high until all the charge in the event is collected. The signal on the mesh is amplified using a charge-sensitive preamplifier. This is then passed to a Tennelec spectroscopy amplifier (spec. amp.) which has two outputs: a unipolar used to monitor the operation of the AT-TPC on an oscilloscope, and a bipolar output used to generate the trigger. The timing between the mesh and MCP signals can be seen in Fig. 4.5 where the rise of the mesh (yellow) occurs at nearly the same time as the MCP signal (green).

Ideally, we would like to minimize the amount of unreacted beam events we need to digitize and record to disk. The signal on the mesh does not provide a clear way to distinguish between fission and beam events without some additional hardware. Because we know which pads on the pad plane the beam travels over, we reduce the micromegas gain on those pads. This reduces the magnitude of the mesh signal such that we can set a threshold on the mesh that only fires when a particle exits the low gain region. We do not fully veto the beam region. This is important for some stages of the analysis (for example see Sec. 4.5.3) where we need information on the traces in the beam region.

The reduction in gain in the beam region is performed using a Smart ZAP, see Fig. 4.6 for a simplified schematic. The Smart ZAP is used to apply an external voltage to a section of the pad plane. This reduces the potential difference between the pad and the micromegas mesh, reducing the gain [70]. The region of the pad plane where the gain was reduced is marked in red in Fig. 4.7. The smart ZAP did not fully cover the entire beam region, and there was a small section of the
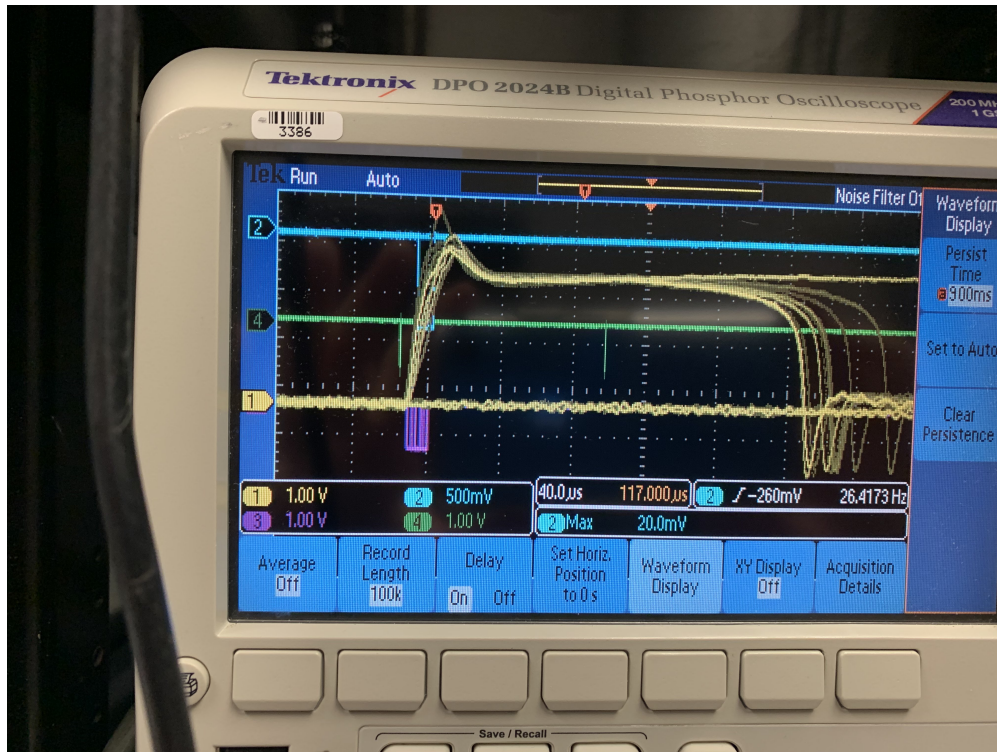
Figure 4.5 Yellow is the unipolar output of the spectroscopy amplifier. Green is the DS MCP anode signal. Purple is the output of the coincidence trigger between the SCA on the bipolar mesh signal and the DS MCP signal. Blue is the raw trigger.
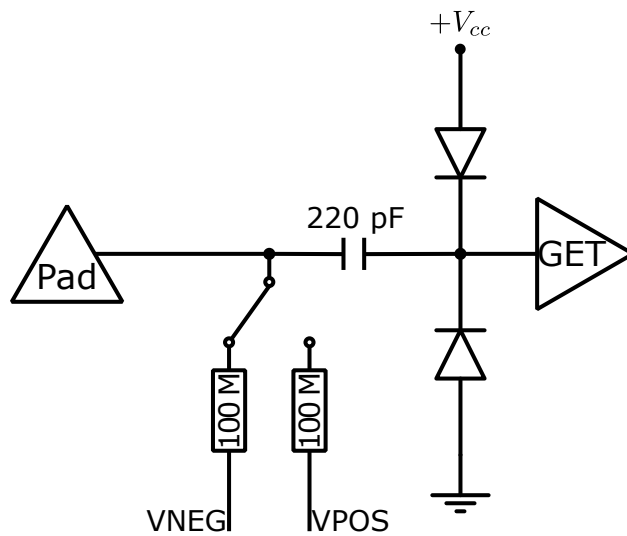
Figure 4.6 Schematic representation of the Smart ZAP. The switch is computer controlled and determines the bias applied to the pad (VNEG, VPOS, or floating).

pad plane that the beam would occasionally hit that was capable of creating a trigger. This false trigger on the unreacted beam is responsible of the majority of the events we recorded. Section 4.5.1 discusses how we separate beam from fission events.
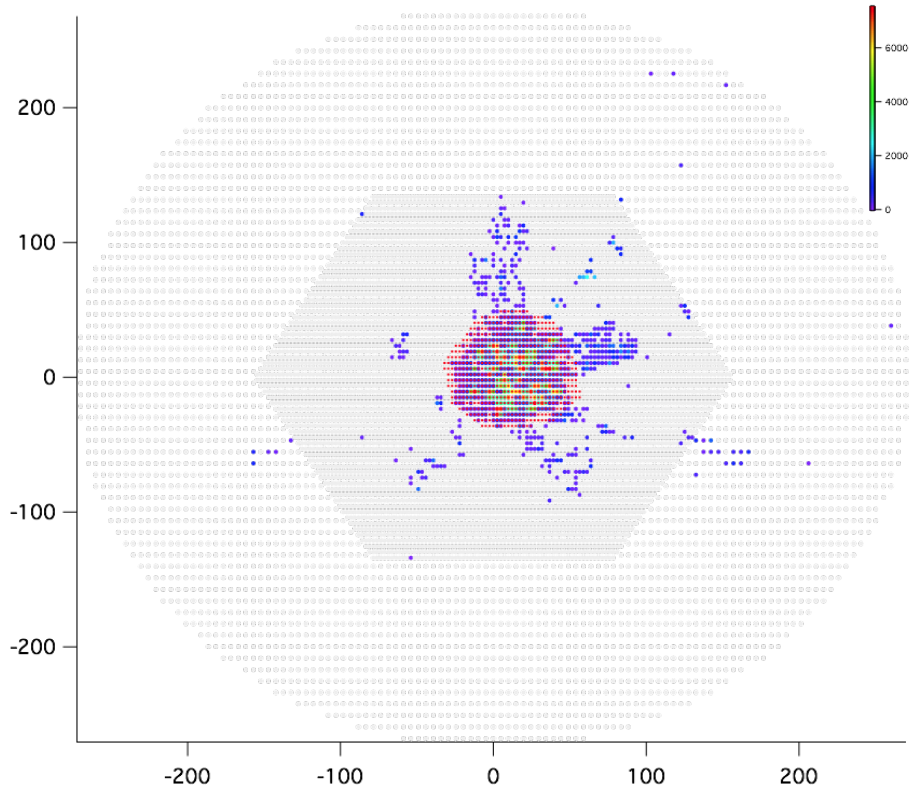
Figure 4.7 Pad plane of the AT-TPC with the low gain region marked in red.

The logic diagram for generating the trigger can be found in Fig. 4.8. The bipolar signal from the mesh is passed to an ORTEC timing single channel analyzer (SCA), producing a fast logic signal, which is stretched by a gate and delay generator (GDG). This stretched signal is what we use to form the coincidence between the mesh and the DS MCP anode. The MCP signal used in the coincidence is also stretched by a GDG.

Usually, while taking data, we use an "or" between the two triggers. Regardless of what is triggering the event, the coincidence or DS MCP trigger, we want to keep the time of the trigger fixed with respect to the DS MCP anode signal. We ensure this consistency (or "re-timing") by forming a second coincidence between the OR of the two triggers and a delayed copy the original
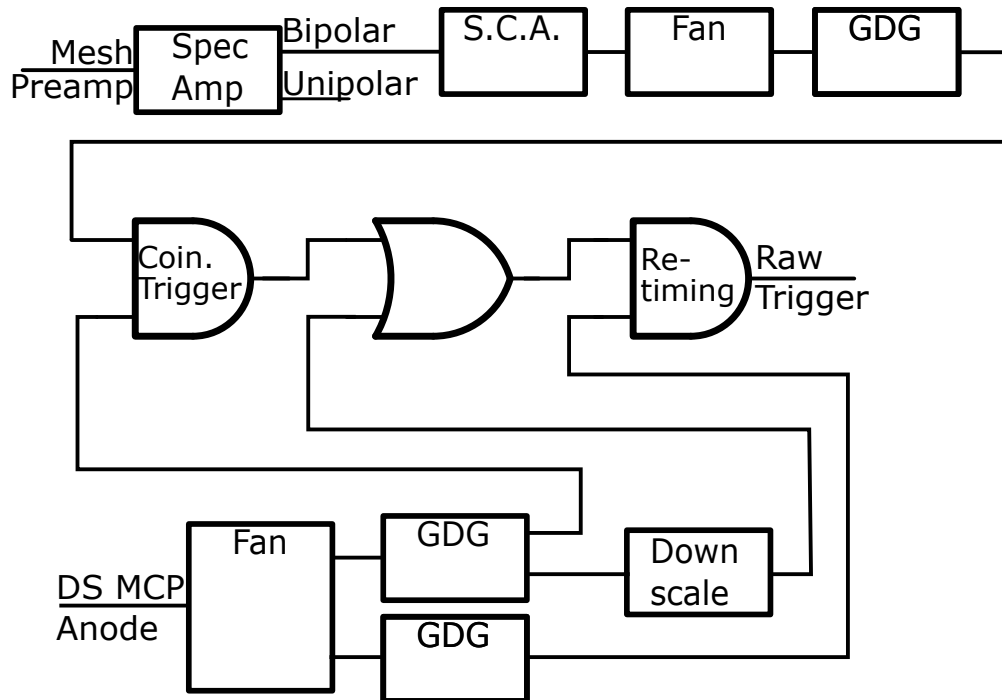
Figure 4.8 Logic diagram depicting the circuit used create the raw trigger. Symbols are IEEE Std 91a-1991 [71].

DS MCP anode signal that is delayed long enough it always goes high after the two triggers. This is seen in Fig. 4.5 where the live trigger (blue) is fixed in time with the DS MCP anode signal (green) despite the shifting time of the coincidence trigger (purple). The output of this second coincidence module is our raw trigger. The next section describes how this raw trigger is treated to ensure the two DAQs in use remain synchronized.

4.4 DAQ linking

This experiment contains two distinct data acquisition (DAQ) systems, one for the AT-TPC discussed briefly in the previous section we call the ATTPCDAQ, and the other for the HEIST system. HEIST uses the NSCLDAQ [72], now FRIBDAQ, as its data acquisition software. These two DAQs are decoupled and responsible for reading out each event individually. We require a way to associate events in the NSCLDAQ, which provides the PID of the beam, with events in the ATTPCDAQ where we actually measure fission. We call this processes of associating events between the DAQs "DAQ linking".

4.4.1 Electronics

We ensure this linking between DAQs two ways. First we have a shared timestamp between the two DAQs we use to link events. Second, we pass some physical signals between the DAQs as discussed in Sec. 4.2 with the auxiliary channels. A SIS3820 VME Scaler was used to generate a 10MHz clock signal that was passed to both the MuTanT and the SIS3820 itself running in latching scalar mode. The SIS3820 was read out by the NSCLDAQ. To ensure the timestamps are synchronized, the electronic circuits in Fig. 4.9 were used.

The first circuit (Fig. 4.9a) was used to clear, or reset, the timestamps at the start of each run so we always count up from 0 at the start of each run. The input to this circuit is the OR of the busy signals from both DAQs (the total busy) and a signal from the NSCLDAQ we call O2. O2 is a NIM signal from the NSCLDAQ VME crate that goes high at the start of a run, and remains high until the end of the run. When both DAQs are ready to take data, the total busy goes low, and O2 goes high. This triggers the RS-latch to go high, and the leading edge discriminator attached to the latch output creates a NIM logic pulse that is passed to both DAQs to clear out the timestamps. To reset this system between runs (i.e. reset the latch) we need to generate a NIM pulse on the end of a run. This is done by monitoring the inverted O2 signal ($\overline{O2}$). When the NSCLDAQ run ends, O2 goes low, so $\overline{O2}$ goes high. The leading edge discriminator attached to $\overline{O2}$ fires, resetting the latch.

The second piece to keeping the DAQs synchronized is making sure the trigger sent to both DAQs is synchronized. That is, we want to ensure both DAQs get the trigger at the same time, and they get the same number of triggers. This is achieved through the circuit diagramed in Fig. 4.9b. Our total busy is constructed by ORing the NSCLDAQ busy, ATTPCDAQ busy, and a third signal (fast busy) that is the live trigger stretched to a length of $\sim 130~\mu$s by a Gate and Delay Generator (GDG). This third signal is included because of the different timescales in reading out the two DAQs. The NSCLDAQ digitizes and reads out the relatively fast signals from HEIST within 80μs of receiving the trigger as seen in Fig. 4.10. The ATTPCDAQ busy does not go high until the data starts being digitized and read out, which only occurs after the full signal has been collected on the switched capacitor array in the AGETs. This means the busy does not go high until $\sim 130~\mu$s
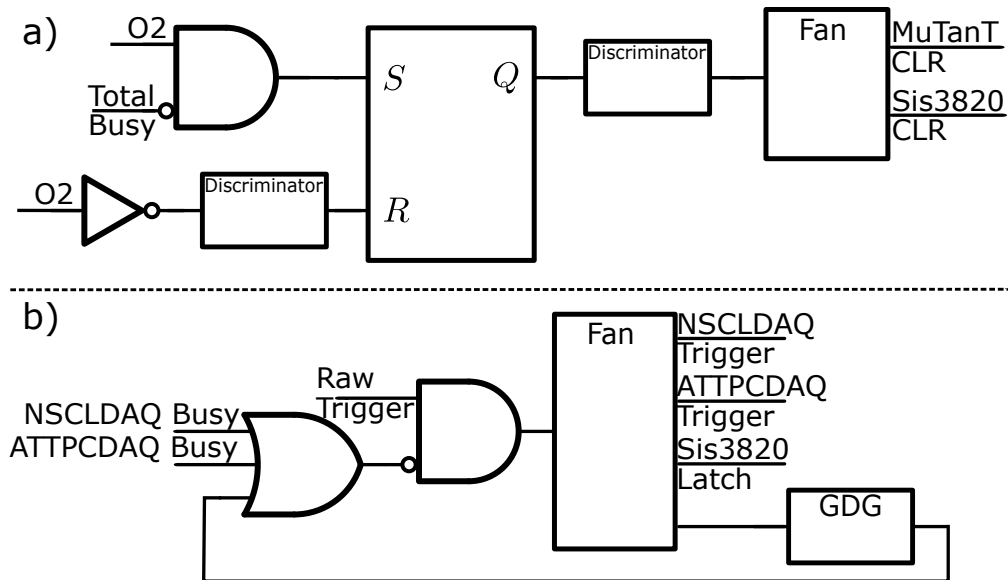
Figure 4.9 a) Logic diagram depicting the circuit used to clear the timestamps at the start of each run. b) Logic diagram depicting the circuit used to create the live trigger to keep the DAQs synced. Symbols are IEEE Std 91a-1991 [71].

after the trigger. As a result, if the total busy were just an OR of the two busies, there would be a $50\mu s$ window where the NSCLDAQ could be triggered again as seen in Fig. 4.10. This double triggering would create spurious uncorrelated events in the NSCLDAQ readout. By stretching the live trigger and adding it back into the busy, we keep the trigger vetoed until the ATTPCDAQ has finished its readout.

4.4.2 Software

We link the two DAQs in software by using the timestamp to compare the time interval between events. We chose to match events on the interval rather than the absolute difference between the timestamps in the two DAQs to increase the robustness of the linking. For a period of time, we did not have access to the timestamp in the ATTPCDAQ from the 10 MHz SIS3820 clock. We only had the timestamp from the internal 100 MHz MuTaNT clock. The drift between the ratio of the two clock frequencies over time is too large to match the absolute difference between timestamps, but events can still be matched by matching the interval between events.

In addition, it is much easier to tell if events are being mismatched when using the interval. To match events using the absolute difference between timestamps in the DAQs, one must determine
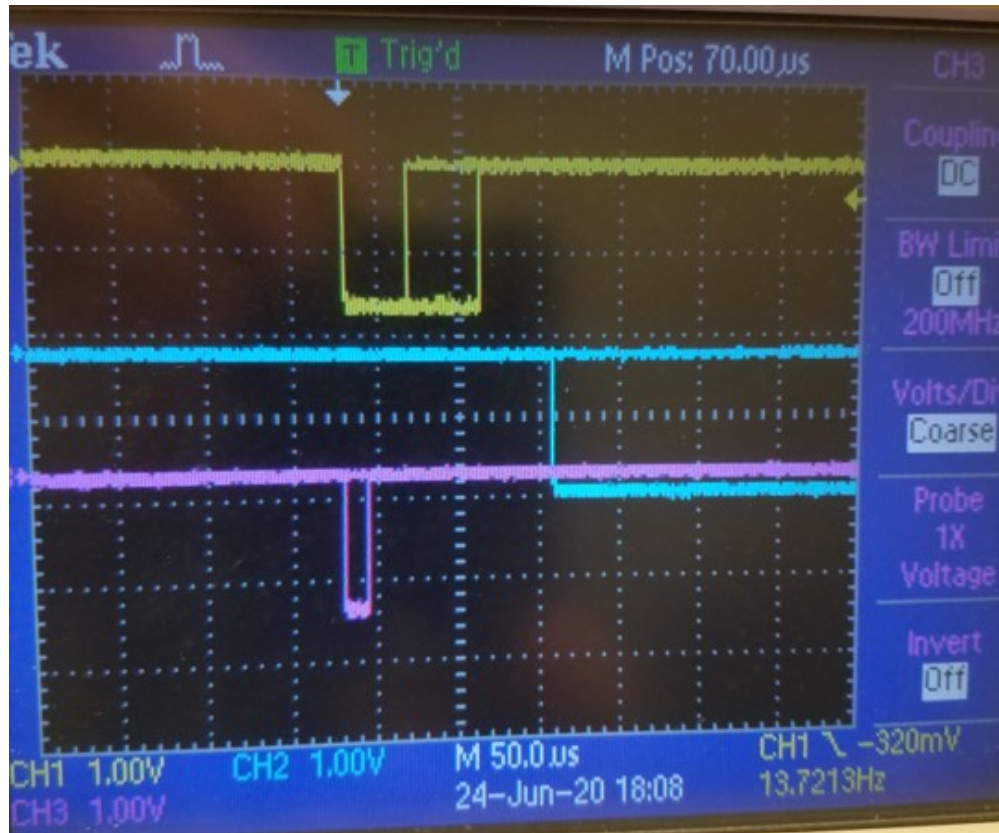
Figure 4.10 Yellow is the busy signal from the NSCLDAQ. Blue is the busy from the ATTPCDAQ. Pink is the live trigger. The NSCLDAQ busy goes low before the ATTPCDAQ busy goes high allowing the NSCLDAQ to be double triggered in the 50 μs where there is no busy.

the expected offset between the two timestamps (the offset arises from effects like differing cable lengths in the electronics). If that offset is found by accidentally by making an incorrect initial guess for which events at the start of the run are matched, then each later event in the run will be mismatched. This is not a problem with matching on the interval where the offset is subtracted away. If an event is mismatched it will become immediately apparent when future intervals do not align.

This additional robustness is also beneficial when, as is quite common, the timestamp from the SIS3820 clock is corrupted in the ATTPCROOT DAQ. For stretches at a time, the timestamp which is a 64-bit number, loses the upper 2 words (32 bits) and lower 12 bits of information. That is, the timestamp `0x000000008015f1e8` from the NSCLDAQ should be matched to the timestamp `0xFFFFFFFF8015f800` in the ATTPCDAQ. We can partially recover the corrupted timestamp by

zeroing out the corrupted upper two words; however, we loose a large amount of precision. We expect the difference in the timestamps in the two DAQs to vary as much as ±2048 from the missing 12 bits of precision while the timestamp is corrupted. This can be seen in Fig 4.11 where we plot the difference between the timestamp interval for the NSCLDAQ, I_{NSCL}, and the ATTPCDAQ, I_{TPC}. The region where the timestamp is corrupted can be seen clearly, and the magnitude in the fluctuations match with what we expect given the missing information. Luckily, the timestamp in the ATTPCDAQ from the MuTaNT's internal clock is not corrupted. This means we can use a comparison between the interval calculated using the MuTaNT clock, I_{MuTaNT} in the ATTPCDAQ with the Sis3820 clock in the NSCLDAQ, I_{SIS} to validate our event linking. This is seen in Fig 4.12, which is the same run shown in Fig. 4.11. As expected, assuming we are matching events properly, there is no evidence for a mismatch in Fig. 4.12.
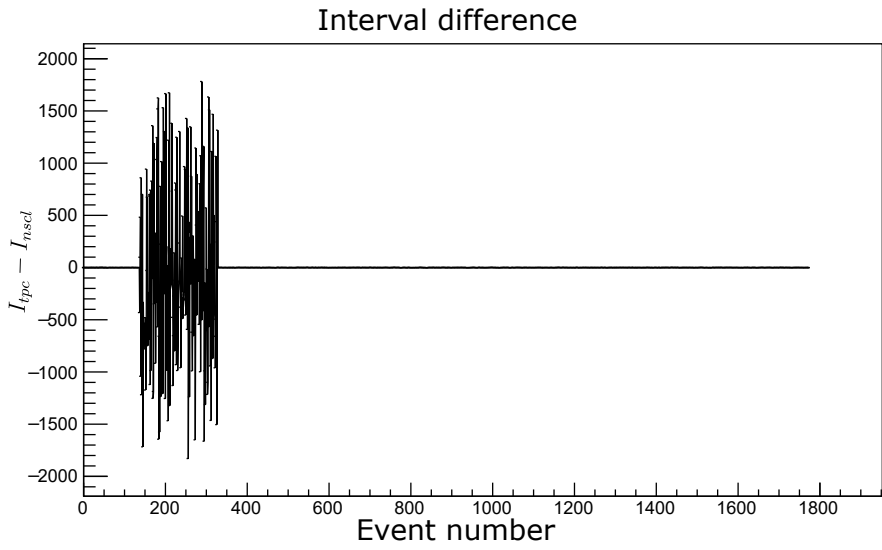
Figure 4.11 Interval difference using the timestamps from the 10 MHz SIS clock. The timestamp in the ATTPCDAQ was corrupted for a series of events, causing the absolute difference in the timestamps to vary away from 0 despite the events still being properly linked.

To ensure events are properly linked, we can use the physical signals shared between the two DAQs. We focus on the signal from the most upstream rectangular pad in the HEIST MUSIC detector. Fig. 4.13 shows the correlation between the peak height of the shaped signal recorded by a peak-sensing ADC in the NSCLDAQ and the peak height of the trace in the ATTPCDAQ.
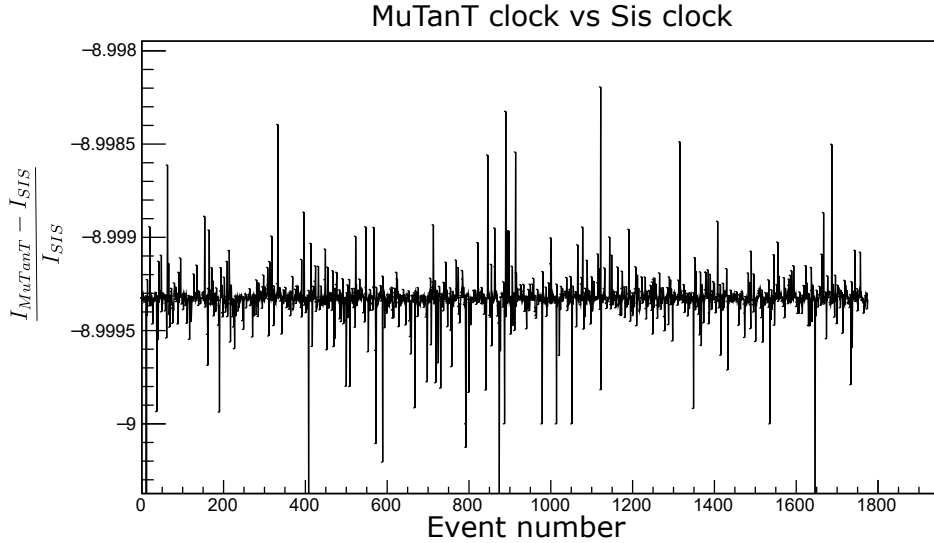
Figure 4.12 Scaled interval difference using two different clocks, internal 100 MHz for the ATTPC-DAQ (I_{MuTanT}) and 10 MHz for NSCLDAQ (I_{SIS}). The value of what is plotted on the y axis should be $1 - f_{MuTant}/f_{SIS} = 1 - 100/10 = -9$. The timestamp from the MuTanT clock was not corrupted and there is no discernible place where we are not properly associating events.

The trace in the ATTPCDAQ is the output of the charge sensitive preamplifier, and as such is quite susceptible to the impacts of pileup due to the long exponential tail. This expresses itself in the plot as the more spherical "shadow". The events where pileup was not in issue lie along the bright oval. Attempts to apply a trapezoidal filter on the traces offered marginal improvement. Fig. 4.14 shows the same correlation between the two DAQs for the same run as Fig. 4.13 but without properly linking the events. As expected, the events in Fig. 4.14 look like a spherical blob.

4.5 Reconstructing fission events

Our goal in reconstructing fission events is to go from an `AtRawEvent`, the collection of traces on the pads, to a 3D reconstruction of the event. From this reconstruction we can pull information like the vertex location, folding angle between the fission fragments, and the energy loss curves of the fission fragments. This information then allows us to identify the charge, Z, of the fission fragments (see Sec. 4.8).

The process of reconstructing these events roughly follows the analysis pathway laid out in Fig. 3.1. We start by applying the selection algorithm laid out in Sec. 4.5.1 to ensure all of our events are fission events. For the selected fission events, we construct hits as discussed in Secs. 3.4.2
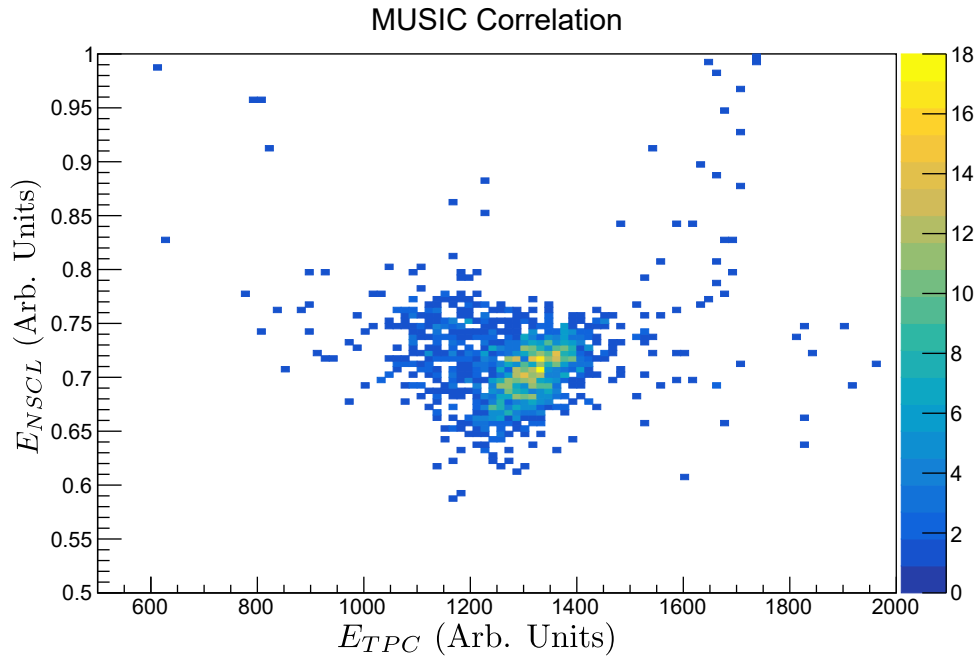
Figure 4.13 Energy in most upstream pad in MUSIC digitized by the NSCLDAQ and ATTPCDAQ. The correlation is evident, along with the effects of pileup, which cause the "shadow" seen where the energy recorded in the ATTPCDAQ is lower than expected given the energy recorded in the NSCLDAQ.
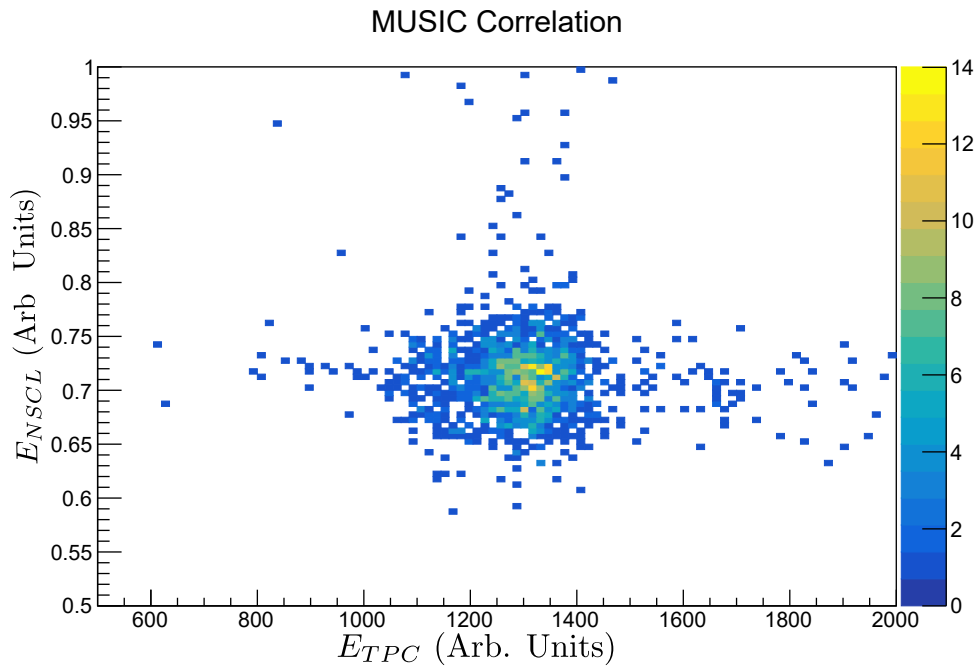
Figure 4.14 Energy in most upstream pad in MUSIC digitized by the NSCLDAQ and ATTPCDAQ where events have been mismatched. As expected, there is no correlation between the two energy signals.

and 4.5.2. Those hits are then corrected for the effects of space charge as described in Sec. 4.5.3. Finally we use the sample consensus method, described in Sec. 3.5.1, to identify the hits associated with the two fission fragments and beam, and then fit these hits with a "Y" pattern as discussed in Sec. 4.5.4.

4.5.1   Separating fission events from beam events

As mentioned in Sec. 4.3, a large number of unwanted beam events were still digitized even after application of the low gain Smart ZAP region. It was necessary to develop methods to sort through the data and mark the beam events for removal, as they constitute the vast majority of our events. For the average run with length of around 1 hour, approximately 10^6 events meet the trigger requirements and are recorded, with only 10^3 to 10^4 of those coming from fusion-fission reactions. The remainder are not useful to analyze and waste significant amounts of computational time if not removed from the analysis. Several parameters that can be quickly extracted from the events were used to determine whether events are fission or not.

For example, one can estimate the location where charge was produced through ionization of the gas in the TPC using the TBAvg PSA method discussed in Sec. 4.5.2. One can then easily calculate the spread of charge across the pad plane as a function of z by computing the standard deviation of the x and y positions of all the hits in a time bucket slice. In the case of a beam event, the standard deviation of hits within each slice should be small and mostly constant, as unreacted beam particles simply continue through the TPC in a straight line. In the case of a fission event, the slices containing the beam (pre-vertex) will show a small and constant deviation. The slices after the vertex containing the two fission fragments will show a sudden large deviation that continues to grow towards the pad plane. This is demonstrated in Fig. 4.15.

The sorting algorithms used to label the events combine this study of standard deviation with other similar basic parameters. These other parameters all derive from a SAC calculation looking for lines (the line pattern) in the data. The parameters extracted from this calculation are: 1) the number of lines identified by the SAC. 2) the locations of the hits closest to the pad plane and closest to the window for each identified line. 3) the angle of the identified lines with respect to the
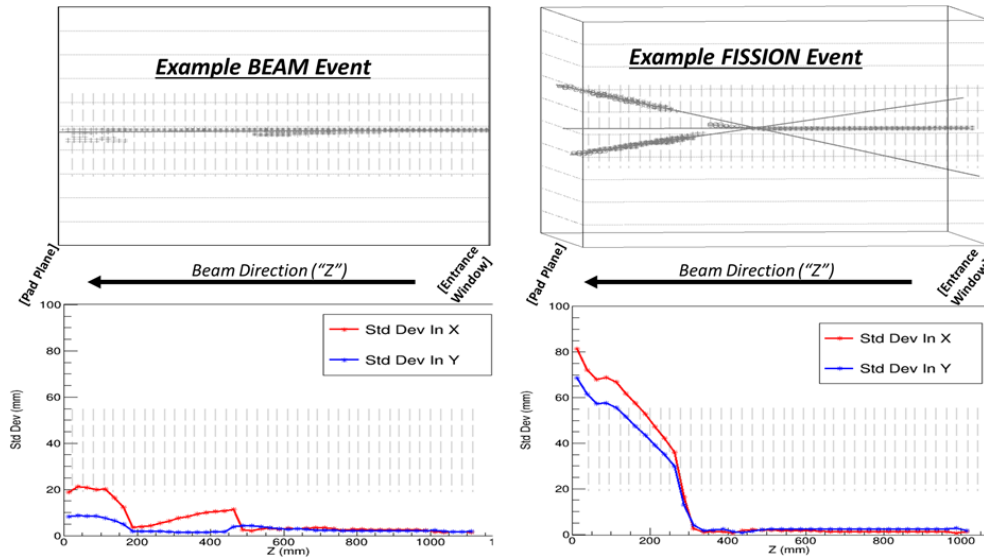
Figure 4.15 Two events are plotted, the left is an unreacted beam event and the right is a fission event. The bottom panels plot the standard deviation of the charge in x (red) and y (blue) for the two events. The standard deviation of the charge in the fission events increases dramatically after the reaction vertex in fission events, but remains small for beam events.

	Known Fission	Known Beam
Predicted Fission	61	0
Predicted Beam	0	2220
Predicted Other	9	46

Table 4.2 Performance of the algorithm for sorting fission events from beam events.

z-axis.

A set of hand labeled events were used to tune values of these parameters until appropriate amounts of unwanted data could be filtered out. The sorting algorithm sorts each event into three potential categories: "Beam" for events that are definitely unreacted beam events, "Fission" for events that are definitely fission reactions, and "other" for events where we are uncertain of the proper ID. The algorithm results on this labeled set can be seen in Table 4.2. By combining the "fission" and "other" categories we can select all fission events at the cost of included a few unwanted events. Our analysis in this chapter will use the pure fission cut.

4.5.2 Pulse Shape Analysis

The pulse shape analysis (PSA) methods used in this analysis need to meet two primary goals. First, we need an accurate reconstruction of the charge deposited in the TPC along the fission

fragment tracks. Second, we need an accurate position measurement across the TPC, including measuring the beam track to successfully fit events with a Y-pattern as discussed in section 4.5.4.

As discussed in a previous chapter (3.4.2), if the charge collection time is not short compared to the shaping time of the electronics, we must use a PSA method like the deconvolution method discussed in Sec. 3.4.2.1. In E12014, the peaking time of the electronics was 720 ns and the width of one time bucket 320 ns. As seen in Fig 4.16, the expected FWHM of the charge profile at the pad plane due to longitudinal diffusion (D_l = 0.0055 cm^2/us) exceeds the peaking time of the electronics ~10cm away from the pad plane. In reality, the collection time of the charge in a pad exceeds the shaping time closer to the pad plane due to other effects such as track angle. As a result, the peak height of the trace has a strong dependence on the width of the charge collected as demonstrated in Fig. 3.7. This implies that to get an accurate measurement of the charge deposited by a fission fragment as it moves through the TPC we must use the devolution PSA method discussed in Sec. 3.4.2.1. As discussed previously, there are a number of parameters, mostly around the required low-pass filter, that must be set. The parameters used for this experiment are listed in Table 4.3.
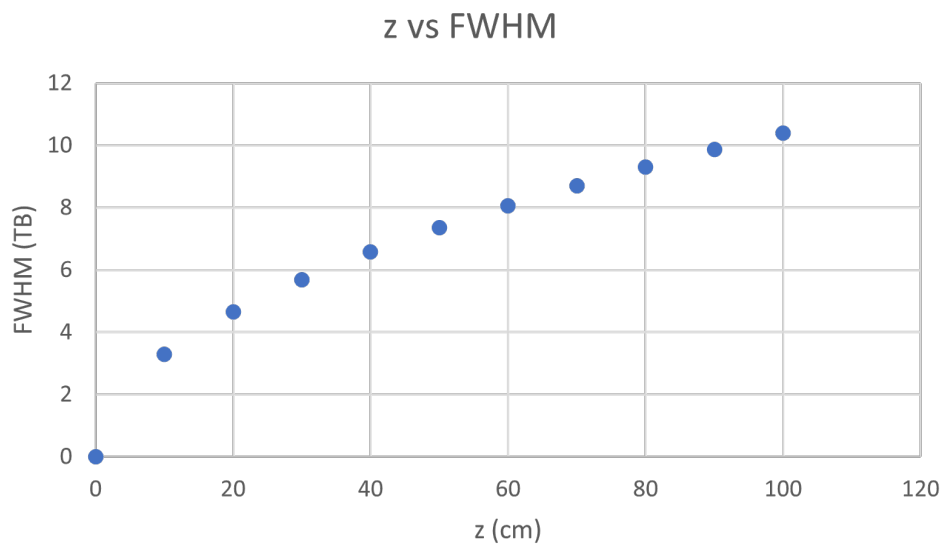
Figure 4.16 Plotted is the expected spread of the charge (FWHM) in time at the pad plane due to longitudinal diffusion in the gas as a function of where the charge was produced in the detector.

The deconvolution PSA method (Deconv PSA) allows us to describe the charge of the fission

Deconv PSA parameter	Value
Filter cutoff frequency	75
Filter order	6
Charge threshold	10

Table 4.3 Parameters used in the deconvolution PSA for the fission fragments.

TBAvg PSA parameter	Value
Charge threshold	45 (ADC units)
n	5 TBs

Table 4.4 Parameters used in the TBAvg PSA for the beam.

fragments well. This is demonstrated in Fig. 4.17 which shows the reconstructed current on two pads, one at the pad plane and one 0.5 m away from the pad plane. In both cases there is good agreement between the Gaussian fit and the current. This method is not well suited to analyzing the beam region. In its current implementation, we generate one hit per pad with the Deconv PSA. This is insufficient to describe the path of the beam through he TPC where it may only pass over a handful of pads. So the Deconv PSA meets most of our goals: it provides good charge and position information for the FF, but does not produce good position information for the beam region.

To solve this problem, we use a second PSA method in the beam region. Because our primary focus in this region is determining the position of the hits, we only care if charge is being collected on the pads and at what time, not how much charge is being collected. We call the PSA method used in the beam region the Time Bucket Average PSA (TBAvg PSA) method.

The TBAvg method is conceptually quite simple. We split the trace up into $512/n$ slices. For each slice we say the charge, q, is the average ADC value for n time buckets in the slice. If the charge is above some threshold, then we save a hit. The x/y position of the hit is set by the center of the pad and the z position of the hit is set to the midpoint of the slice. That is, if the hit was created by averaging the time buckets from 100 to 102 (inclusive), the z location would correspond to time bucket 101. The parameters for this PSA method used in the analysis of the fission experiment are given in Table 4.4.

The determination of which PSA method to apply to a pad in a given event is determined by the location of the pad in the pad plane. If the distance between the center of the pad to the center
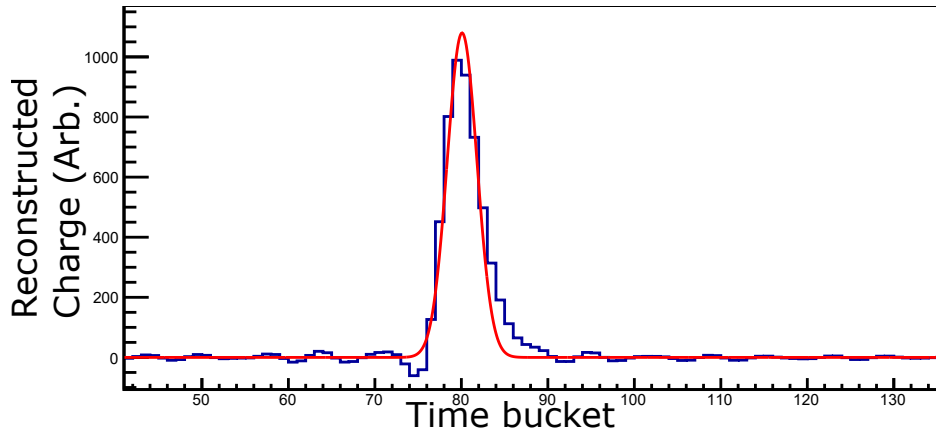
(a) Fission fragment hitting the pad plane.
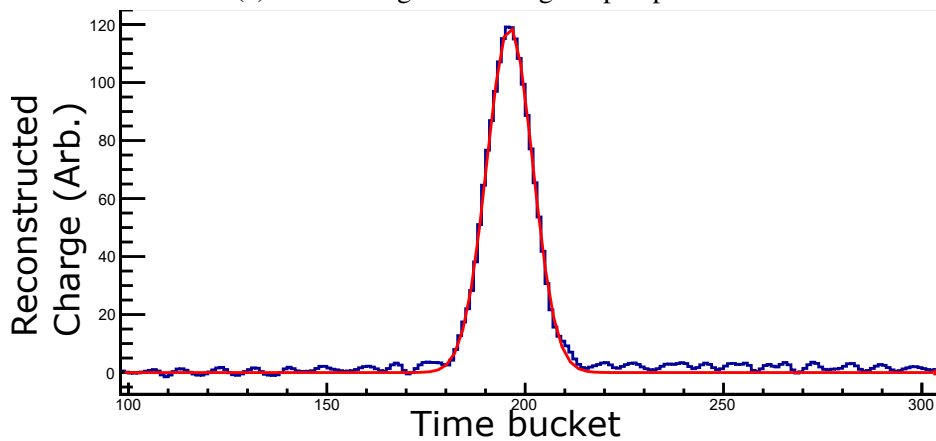
(b) Fission fragment 0.5 m from the pad plane.

Figure 4.17 Gaussian fit to the current collected on two pads. One where the fission fragment is hitting the pad plane (a) and one where the fission fragment is about 0.5 m from the pad plane (b).

of the pad plane is less than 20 mm, then we use the TBAvg PSA method. Otherwise we use the Deconv PSA method.

The use of two different PSA methods has an important implications to keep in mind for the rest of the analysis. The charge of the hits in the two regions are not on the same scale. That is, there is a different constant of proportionality between the recorded charge and the physical value of the charge deposited in the two regions of the TPC. As discussed in the next section, this means care must be taken when performing fits to tracks across this boundary.

In principle, one could try to correct this difference in scale between these two PSA methods. We choose not to do that because of the complexity of the task. The TBAvg method operates on the trace while the Deconv method operates on the reconstructed charge so the proportionality

between them would be position and angle dependent. This boundary region is also around the boundary of the lower gain region. Even if the charge was put on the same scale, we have poor position measurements in this region because of the effects of space charge. It was determined that the effort involved in getting the charge on the same scale was not worth the minimal benefit.

4.5.3 Space charge correction

The process for correcting hits for space charge is described in Sec. 3.11. That method describes the process of estimating a solution to the Langavin equation (Eqn. 3.22) for a axially symmetric space charge field. Here, we will describe the details of the model used, including the closed form solutions to our modeled space charge.

To estimate the distortion to the electric field, we treat the space charge as a long thin wire, centered at (0,0). The electric field is given by:

$$\vec{E} = \frac{\lambda z}{2\pi\epsilon_0 \rho L} \hat{\rho} \tag{4.1}$$

where λ is the magnitude of the line charge at the window, z is the distance from the pad plane, and L is the length of the drift volume. The field strength scales with z because the positive ions are slowly drifting towards the TPC entrance window so that more charge is built up farther from the pad plane. The effect of this field is to pull the drifting e^- inwards, thus distorting the recorded tracks.

Conveniently, there is a closed form solution to the Langavin equation for this model. It is given by:

$$\rho_f^2 = \rho_i^2 + \frac{\lambda}{\pi\epsilon_0} \frac{z}{E_z} \frac{z}{2L} \tag{4.2}$$

where ρ_f is the distance from space charge line after correction, and ρ_i is the distance from the space charge line before correction.

In reality, the beam is not centered at (0,0), but instead there is some offset and the beam is traveling at a shallow angle. This can be seen in Fig. 4.18 which plots the beam profile at the window and at the pad plane. From these plots, we estimate the average position of the beam a

99

distance z from the pad plane to be:

$$\vec{x}_{beam} = \frac{\vec{x}_{pp} - \vec{x}_{win}}{1000} z \tag{4.3}$$

$$\vec{x}_{pp} = 0\hat{x} - 6\hat{y} + 0\hat{z} \; mm \tag{4.4}$$

$$\vec{x}_{win} = 10\hat{x} - 0\hat{y} + 1000\hat{z} \; mm \tag{4.5}$$

where $\vec{x}_{pp}$ and $\vec{x}_{win}$ are the average position of the beam at the pad plane and window, respectively, and z is the distance from the pad plane in mm.

To account for the changing beam direction before correcting for the space charge we undergo a change of coordinates, re-centering the origin on $\vec{x}_{beam}$ on a hit-by-hit basis. The final thing we must do is determine the remaining free parameter (λ) and verify the space charge correction works as intended.

The primary tool we will use for both these tasks is a comparison between two independent methods of determining the vertex. The first method uses the sample consensus method described in Sec. 3.5.1 to fit a "Y" pattern to the hits in an event. We will call this method the "Y-fit" method. The vertex extracted using this method depends strongly on the effects of space charge. The second method involves examining the charge collected on the pads in the beam region over time. When a fission occurs, the magnitude of the energy loss in the beam region should drop (energy loss scales as Z^2). We will call this method the "ADC sum" method. By identifying where in time that drop occurs, we can determine the z location of the vertex. This second method only works for a small subset of the data where the ADC sum is clean enough to identify the drop corresponding to the vertex. In addition, these events usually need to be hand selected to make sure the the location of the vertex in the ADC sum is properly determined and we are not picking up a sudden change in the dE/dx arising from pileup or another effect. Fig. 4.19 illustrates these two methods, where the vertex from the ADC sum method is marked in blue, and the vertex from the Y-fit method is marked in red.

By varying the magnitude of the space charge correction (λ), we should be able to empirically determine the correct magnitude of the correction. When the magnitude is properly set, we would
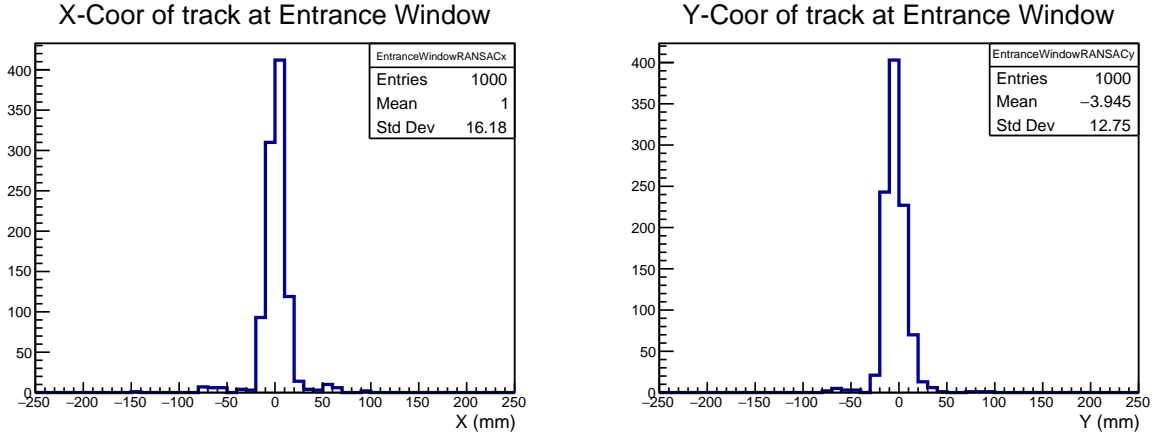
(a) Beam Position at Window.
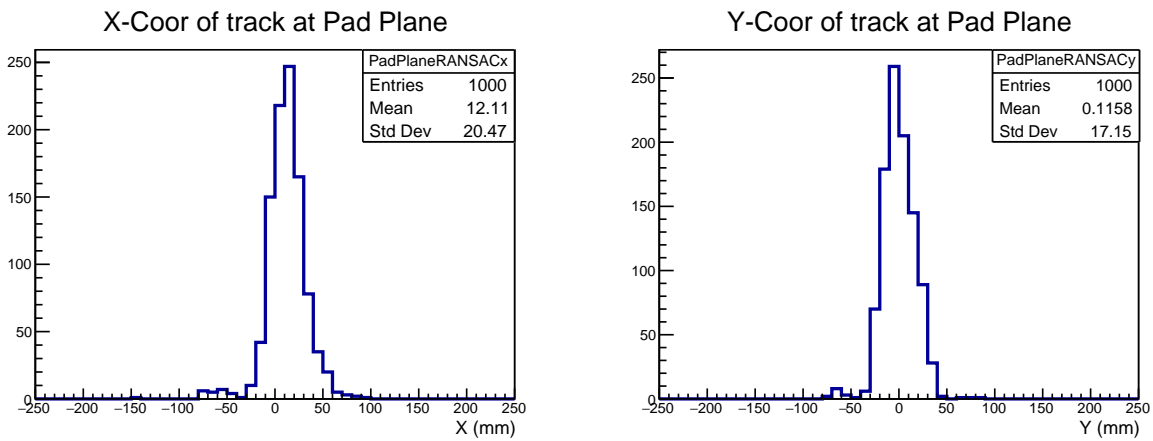
(b) Beam Position at Pad Plane.

Figure 4.18 Measured profile of the beam in the AT-TPC at the window (top row) and pad plane (bottom row).

expect the two methods to converge on a single vertex location. This can be seen in Fig. 4.20 where the left panel shows the correlation between the two methods with no space charge correction applied, and the right panel shows the correlation with a properly selected λ.

The final step in characterizing the space charge correction is determining how the magnitude of the correction depends on the beam rate. Since the the number of positive ions produced scales linearly with the beam rate, we would expect λ to also have a linear dependence on the beam rate. To determine this scaling, we manually tune λ for a series of runs with differing beam rates until we see a good correlation between the two vertex reconstruction methods, like that seen in Fig. 4.20b. Fig. 4.21 shows the correlation between λ and the beam rate for those runs. When applying the
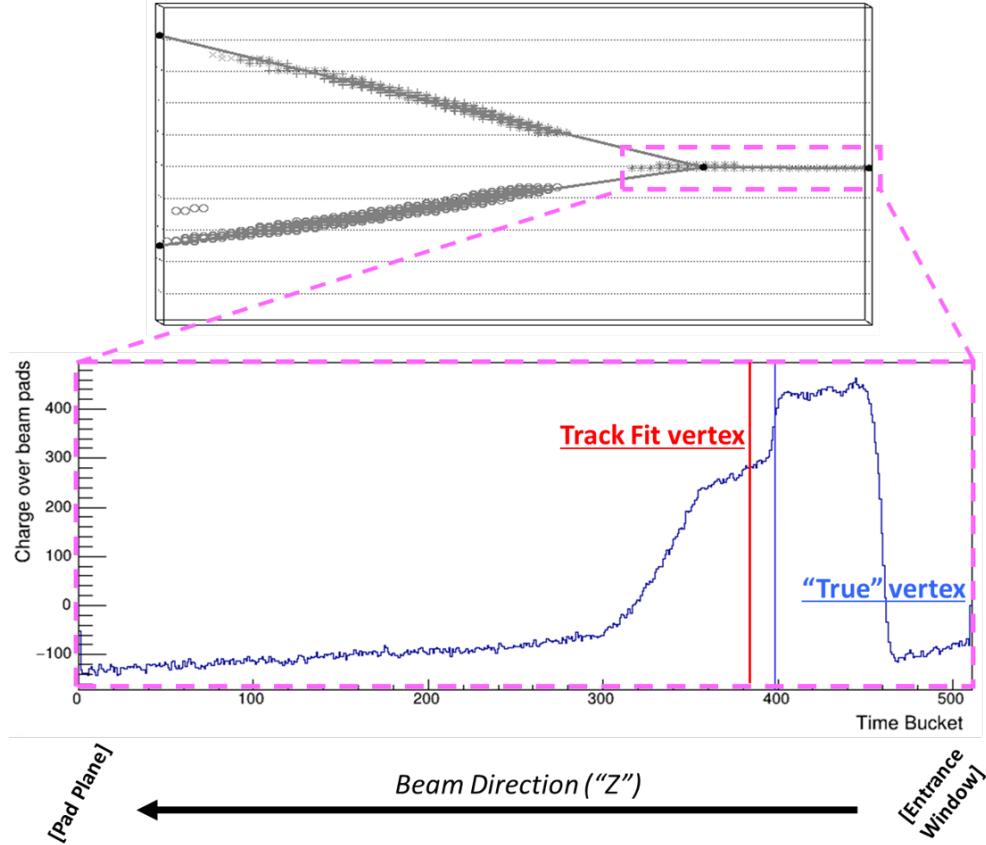
Figure 4.19 The upper panel shows the fission event in space, with the Y-fit marked. The vertex is the point of intersection between the three lines. The timebucket corresponding the the z location of the vertex is marked by the red vertical line in the lower panel. The lower panel shows the sum of the traces for all the pads in the beam region. The drop associated with the vertex is marked by the blue vertical line.

space charge correction, we set the magnitude of λ based on the average beam rate for the run:

$$\lambda = 3 \times 10^{-12} * R + 4 \times 10^{-9} \tag{4.6}$$

where R is the average beam rate for the run in pps, and λ has units C/m.

4.5.4 Identifying fission tracks

We identify tracks in the TPC using the sample consensus (SAC) method described in Sec. 3.5.1. As discussed previously, there are three main components that go into the construction of a SAC analysis: First, is the pattern describing the shape we are looking for in the data, including the method of fitting the data to the pattern, see Sec. 4.5.4.1. Second, is the method for sampling hits in the event to create trial patterns, see Sec. 4.5.4.2. Third, is the method of evaluating how well a
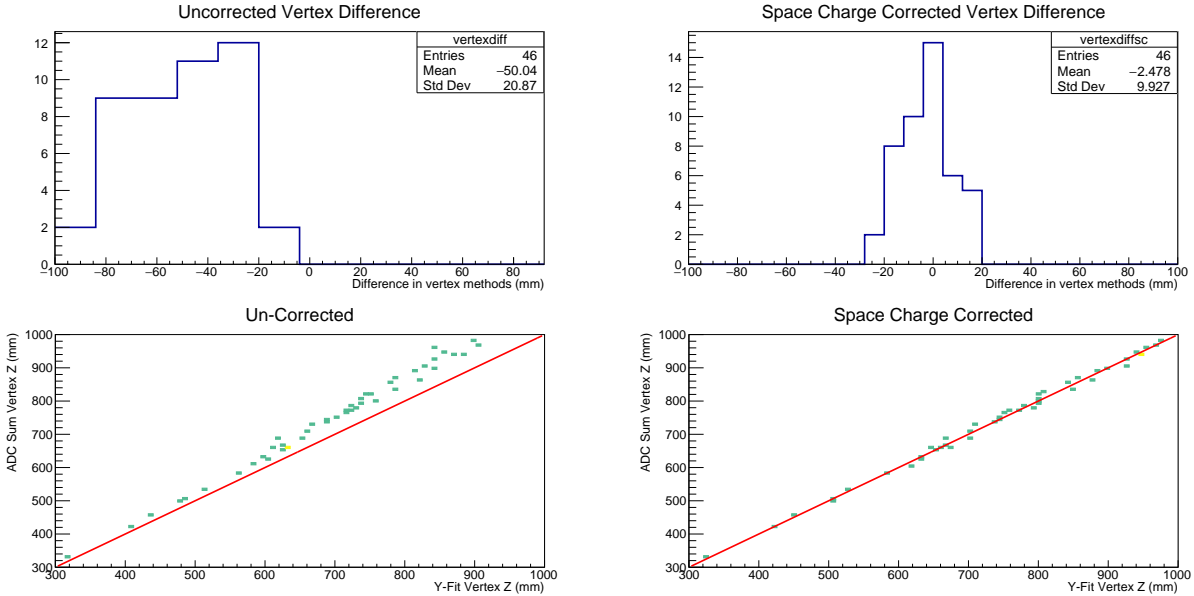
(a) Before data correction.   (b) After data correction.

Figure 4.20 Difference in vertex determination between the Y-fit and ADC sum methods before and after correction of the data.
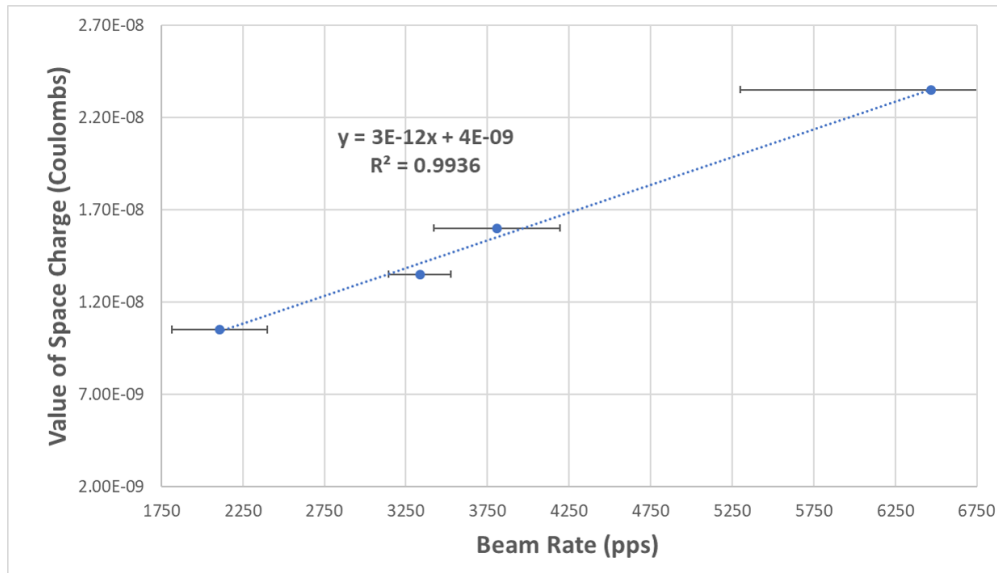
Figure 4.21 Trend between the beam rate and extracted value of λ that provides agreement between the Y-fit and ADC sum methods of vertex determination. The error in the beam rate is the 1 sigma error bar arising from the variance of the beam rate over the run.

trial pattern describes the data, see Sec. 4.5.4.3. All of the parameters used in the SAC calculation and their values for the fission experiment can be seen in Table 4.5. We only accept patterns that are consistent with at least 150 hits. We estimate this will capture more than 99% of fission events.

103

SAC Parameter	Description	Value
Pattern	Shape we are identifying in the hit cloud	Y-Pattern (4.5.4.1)
Sampling method	Method used to randomly sample hits in the hit cloud to generate trial pattern.	Y-sampling (4.5.4.2)
Estimator	Method of ranking generated trial patterns by "goodness."	Y-RANSAC (4.5.4.3)
Distance threshold	Maximum distance a point can be from the trial pattern and be considered consistent with the pattern.	20 mm
n_{min}	Minimum number of points that have to be consistent with the trial pattern for the trial pattern to be valid.	150
N	Number of trial patterns to generate from the hit cloud	500

Table 4.5 Parameters used in the SAC calculation for identifying fission tracks in events.

The average number of hits consistent with the pattern is 356, and the standard deviation of the distribution of hits consistent with the pattern is 88.5.

4.5.4.1 Y-Pattern

The Y-pattern is defined by four points. One point is the vertex, and the other three points lie along the three rays originating at the vertex. In determining the best trial pattern, the points defining the pattern must be the location of hits in the AT-TPC from the PSA methods. There is no guarantee that we will have a hit in the data that corresponds to the vertex location, or hits that would lie on the best description of the three rays. In fact, the effects of space charge mean we do not have good position information from the beam region near the window.

To account for this we must fit the y-pattern to the data allowing the vertex location and the directions of the rays to vary away from the limited set of options that arise from creating patterns based on the recorded hits in an event. After we have selected the best trial pattern, we assign each hit in the event consistent with the pattern to the track it is closest to: FF1, FF2, or Beam corresponding to the two fission fragments or the beam, respectively. From the collection of hits associated with the fission fragments we remove those in the beam region. This is for two important reasons. First the PSA method used to generate the hits inside the beam region is different than the PSA methods used to generate the hits outside the beam region. As a result, the charge associated

with the hits has a different scale in the two regions of the TPC. Second, the hits in the beam region are not corrected for the effects of space charge and including the uncorrected hits would distort the fit.

For each track we define the following objective function:

$$\chi^2_{FF1} = \frac{\sum_i^{hits} q_i d_i^2}{\sum_i^{hits} q_i} \tag{4.7}$$

where q_i is the charge associated with a hit and d_i is the distance between the hit and the pattern. The objective functions for the other tracks are similarly defined. What we aim to minimize is then:

$$\chi^2 = \chi^2_{FF1} + \chi^2_{FF2}. \tag{4.8}$$

Because we primarily care about properly reconstructing the vertex location and direction of the fission fragments, we do not incorporate information from the beam region in the minimization.

The pattern is defined by 12 parameters. Three for the position of the vertex (x,y,z) and nine for the directions of the three rays ($\hat{x}, \hat{y}, \hat{z}$ for each). Since we are not fitting the direction of the beam (it is not included in our objective function) we fix the direction of the beam ray. There are then seven free parameters to fit, the vertex location and direction (polar and azimuthal angles) of the two fission fragments. The fit is performed using the CERN ROOT Fitter interface using the Minuit2 minimizer. The fit pattern is then saved for future analysis described in Sec. 4.6.

4.5.4.2 Sampling Method

In this analysis, we know something about the expected shape and location of the fission tracks. The vertex must lie along the beam axis and the ray associated with the beam must also lie along the beam axis. We exploit this fact by randomly sampling two hits in the beam region, defined as a cylinder with a radius of 4 cm centered in the active volume. The sampled hit closest to the pad plane is taken as the vertex of the trial pattern, and the second sampled hit is used to define the direction of the beam in the trial pattern.

Two hits are then randomly sampled in the non-beam region of the TPC. We start by attempting to sample two hits closer to the pad plane than the sampled vertex. If this fails, then we just sample two hits outside the beam region. If even that fails then we just sample two more points across the

entire TPC volume. The two newly sampled hits are then used to define the direction of the two fission fragments in the trial pattern. Of course, even more complicated sampling methods can be developed, but the speed of the SAC calculation relies on the random sampling being fast. So the additional computational time spent in more complicated sampling methods is a net loss in speed without improving the results. After the trial pattern is defined, we then estimate how well the data matches the trial pattern.

4.5.4.3 Modified Y RANSAC Estimator

We use a modified version of the traditional RANSAC estimator to define how well the trial patterns match the data. In the traditional RANSAC estimator, we try to maximize the total number of inliers, or points in the event that are within some distance threshold of the pattern. In our estimator we try to maximize the number of inliers associated with the two fission fragments. This change is made to help deal with complications from pile-up. When there are multiple beams in the AT-TPC at once, you can get an anomalously large number of hits along the beam axis. Using a traditional RANSAC estimator can cause the "best" trial pattern to place the vertex near the pad plane, capturing all the hits in the beam region but missing the fission fragments entirely. This is demonstrated in Fig. 4.22 where the pattern found using our estimator is show in Fig. 4.22b, and the same event identified using the traditional RANSAC estimator is show in Fig. 4.22a. The traditional RANSAC misses the FF, while ours successfully identifies the tracks in the event.

4.6 Monte-Carlo fitting of fission events

The large number of detector effects present in the data, such as space charge corrections and missing or corrupted data from parts of the pad plane, mean that it is very difficult to obtain the complete energy loss curve of the fission fragments from the data. Instead, a simpler approach is to simulate the detector response to trial fission events, including all of the detector effects. A direct comparison can then be made between the experimental data in the pads where the data is uncorrupted and the simulated data in those same pads. A general description of this Monte-Carlo fitting technique is given in Sec. 3.7.2. Here we will detail the method implemented for simulating fission events to extract both the charge distributions for different fissioning systems, as well as the

106
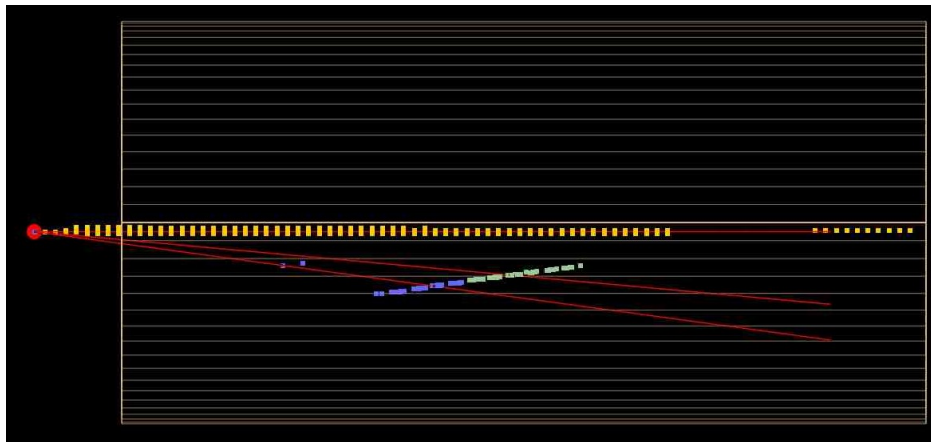
(a) RANSAC Estimator.
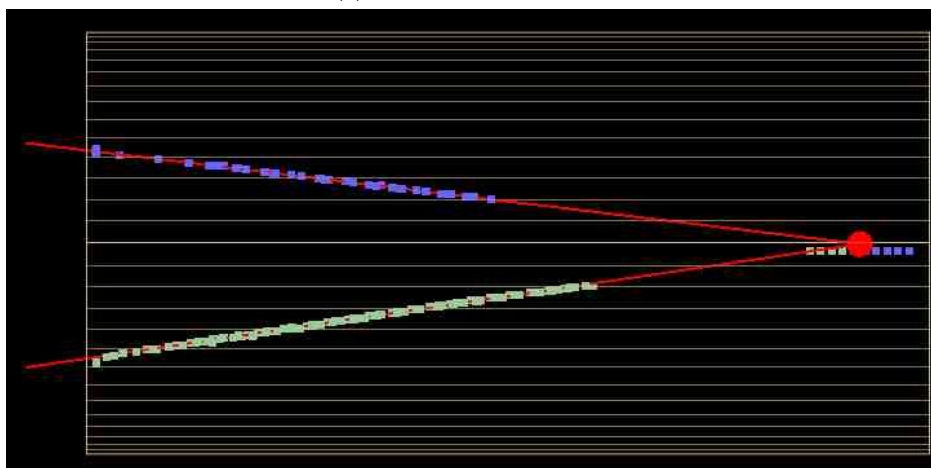
(b) Y-RANSAC Estimator.

Figure 4.22 The best trial pattern for the same event using the traditional RANSAC estimator (a) and the modified Y RANSAC estimator (b). In both cases the beam is entering the TPC from the right, the hits are colored by the track, and the red lines mark the result of the fit of the pattern to the data.

beam energy and by extension the excitation energy. We initially simulate 100 trial events, before using the best of those 100 trial events to recenter the parameter distributions we are sampling. A 100 more trial event are sampled and we take the best of those to extract the energy of the beam and the charge of the fission fragments.

This method requires four primary pieces of information: First, we need to define the simulation method to calculate the magnitude and position of the energy loss of the fission fragments. This includes both the energy loss models for all of the fission fragments as well as any models describing the effects of space charge on the drifting electrons. While the effects of space charge physically

occur as the electrons drift from their point of creation at an ionization site to the pad plane, we account for it in the simulation by shifting the ionization site. We will call the physical ionization site $\vec{x}_0$, and where the electron arrives at the pad plane after drifting under the influence of the total electric field (drift field and field from space charge) $\vec{x}_{PP}$. In the simulation, we shift the ionization site from $\vec{x}_0$ to $\vec{x}_{SC}$ such that an electron drifting from $\vec{x}_{SC}$ under the influence of an electric field without the space charge component arrives at the pad plane at $\vec{x}_{PP}$. This is done to fully decouple the space charge correction from the simulation of the detector response. This is discussed in Sec. 4.6.1.

The second piece of information is the selection of a method for digitizing the simulated data (i.e. simulating the detector response). This involves calculating and drifting the charge produced in the active volume, assigning that charge to specific pads, and optionally calculating the response of the electronics. This is the same as the clusterize and pulse tasks discussed in Sec 3.3.2, and the choices for this experiment are detailed in Sec 4.6.2.

Third, we need to analyze the simulated data in the same way as the experimental data up to the point where we can do a direct comparison. For us, this just involves running a pulse shape analysis method to construct hits in the detector volume, see Sec. 4.6.3.

Fourth, we need a method of generating trial fission events based on the actual experimental event we are trying to match. In our case, our experimental data is a fission event with all of the corrections described in previous sections fitted with a Y-pattern determined by a SAC calculation. The details are discussed in Sec. 4.6.4.

4.6.1 Simulation

Because we do not need the full machinery of the ROOT VMC simulation method discussed in Sec. 3.3.1.1 we use the simpler simulation method laid out in Sec. 3.3.1.2. This method also has the benefit of giving us much tighter control over the models used in the simulation. It was also parallelized for this experiment to speed up the time to simulate the trial events. The energy loss models in use, and how they are used to calculate energy losses over the distance steps in the simulation are discussed below in Sec. 4.6.1.1. The space charge model in use is detailed in Sec.

4.6.1.2.

4.6.1.1 Energy loss models

The energy loss models used are tabulated values of the stopping power, dE/dx. We used tables from both SRIM [24], as well as tables exported from LISE [46] to access the models it contains. When we discuss using LISE energy loss models, we are referring to the ATIMA-LS corrected energy loss model [73] from LISE unless otherwise stated. For the beam, these two models make very different predictions for the energy loss of the beam in the material upstream of the AT-TPC as seen in Fig. 4.1. The difference in the energy loss models has a much smaller impact on the reconstructed fission events, explored in Sec. 4.8. We will use the SRIM energy loss models unless otherwise stated as those provide better (although not good) agreement with the measured energy loss of the beam.

Regardless of the source of the tabulated model, we extract energy losses through a material the same way. The tables are interpolated using a C^2 cubic spline (that is the cubics, as well as their first and second derivatives are continuous). The integral of the cubic splines can be computed exactly, and cheaply, using Simpson's Rule [74] which is exact for cubic functions. The integrated tables can be directly used to calculate the distance traveled, d, to drop from some initial energy E_i to a final energy E_f. To invert that process and calculate E_f after traveling a known distance d we use Newton's method of root finding, iterating E_f until we converge on the desired distance d.

4.6.1.2 Space charge model

The space charge model used to distort the simulated data is the same as the model used to correct the experimental hits described in Sec. 4.5.3 where the distorted field is modeled by:

$$\vec{E} = +\frac{\lambda}{2\pi\epsilon_0 \rho}\frac{z}{L}\hat{\rho} + E_z\hat{z} \tag{4.9}$$

where L is the length of the detector, E_z is the nominal drift field, λ is the magnitude of the line of space charge at the window, and z is the distance from the pad plane.

Solving the Langavin equation under the assumption that we are at the steady state velocity and lack a magnetic field (Eqn. 3.22), the final radius the electron arrives at the pad plane, ρ_f, having

been produced at ρ_i is given by:

$$\rho_f^2 = \rho_i^2 - \frac{\lambda}{\pi\epsilon_0} \frac{z}{E_z} \frac{z}{2L} \qquad (4.10)$$

The effect of applying this distortion is seen in Fig. 4.23 where the simulated hits from a trial event (in red) are overlaid on the experimental hits (in purple). There is good agreement between the two for most events. The impact this space charge correction has on our ability to reconstruct events is discussed further in Sec. 4.7.2.
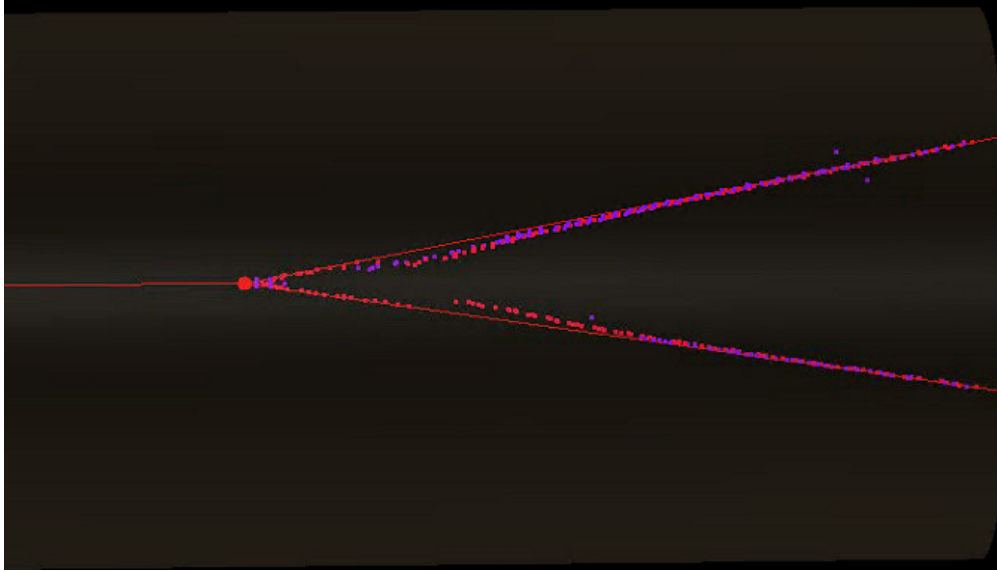
Figure 4.23 Experimental (purple) and simulated (red) hits for a fission event. The simulated hits have had the space charge distortion applied. The space charge correction is only applied if the distance from the line charge to the hit is greater than 2 cm, which is seen in the discontinuity in the bottom track.

4.6.2 Digitization

After calculating the energy loss of the FF in the active volume, and correcting for the space charge, we now need to drift the ionized electrons to the pad plane and assign the charge to particular pads. For this we use the same methods described in Sec. 3.3.2.

There are two differences between what is described in Sec. 3.3.2 and what we do for the trial events in the MC fitting method. Both changes reflect the fact that speed in simulating the trial events is very important. First, when integrating the transverse diffusion to assign electrons to pads, we reduce the number of points sampled to 100 from the default of 500. This speeds up the

simulation by $\sim 50\%$. This has little effect on the integrity of the simulation and the distribution of charge across the pads is consistent between the two cases.

Second, we do not do the numeric convolution of the response function with the collected charge. As discussed below in Sec. 4.6.5 what we use to evaluate how well the simulated and experimental events match is the charge collected on the pads, not the traces. From the simulation we have that information directly. From the experimental data we back it out using the deconvolution method described in Sec. 4.5.2. Removing the convolution from the simulation speeds it up by more than a factor of 3.

4.6.3 Reconstruction

The final step in the simulation of a trial event is doing whatever additional analysis is required to do the comparison between the simulated and experimental events. In out case, that is just extracting hits from the charge collected on the pads. We use the same pulse shape analysis method discussed in Sec. 3.4.2.2; however, we do not need to do the initial deconvolution. Instead, we can skip directly to fitting the charge by a Gaussian.

4.6.4 Defining trial events

Our goal is to simulate a collection of trial events and determine which trial event looks the most similar to the experimentally measured fission event. Through the analysis discussed in Sec. 4.5 we can accurately measure the direction of the fission fragments, and the vertex location in the TPC. For this analysis we consider only the fission events with the largest folding angles, which correspond to the fission events where, in the center of mass (CoM) frame, the decay of the CN happens perpendicular to the beam direction. The selection of these events is discussed in Sec. 4.7.1.

With this assumption, and our measurements of the vertex location and FF directions there are only two additional pieces of information we need to fully define a trial fission event. First is the species (A and Z) of the two fission fragments. This is determined by a single parameter, the charge of one of the fission fragments. We sample a t-distribution initially centered at $\frac{Z_{CN}}{2}$ and with a standard deviation of 3 (the long tails on the t-distribution mean these do not need to be

111

particularly well tuned). This sampled value is rounded to the nearest integer which we take as Z_1, or the charge of the first fission fragment. The charge of the second fission fragment is then given by $Z_2 = Z_{CN} - Z_1$. We also assume that the mass is split the same as the charge. That is the masses of the two FF are given by:

$$A_1 = \frac{Z_1}{Z_{CN}} A_{CN} \tag{4.11}$$

$$A_2 = A_{CN} - A_1 \tag{4.12}$$

This assumption is not fully accurate, but the deviation from a more accurate description of reality where the mass is assigned by minimizing the binding energy of the FF does not lead to deviations from this simple model that would impact the analysis. This is evidenced in Fig. 4.24 where even at very asymmetric splits, the difference in mass minimizing the binding energy (given by the semi-empirical mass formula) is less than 3 mass units.
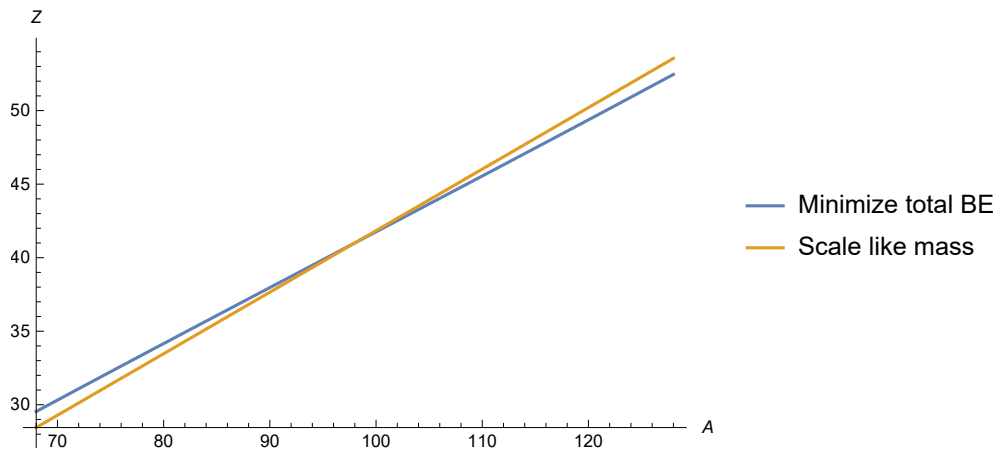
Figure 4.24 Mass and charge for fission fragments under two models. One as the mass split like the charge (orange), the other has the mass split to minimize the binding energy (blue).

There is another assumption hiding in this discussion. That is that the fission decay is a two-body decay where the CN decays into two FF which, only after the decay, may then emit additional particles (mostly n and γ) to de-excite. We also assume those decays do not substantially change the momentum of the fission fragments in the lab frame, and the change in mass from those possible decays does not change the energy loss of the FF as it passes through the detector; a reasonable assumption as the energy loss does not have a very strong dependence on the mass.

At this point we have the following description of a trial event: A compound nucleus with mass A_{CN} and charge Z_{CN} decays into two fission fragments (Z_1, A_1) and (Z_2, A_2) where the decay axis is perpendicular to the beam axis. The final piece of information we require is determining the momentum of the FFs in the CoM frame. We can use Viola systematics [75] to estimate this final piece of information.

Viola systematics describe the most probable total kinetic energy of the FFs after a fission decay in the CoM frame, $\langle E_k \rangle$. $\langle E_k \rangle$ has a linear dependence on the Coulomb parameter $Z^2/A^{1/3}$ for the fissioning nucleus and can be interpreted as the kinetic energy resulting from the Coulomb repulsion of two prolate spheroids (the FFs). The model provides the following relation:

$$\langle E_k \rangle = (0.1189 \pm 0.0011)Z^2/A^{1/3} + (7.3 \pm 1.5) MeV \tag{4.13}$$

which for ^{204}At corresponds to a kinetic energy release of $\langle E_k \rangle = 153.2 \pm 2.9$ MeV. This model appears to hold true across a large portion of the chart of nuclei, and does not appear to have a strong dependence on the excitation energy of the fissioning nucleus as discussed in [75].

By definition, in the CoM frame the total momentum is zero, so $\vec{p}_1 = -\vec{p}_2$ where $\vec{p}_1$ and $\vec{p}_2$ are the momentum of the first and second fission fragments, respectively. The two fission fragments are released with kinetic energies KE_1 and KE_2. Treating the decay relativistically (strictly speaking this could be done non-relativistically but doing it relativistically simplifies the software development), our goal is to solve the following set of equations for the fissioning system:

$$\gamma_1 m_1 v_1 = \gamma_2 m_2 v_2 \tag{4.14}$$

$$\langle E_k \rangle = m_1(\gamma_1 - 1) + m_2(\gamma_2 - 1) \tag{4.15}$$

where γ has the typical definition $\gamma = (1 - v^2)^{-1/2}$, m is the rest mass, $\vec{v}$ is the velocity. We use units where we set the speed of light $c = 1$.

Solving these equations gives the Lorentz factors, γ_1 and γ_2 of the two FF in the CoM frame:

$$\begin{aligned} \gamma_1 &= \frac{\langle E_k \rangle^2 + 2(m_1 + m_2)(\langle E_k \rangle + m_1)}{2m_1(\langle E_k \rangle + m_1 + m_2)} \\ \gamma_2 &= \frac{\langle E_k \rangle^2 + 2(m_1 + m_2)(\langle E_k \rangle + m_2)}{2m_2(\langle E_k \rangle + m_1 + m_2)} \end{aligned} \tag{4.16}$$

The velocities are then given by $v = \sqrt{1 - 1/\gamma^2}$. With these velocities, the system in the CoM frame is fully described.

Moving to the lab frame, there are two frames it is useful to think about. First, is the frame we will designate the "Lab" frame. This is the frame of the physical detector we have been using up to this point where the z-axis is perpendicular to the pad plane. The second frame we will call the "Lab′" frame. This is a rotation of the Lab frame where the z-axis points along the trajectory of the beam particle at the point of interaction.

We will start by considering the boost from the CoM frame to the Lab′ frame. In this case, the boost happens purely along the z-axis, so the transverse velocity components of the FF remain unchanged by the boost, aside from a slight adjust of the velocity due to time dilation. The velocities on the lab' frame are given by:

$$v'_T = v_T \sqrt{1 - v_B^2} \tag{4.17}$$

$$v'_z = v_B \tag{4.18}$$

where v'_T and v'_z are the transverse and z velocities in the Lab′ frame, v_T is the transverse velocity in the CoM frame given by Eqn. 4.16, and v_B is the beam velocity (i.e. the relative speed between the CoM and Lab′ frames).

From the experimentally measured folding angle, θ, between the FFs we can calculate the total momentum of the FF in the Lab′ frame by examining the velocities. Fig. 4.25 shows the velocity vectors of the fission fragments in the CoM and Lab′ frames where $v_{T,1/2}$ are given by Eqn. 4.16 and $v'_{T,1/2}$ are given by Eqn. 4.18. The angle between the beam and velocity of the fission fragments, $\theta_{1/2}$ is then given by:

$$\theta_1 = \tan^{-1}\left(\frac{v'_{T,1}}{v_b}\right) \tag{4.19}$$

with a similar expression for θ_2. The observable, the folding angle between the fission fragments,
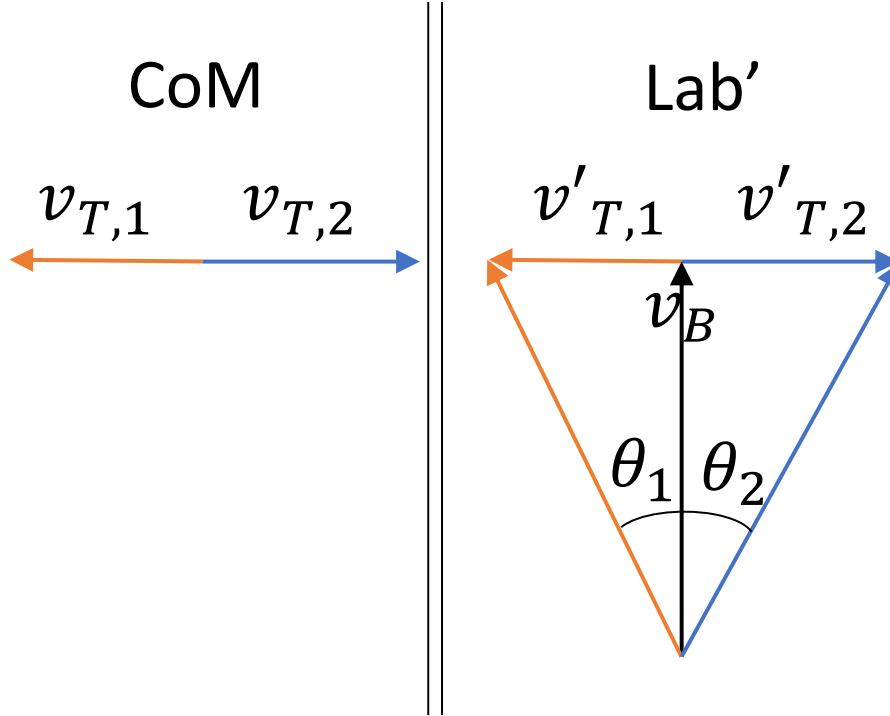
Figure 4.25 Velocity of the fission fragments in the CoM and Lab' frames. Not to scale.

θ is given by:

$$\theta = \theta_1 + \theta_2$$

$$\theta = \tan^{-1}\left(\frac{v'_{T,1}}{v_b}\right) + \tan^{-1}\left(\frac{v'_{T,2}}{v_b}\right) \tag{4.20}$$

$$\theta = \tan^{-1}\left(v_B \frac{v'_{T,1} + v'_{T,2}}{v_B^2 - v'_{T,1}v'_{T,2}}\right)$$

Inverting this expression and solving for v_B gives:

$$v_B = \frac{v'_{T,1} + v'_{T,2} \pm \sqrt{v'^2_{T,1} + v'^2_{T,2} + 2v'_{T,1}v'_{T,2}(1 + 2\tan^2\theta)}}{2\tan\theta} \tag{4.21}$$

The direction of the momentum and velocity are the same, so we can now calculate the total magnitude of the momentum of the FF in the Lab' frame:

$$p_1 = \frac{p_{T,1}}{\sin\theta_1} \tag{4.22}$$

where $p_{T,1}$ is the the transverse momentum in the Lab' frame, and θ_1 is given by Eqn. 4.19. There is a similar expression for the momentum of the second fission fragment.

115

The magnitude of the momentum, which is the same in the Lab and Lab' frames, combined with the experimentally determined direction of the FFs allow us to fully define the event in the lab frame:

$$\vec{p}_1 = p_1 \hat{p}_{exp,1} \tag{4.23}$$

$$E_1 = \sqrt{m_1^2 + p_1^2} \tag{4.24}$$

where $\hat{p}_{exp,1}$ is the direction of the FF from the Y-pattern fit of the experimental event. There is a similar expression for the second FF.

Conservation of 4-momentum allows us to easily reconstruct the beam's direction and kinetic energy:

$$\hat{p}_B = \frac{\vec{p}_1 + \vec{p}_2}{||\vec{p}_1 + \vec{p}_2||} \tag{4.25}$$

$$KE_B = E_B - m_B \tag{4.26}$$

where $\hat{p}_B$ is the direction of the beam, KE_B is the kinetic energy of the beam and m_B is the rest mass of the beam.

This process of sampling the physical parameters of the trial event, and using those sampled values to calculate the momentum of the FF in the lab frame is repeated a number of times. The resulting 4-vectors (from Eqn. 4.23) along with the initial position (the reaction vertex from the Y-pattern), and the particle ID are passed to the simulation discussed above to acquire the charge collected on each pad for each of the trial events.

4.6.5 Evaluating trial events

We evaluate how well the trial events compare to the experimental event by examining the charge collected on the pad plane as a function of time. We start by constructing the experimental dQ/dTB curves where dQ/dTB is the measured charge collected on the pad plane per time bucket. These curves serve as a proxy for the dE/dx curves of the fission fragments. To construct the curves, we loop through all of the experimental hits associated with that fragment. From these hits, we generate a list of good pads associated with the fragment. A pad is considered good if it is outside

116

CoBo ID	AsAd ID	AGET ID	Channel ID
2	3	all	all
0	1	1	6-7
0	1	1	9-10
0	1	1	12-13
0	1	1	39-41
0	1	1	43-44
0	1	1	46

Table 4.6 List of bad channels removed from the charge analysis.

the low gain region of the TPC, it is not one of the malfunctioning electronic channels, the pad was not saturated in the event, and it is one of the small pads in the inner region of the TPC. Table 4.6 lists all of the electronics channels we exclude from the charge analysis. For each pad that passes all these checks, we add the Gaussian fit of the reconstructed current to our experimental measure of dQ/dTB.

A similar process is repeated for the simulated fission fragments where we sum the Gaussian fits of the simulated current for the good pads identified in the experimental event. That is, the data in the simulated and experimental curves arise from the same set of pads. This has a consequence that there can be points in the data and the simulation where the charge is not completely corrected due to the pads that are not working and have no signal.

We then trim the dQ/dTB plots for both fission fragments by dropping the time buckets where the experimental dQ/dTB has no charge. An example of the resulting charge curves for the two fission fragments can be seen in Fig. 4.26 where the blue curves are the experimental dQ/dTB curves and the red curves is the simulated dQ/dTB from the trial event that best matches the experimental data.

Because of the pads we remove there are often gaps or unusual structure in the experimental dQ/dTB curves. This can be seen clearly in Fig. 4.26a where the curve dips suddenly around TB 130 before rising again around TB 80. Because we only add charge to the simulated curve if there is data in the corresponding pad in the experimental event, our simulation still matches the data. Fig 4.27 shows the simulated dQ/dTB curves for the same event shown in Fig. 4.26, but keeping all of the pads in the simulation. Here you can see the complete curve does not contain the dip
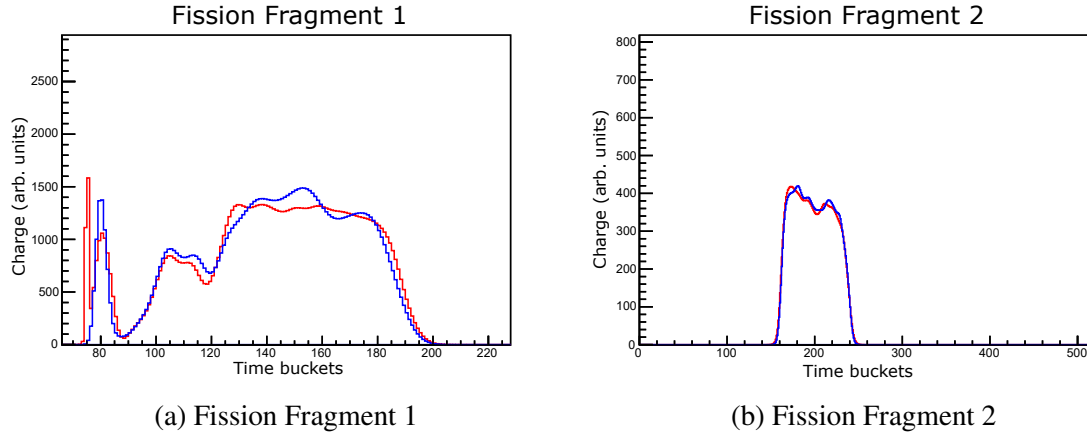
Figure 4.26 dQ/dTB curves for an event. Blue curves are the experimental curves, and red are the simulated curves for the best matching trial event. Simulated curves only contain contributions from good pads in the experimental event.
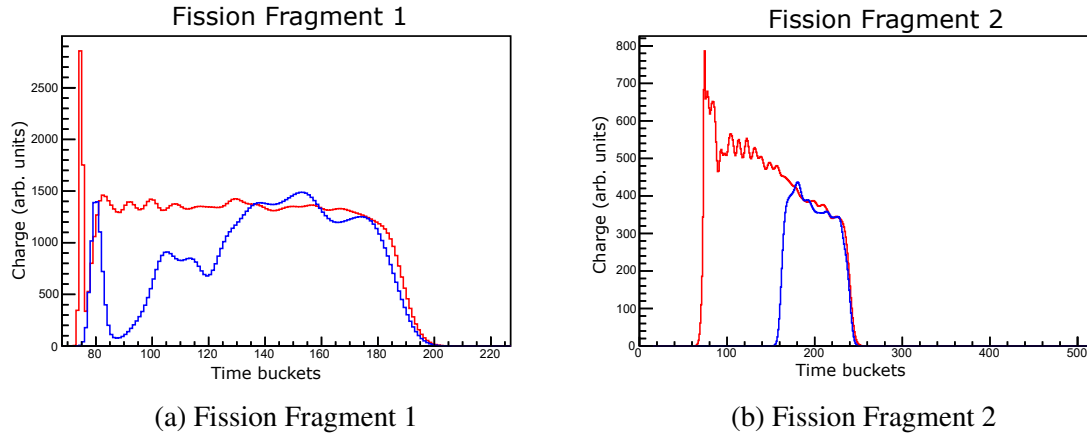
Figure 4.27 dQ/dTB curves for an event. Blue curves are the experimental curves, and red are the simulated curves for the best matching trial event. Simulated curves are complete and contain the charge collected in all pads.

between TB 130 and 80, but maintains the same magnitude across the detector. In the simulated curves the spike around TB 74 is the FF hitting the pad plane.

We determine which trial event best matches the data by examining the following objective function:

$$\chi^2 = \frac{1}{N_{TB}} \sum_i^{N_{TB}} \frac{(Exp_i - A * Sim_i)^2}{Exp_i} \tag{4.27}$$

where N_{TB} is the total number of time buckets in the trimmed dQ/dTB curves for the two fission fragments, Exp_i is the experimental dQ/dTB value for the ith time bucket, Sim_i is the experimental dQ/dTB value for the ith time bucket, and A is the constant of proportionality between the simulated

and experimental charge units.

Because we do not know A, we fit A by minimizing the objective function given in Eqn. 4.27 for each trial event. We then assign the fission fragments their charges by examining which trial event minimized the fit objective function.

As a sanity check, it is useful to examine the behavior of this objective function within a single experimental event. We would expect that as the Z of a fission fragments in a trial event, Z_i, is less similar to the "best" Z, Z_B, the objective function would get larger. This is plotted in Fig. 4.28 for the same event plotted in Fig. 4.26. The behavior follows our expectation where as $Z_B - Z_i$ grows so does χ^2. This plot also gives a sense of what our charge resolution is. The flat bottom between $Z_B - Z_i = -1$ and $Z_B - Z_i = 1$ imply the error on our charge determination is about ± 1 proton.
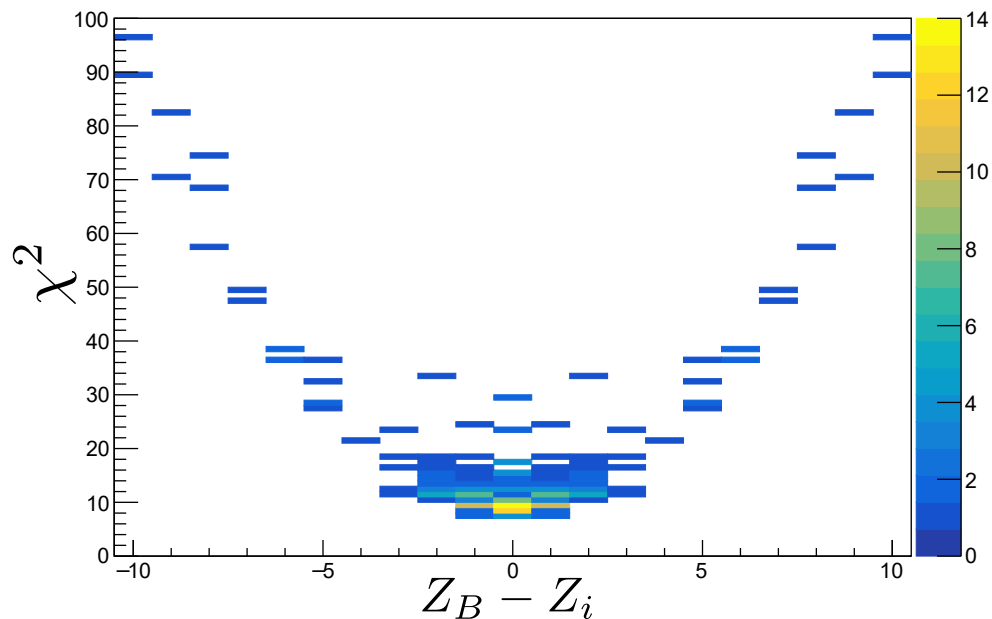
Figure 4.28 The objective function for each trial event is plotted as a function of the difference between the Z of the trial event, Z_i, to the Z of the best trial event, Z_B, for a single experimental event.

4.7   Selecting fission events for charge analysis

4.7.1   Selecting fission events at $90°$

Our analysis for determining the charge, Z, of the fission fragments (discussed in Sec. 4.6) relies on the assumption that the angle between the fission fragments and the beam axis in the CoM frame is $90°$. We will call this angle the decay angle, or θ_{CM}. We can select these events by examining the folding angle between the fission fragments in the lab frame. Fig. 4.29 plots the folding angle vs the vertex location in the AT-TPC (measured from the pad plane) for all ^{204}At fission events in the experiment. The events with decay angles close to $90°$ will be the ones with the largest folding angles. The bright spot centered around $z = 1000$ mm are events that arise from reactions on the entrance window to the AT-TPC. The maximum folding angle depends on the depth in the AT-TPC where the reaction occurs. As the beam looses energy, the magnitude of the boost from the CoM frame to the lab frame is also reduced, increasing the size of the folding angle.
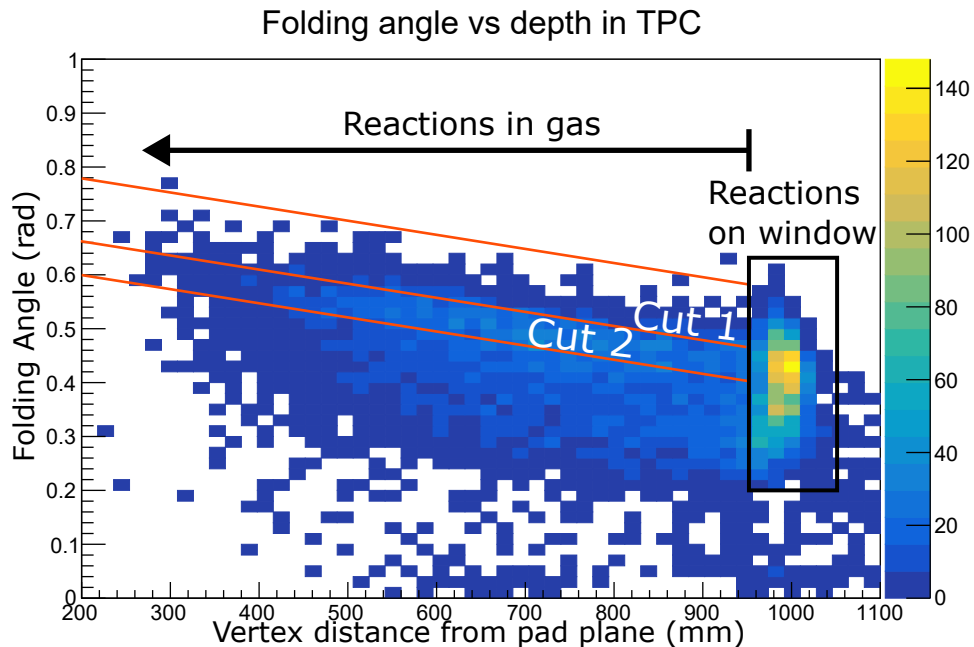
Figure 4.29 Folding angle between fission fragments vs distance from the pad plane for ^{204}At. The cut on large angle fission events is indicated by the two parallel orange lines. The bright spot around 1000 mm are reactions on the window that look fission-like.

There are two cuts marked in Fig. 4.29, a very tight cut on just the largest folding angles marked

as Cut 1, and a second cut that selects events with a slightly smaller folding angle marked as Cut 2. To examine which decay angles we are capturing in these two cuts, and the consequences for the analysis laid out in the Sec. 4.6, we will turn to simulation.

To construct a simulated version of the plot shown in Fig. 4.29 we will use initial results from the analysis described in Sec. 4.6 applied to Cut 1. From that analysis we can extract two pieces of information. First, is an approximation for the expected mass distribution of the fission fragments shown in Fig. 4.30. Second, we can extract the beam energy as a function of depth in the AT-TPC. Fig. 4.31 shows the reconstructed beam energy as a function of depth in the TPC, along with the model (in red) for the beam energy used in this simulation. The model is calculated by taking 5 cm slices of the AT-TPC and fitting the reconstructed energy in each slice with a Gaussian. This gives us a measurement of the average energy of the beam as a function of depth in the TPC, shown in Fig. 4.32. To these measurements we fit a 2nd order polynomial which we take as our model:

$$E(z) = 2713 - 2.30z + 4.55 \times 10^{-4} z^2 \; MeV \tag{4.28}$$

where z is the depth in the AT-TPC (distance from the window) in mm.

There are three things that impact the spread of the beam energy. First is straggling in the material upstream of the TPC, namely the Fe degrader. The thickness was quoted from Goodfellow Metals, the manufacturer, to be $0.25 \pm 2.5\%$ mm. The foil is 5 cm X 5 cm, and the beam spot on the foil is not small compared to the foil area. A basic LISE++ calculation implies that the expected variation in energy at the TPC from variations in the foil thickness is more than 600 MeV. Second are the assumptions in the method for determining the velocity of the fission fragments in the CoM frame, namely the error in the assumed decay angle and uncertainty in Viola systematics. Third is any error in measuring the folding angle between the fission fragments in the Lab frame, which is used to extract the beam energy.

With these physical inputs, we can now perform the simulation. For each event, we sample the mass of one fission fragment, A_1, following the Gaussian distribution plotted in Fig. 4.30, and set the mass of the other fragment to be $A_2 = A_{CN} - A1$, where A_{CN} is the mass number of

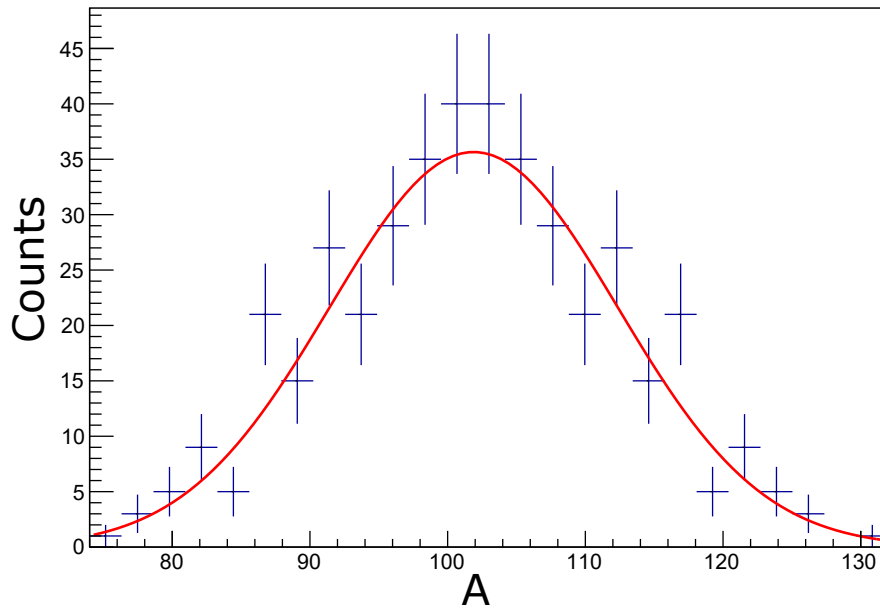Figure 4.30 Initial experimental measurement of the mass distribution of the fission of ^{204}At with Cut 1 applied to the data. The red line is the best fit for a Gaussian that is used as our probability distribution for the mass of the FF in the simulation.
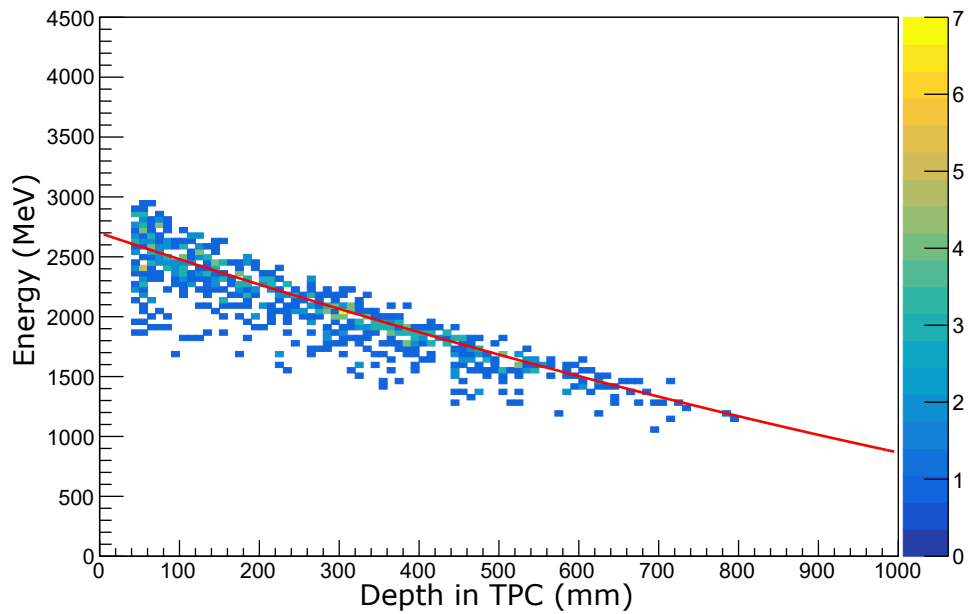
Figure 4.31 Experimentally reconstructed beam energy as a function of depth in the AT-TPC. The red line is our model for the energy loss.
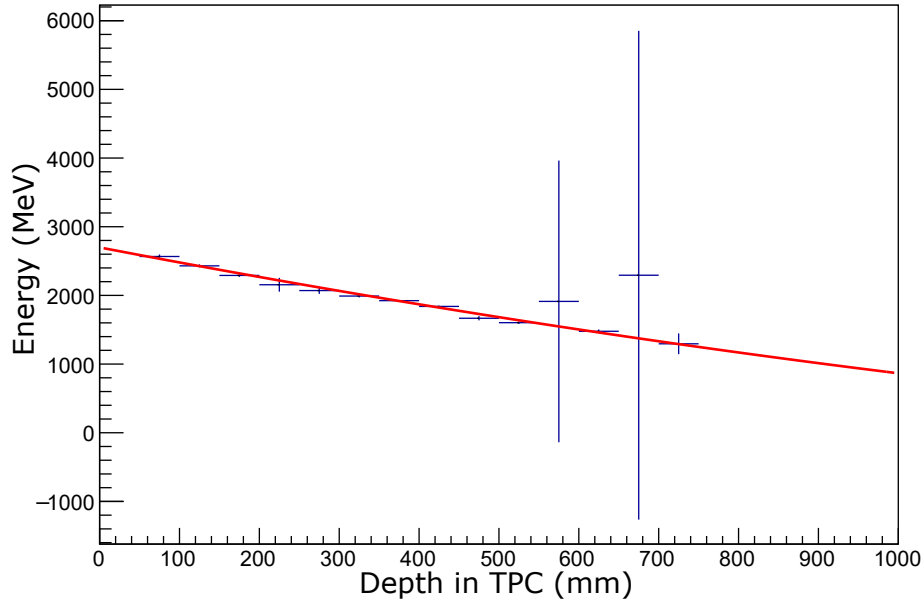
Figure 4.32 Each point is the mean of a Gaussian fit to the experimentally reconstructed beam energy for all fission events in Cut 1 that occurred in a 5 cm slice of the AT-TPC . Error bars are the fit errors. The red line is a second order polynomial fit.

the compound nucleus, 204 in this case. We then assign the charges, Z_1 and Z_2 by maximizing the total binding energy of the fission fragments, and assuming $Z_{CN} = Z_1 + Z_2$. Finally we set the decay direction, assuming the decay angle follows the anisotropy distribution measured by Huizenga et. al. for ^{197}Au(α, f) [76]. As seen in Fig. 4.33, near 90° this distribution follows a $1/\sin\theta$ distribution that is typical of higher beam energies or fusion-fission with heavier ions [77]. Because this simulation purpose is to determine which decay angles are captured by the cuts on the folding angle in the lab frame, the exact shape of the anisotropy distribution is not relevant to the conclusion of this analysis. Changing the anisotropy distribution just changes the number of events in the cuts on folding angle, not the relationship between folding angle and decay angle.

To boost from the CoM to the lab frame, we sample the location of the decay in the AT-TPC, assuming a uniform distribution along the length of the detector. Once again, the distribution assumed will not effect the conclusion of the analysis, just the number of counts within each cut. From that we can calculate the kinetic energy of the beam through Eqn. 4.28, and by extension the boost between the two frames. Fig. 4.34 shows the simulated version of the folding angle

Anisotropy distribution

Figure 4.33 Decay angle in the CoM frame for ^{204}At following the anisotropy distribution measured by Huizenga et. al. [76] for ^{197}Au(α, f). The red line is a $1/\sin\theta$ distribution.

Simulated folding angle vs depth in TPC
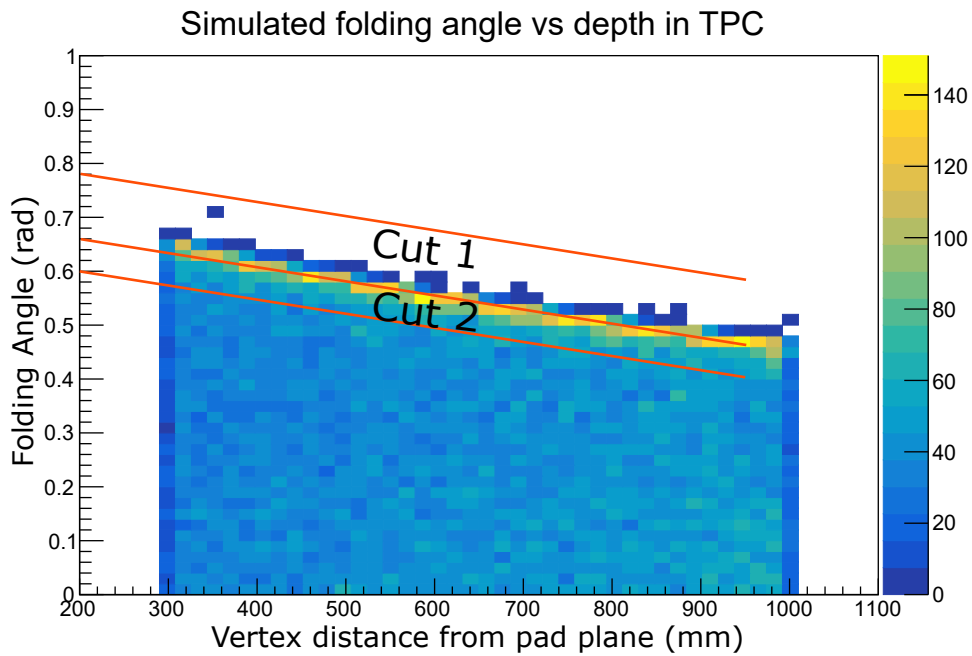
Figure 4.34 Simulated folding angle between fission fragments vs distance from the pad plane for ^{204}At.

| (a) Cut 1 | (b) Cut 2 |
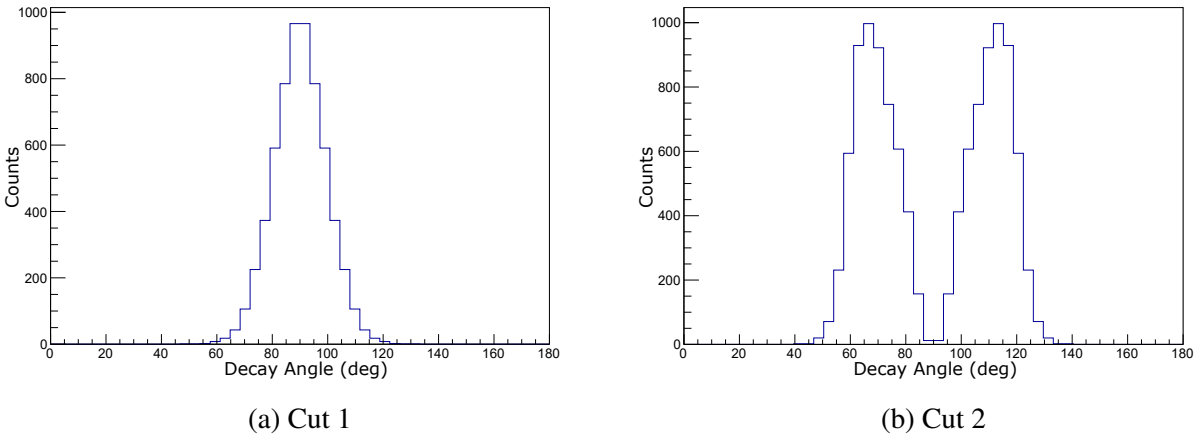
Figure 4.35 Decay angles with respect to the beam axis in events captured by Cut 1 in (a) and Cut 2 in (b). Based on simulation (we have no direct experimental measurement of decay angle).
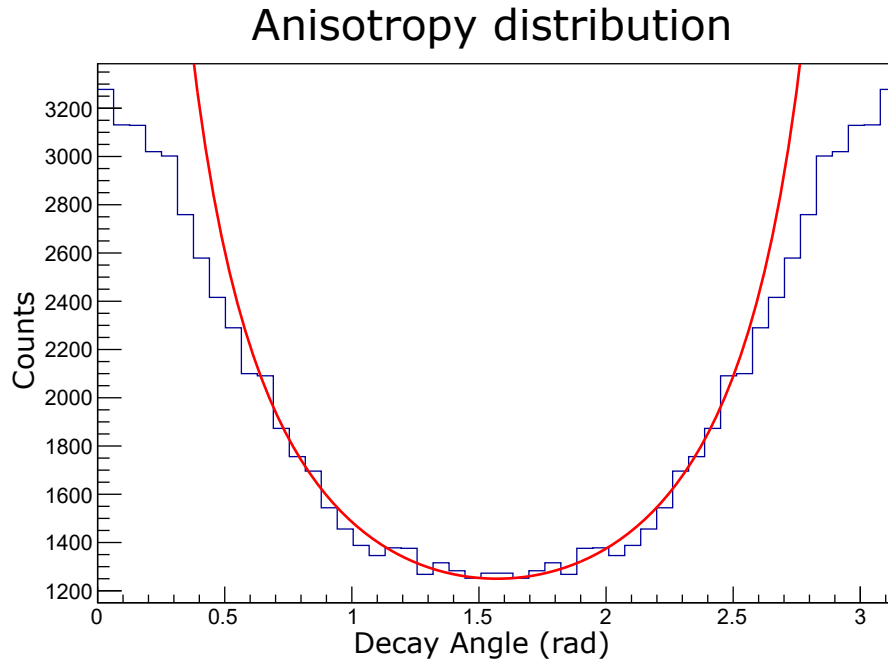
plot in Fig. 4.29, with the same cuts drawn. There is good agreement between the simulated, and experimental plots, especially in the region of interest at the largest folding angles. To recover the behavior at smaller folding angles, the trigger and its dependence on the low gain beam region would need to be accounted for.

Applying Cut 1 and Cut 2 to the simulated data we can examine the decay angles captured by the cuts, which are shown in Fig. 4.35. Cut 1 is peaked around 90°, while cut 2 contains almost no events at 90°, and is instead peaked around 110°. To understand the impact this will have on the analysis described above, it is more useful to look at how the velocities of the fission fragments in the lab frame compare to the velocities we assume in the analysis. This is shown for the two cuts in Fig. 4.36. In both these plots, the particles with $v_{assumed}/v_{actual} < 1$ correspond to the FFs that are in the forward direction ($\theta_{CM} < \pi/2$), and events with $v_{assumed}/v_{actual} > 1$ correspond to the FFs that are in the backwards direction ($\theta_{CM} > \pi/2$).

From this analysis, its clear that a tight cut, such as cut 1, is required to apply the analysis laid out in Sec. 4.6 with the current assumptions. In principle, one could extend the analysis to allow the decay angle to be a sampled parameter along with the charge of the fission fragments. That extension of the analysis is beyond the scope of this thesis, but we will provide here some evidence that the extension is potentially feasible.

The analysis to determine the charge of the fission fragments comes down to matching energy

125

(a) Cut 1   (b) Cut 2
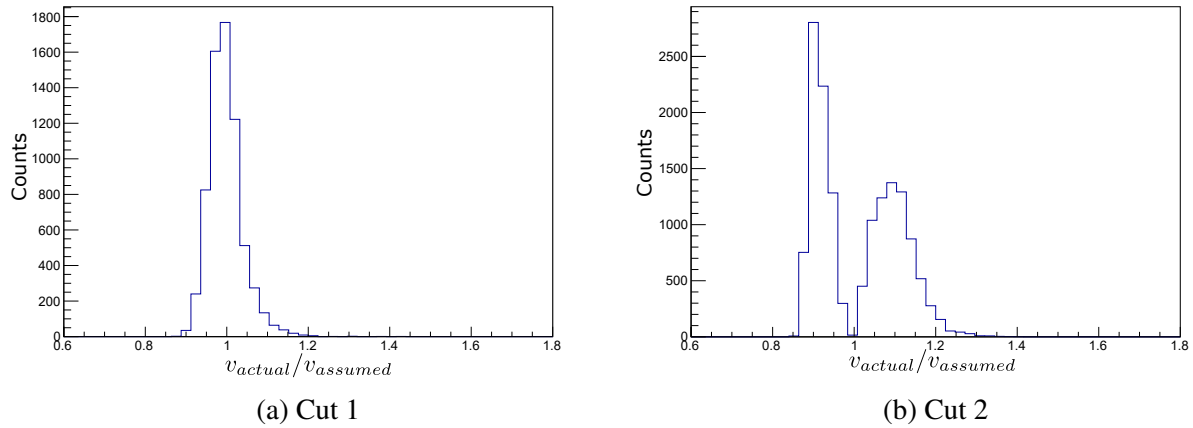
Figure 4.36 Simulated ratio between the reconstructed velocity assuming the decay angle is 90°, v_{assume} and the actual velocity of the fission fragments in the lab frame v_{actual}.

loss curves between the experimental data and the simulation. The effect of changing the decay angle is to change the initial velocity of the fission fragments. Because the stopping power of an ion has a strong dependence on the velocity of the ion, its critical the initial velocities of the fission fragments are well described.

The limiting factor to the reconstruction of Z, while allowing the decay angle to vary, is an ambiguity in our observable. One can get multiple charge splittings in simulated events that are consistent with the experimental event by selecting different decay angles. We examine two observables to characterize the extent of this problem, both shown in Fig. 4.37. Fig. 4.37a plots the ratio of the stopping power for the two FF at the vertex. Fig. 4.37b plots the ratio of the energy loss of the two FF in in the He gas after traveling 50 cm. The decay angle is taken to be the angle between the more massive fission fragment and the beam direction in the CoM frame. Both these plots contain dashed red lines that indicate a single value of the observable in question. In both cases the observable is consistent with multiple charge splittings.

Without additional information on the decay angle, it is not possible to uniquely identify the charge splitting of the fission fragments. A single value of the observables can be consistent with symmetric to the most asymmetric charge splittings. It's only when a cut on decay angle can be made that the observables become unique identifiers of the charge splitting. As evidenced in Fig. 4.35, we can extract some information on the decay angle from the relationship between the folding

(a) Ratio of stopping power of the FF   (b) Ratio of the energy loss of the FF
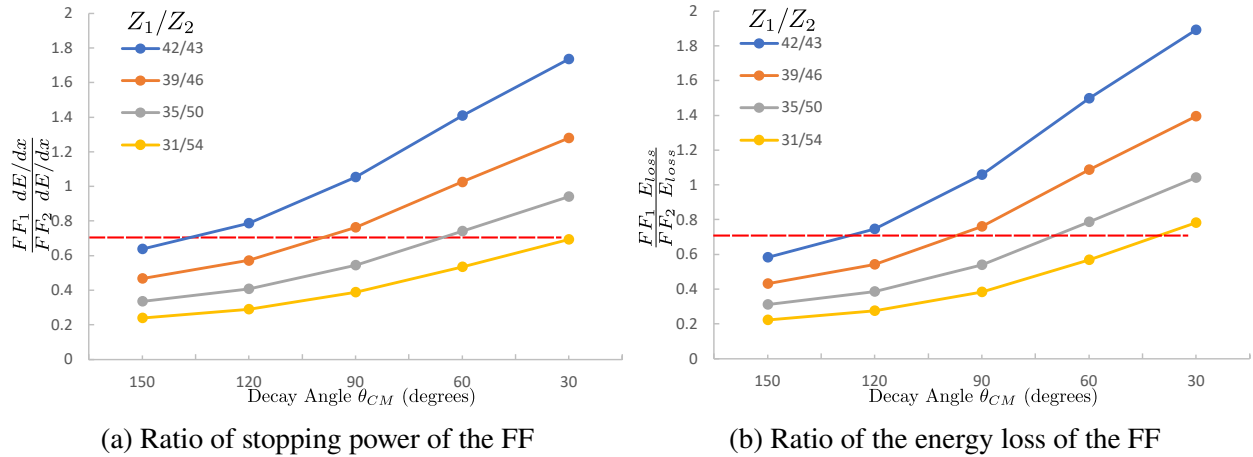
Figure 4.37 Plotted are two potential observables for determining the charge of the fission fragments for events located 10 cm from the window of the AT-TPC as a function of the angle between the beam direction and the more massive fission fragment in the CoM frame. (a) plots the ratio of the stopping power of the fission fragments with various charge splits. (b) plots the ratio of the total energy loss after each fragment has traveled 50 cm in the AT-TPC. The red lines are to guide the eye, at a single value of the observable in questions multiple charge splittings are consistent with the value of the observable.

angle and vertex location (which is acting here as a proxy for the energy of the beam). Future work will determine if the selection of decay angles from these observables is sufficient to remove the ambiguity discussed here.

4.7.2 Identifying fits that converge

After we have selected fission events with the largest folding angles (Cut 1 in Fig. 4.29) and have run the MC Fit analysis described above, the final step in recovering a charge distribution is to identify which event the MC fitting algorithm was able to successfully fit. This is, we need to establish a fit quality criterion where we determine when the MC fitting is successful and when it fails.

Our overall goal is to determine where to place a cut on the the data so we limit our selection to events where the fit converged. We know the fit is not always converging after the selection of just large angle events. This is evidenced by how value of the objective function changes as a function of $Z_b - Z_i$. Here we use the same definitions of Z_b and Z_i as we did in Fig. 4.28. Fig. 4.38a shows the relationship between χ^2 and $Z_b - Z_i$ for all events in our angle cut. There is structure in this plot beyond the simple parabolic shape seen in Fig. 4.28, particularly around $Z_B - Z_i = 0$ where

(a) All events   (b) Only selected events

Figure 4.38 Relationship between the objective function and difference in Z between the best fit for an event and all the trial events. a) is all events. b) is selected events after the cuts discussed in the text are applied.
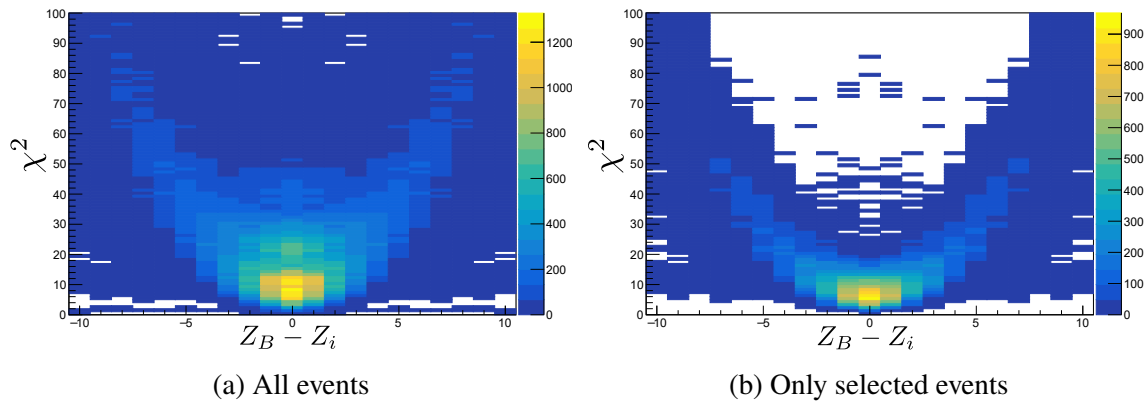
it appears as if the pattern from Fig. 4.28 has been duplicated at higher values of the objective function. This is also visible in the distribution of χ^2 for the fits. There is a second, smaller peak around $\chi^2 = 18$. The events with larger values of χ^2 correspond to events we cannot fit well.

There are three primary classes of events that we do not fit well and are removed by this cut. First, are events where the space charge correction is insufficient, or the Y-fit does a poor job describing the data. Fig. 4.39 shows an example simulated and experimental dQ/dTB curve where that is the case, particularly for fission fragment 1. An insufficient space charge correction expresses itself as an offset in the time the charge that originated near the vertex is collected. Near the pad plane, where the magnitude of the space charge effect is smaller the simulated and experimental curves overlap again. This is seen in the curves in Fig. 4.39a where the simulated curve is offset from the experimental curve at large time buckets, but is not at small time buckets near the pad plane. The effect of this can also be seen in the 3D data where the simulated and experimental hits do not overlap near the vertex as seen in Fig. 4.40.

The second main class of events we fail to fit are ones where the experimental dQ/dTB curves are malformed. We believe the primary cause of this is issues with the baseline of the traces. An example of this class of event is given in Fig. 4.41. The rise of the dQ/dTB curve for FF2 has structure that cannot be explained by missing pads. The curve rises in two steps and then begins declining. Fig. 4.42 shows the ADC trace and reconstructed charge for a pad associated with fission

| Fission Fragment 1 | Fission Fragment 2 |
| (a) Fission Fragment 1 | (b) Fission Fragment 2 |
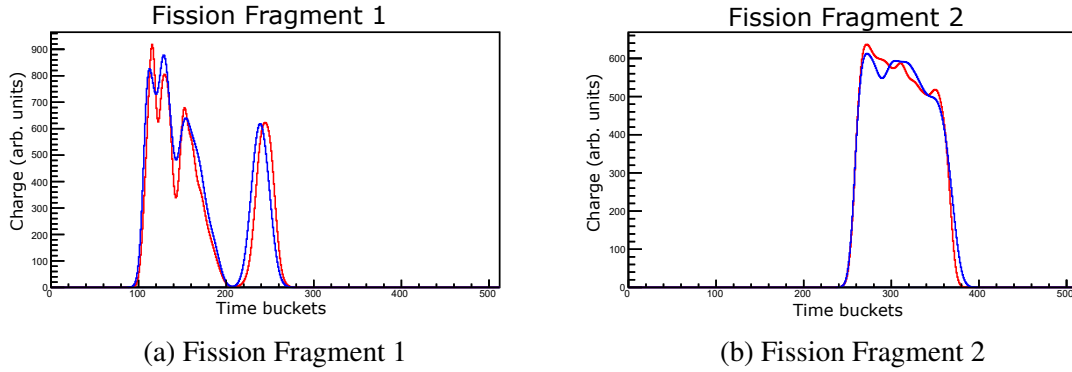
Figure 4.39 dQ/dTB curves for an event where the space correction is insufficient. This expresses itself as an offset in the time of charge collection near the vertex (higher time buckets). Near the pad plane, where the magnitude of the space charge effect is smaller the curves overlap again. Red is the simulated dQ/dTB curve and blue is the experimental dQ/dTB curve.
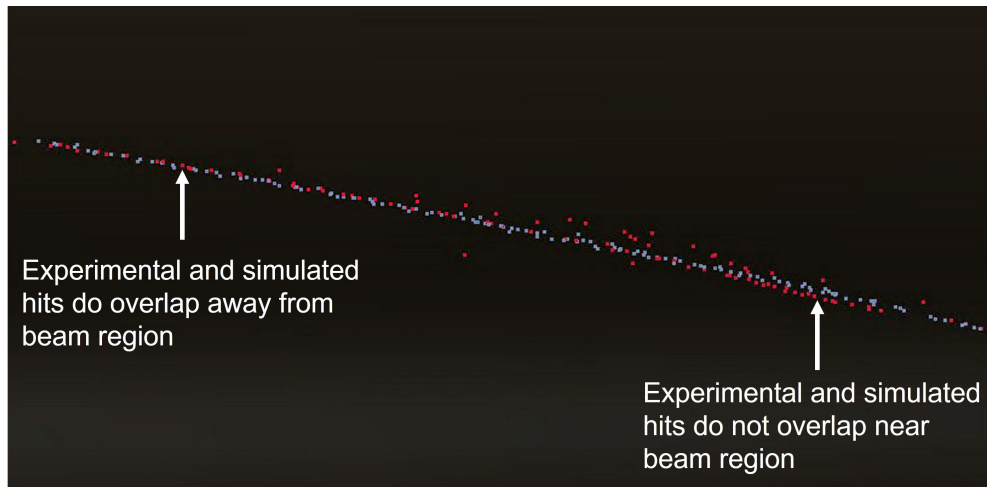
Figure 4.40 Simulated (grey) and experimental (red) hits in the TPC. The experimental hits have not been corrected for space charge. The shift in location between the red and grey hits for one track is indicative of an insufficient space charge correction.

fragment 2 that is indicative of the issue. The large non-constant baseline causes the reconstructed charge to be anomalously high, distorting our dQ/dTB curve. If this were just a single pad, or uncorrelated in an event it would probably not be an issue; however, the baseline fluctuations are correlated within an AsAd, as discussed in Sec. 3.4.1, and pads within an AsAd are typically close to each other on the pad plane. As a result, the effect of the baseline will be compounded while the fragment remains over pads belonging to that AsAd magnifying the distortion of the dQ/dTB curve. For example, in the event depicted in Fig. 4.41 the magnitude of the baseline near the signal is about 4-5 (arb. units) for traces in CoBo 3 AsAd 2 as seen in Fig. 4.42. Fission fragment 2

(a) Fission Fragment 1

(b) Fission Fragment 2
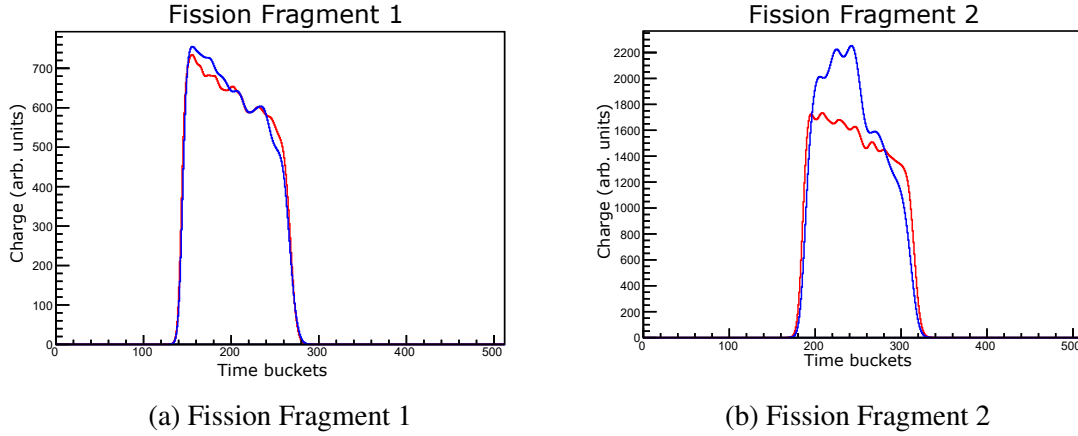
Figure 4.41 dQ/dTB curves for an event where the experimental curve is malformed from a large baseline distortion that is correlated within an AsAd and compounded over many pads.

(a) Trace

(b) Reconstructed charge
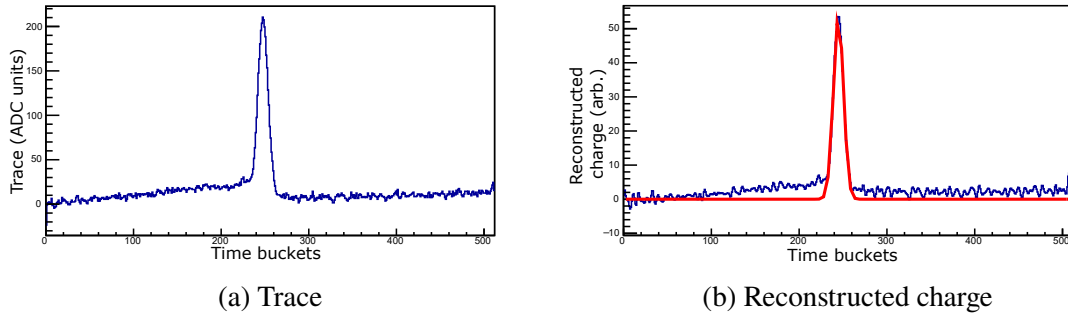
Figure 4.42 ADC trace (a) and reconstructed charge (b) for a pad in CoBo 3 AsAd 2 associated with fission fragment 2 in Fig. 4.41.

passes through 137 pads in this AsAd, implying the expected distortion in the total dQ/dTB curve to be 548 to 685. This is close in magnitude to the observed distortion in Fig. 4.41.

The third and final class of events we fail to fit well are those where one of the fission fragments does not pass over enough good pads to construct a reasonable dQ/dTB curve. These typically are events where one of the fission fragments passes over the region of the pad plane corresponding to CoBo 2 AsAd 3 which was malfunctioning throughout the experiment.

We remove these events by placing a cut on χ^2 (Eqn. 4.27) at 15, the line marked in red in Fig. 4.43. This removes the bulk of the bad events. We can get a cleaner sample by adding an additional cut to the scaling factor of between the simulated and experimental dQ/dTB curves. We call this the "A Cut". This cut is marked by the red box in Fig. 4.44, and the χ^2 distribution after this cut is show in Fig. 4.43b. Because there are only 593 event in our large angle cut, Cut 1, we can label by

Objective Function Charge

(a) All events (b) Only selected events
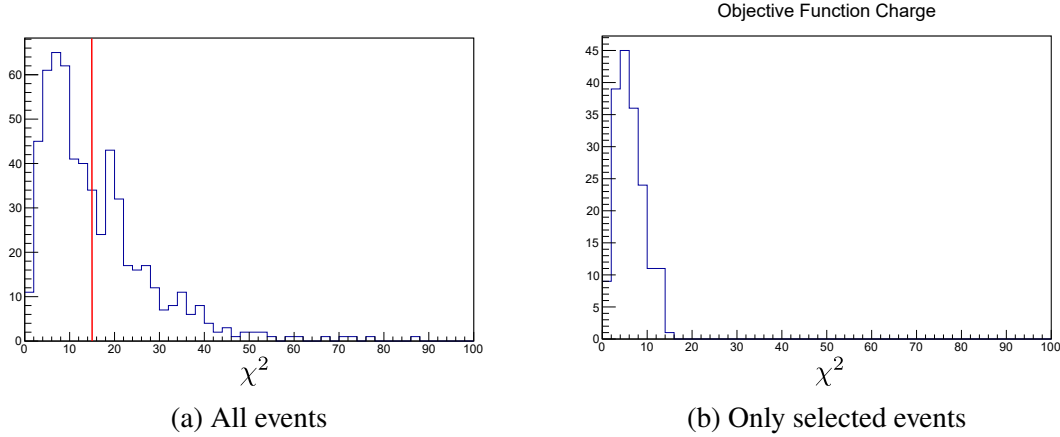
Figure 4.43 Value of objective function for the trial event that best described the data. a) is all events. b) is selected events after the cuts discussed in the text are applied.

Event Class	Total	χ^2 Cut	χ^2 and A Cut
Good Events	155	150	147
Space Charge	34	8	3
Malformed	365	175	87
Too few pads	40	26	16

Table 4.7 Results of labeling all events in Cut 1.

Excitation Energy (MeV)	Sigma (Z)	Amplitude (counts)
All Events	5.34 ± 0.20	34.8 ± 2.0
E* < 35	4.84 ± 0.25	23.4 ± 1.8
E* > 35	6.87 ± 0.68	9.7 ± 1.0

Table 4.8 Table of the parameters resulting from fitting the charge distributions at different excitation energy ranges.

hand if they fall into any category that would make them difficult to fit. We can then asses how well our cuts remove the events in these categories. The results of this labeling are given in Table 4.7.

4.8 Charge (Z) distribution of ^{200}Bi(^{4}He,f)

After applying the cuts described in the previous section, we can now recover a charge distribution taking the Z from the best trial event in the Monte-Carlo fitting method. The charge distribution for ^{204}At, our most abundant species, is shown in Fig. 4.45. The results of the fit are enumerated in Table 4.8

Our measured charge distribution extends across a range of beam energies. Fig. 4.31 plots the reconstructed beam energy as a function of depth in the TPC. The energy of the beam is inferred

Figure 4.44 Value of objective function for all events. Red line indicates the cut made on the value of the objective function to select events where the fit is good.

Figure 4.45 Z distribution for fission of ^{204}At.

(a) E* > 35 MeV   (b) E* < 35 MeV

Figure 4.46 Z distribution for fission of ^{204}At for two different ranges of excitation energy
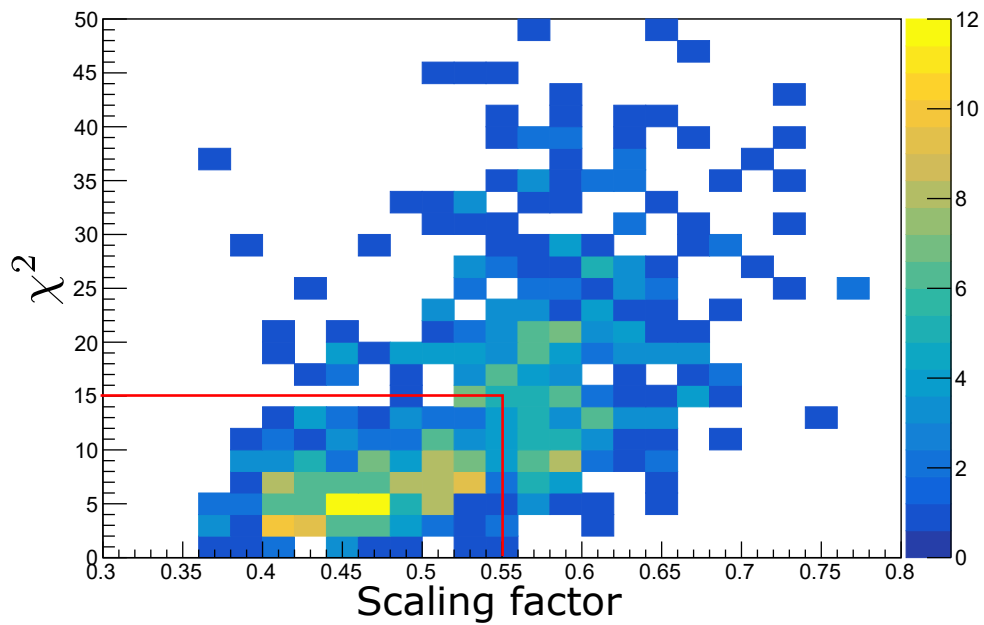
Energy Loss Model	Sigma (Z)	Amplitude (counts)
SRIM	5.34 ± 0.20	34.8 ± 2.0
LISE	5.24 ± 0.28	26.3 ± 1.9

Table 4.9 Table of the parameters resulting from fitting the charge distributions using different energy loss models.

through momentum and energy conservation from the reconstructed momentum of the fission fragments (see eqn. 4.25).

Although we have limited statistics, we can plot the charge distribution for different excitation energies, shown in Fig. 4.46 where we plot the Z distribution for events with $E* < 35$ MeV and events with $E* > 35$ MeV. The fit parameters are given in Table 4.8. Our results are consistent with previous measurements in this mass region where the width of the mass distribution is expected to increase with increasing excitation energy [78].

As a consistency check, we repeated the analysis described in Sec. 4.7.2 for the MC fitting method using energy loss table from LISE instead of SRIM. As seen in Fig.4.47 the correlation between the scaling factor, A and χ^2 when using LISE tables is qualitatively similar to Fig. 4.44 using SRIM tables. The primary difference is the scaling factor is centered on a different value. This is not unexpected, as the energy loss models can be quite different in magnitude as seen in Fig. 4.1. The resulting charge distribution is shown in Fig. 4.48, and the fit parameters are given in Table 4.9. The fits and distributions are consistent across the two models.

In the seminal experiment by Schmidt et al. [15] charge distributions were measured for the two

Figure 4.47 Value of objective function for all events using LISE energy loss tables for the fission fragments. The red line indicates the cut made on the value of the objective function to select events where the fit is good.
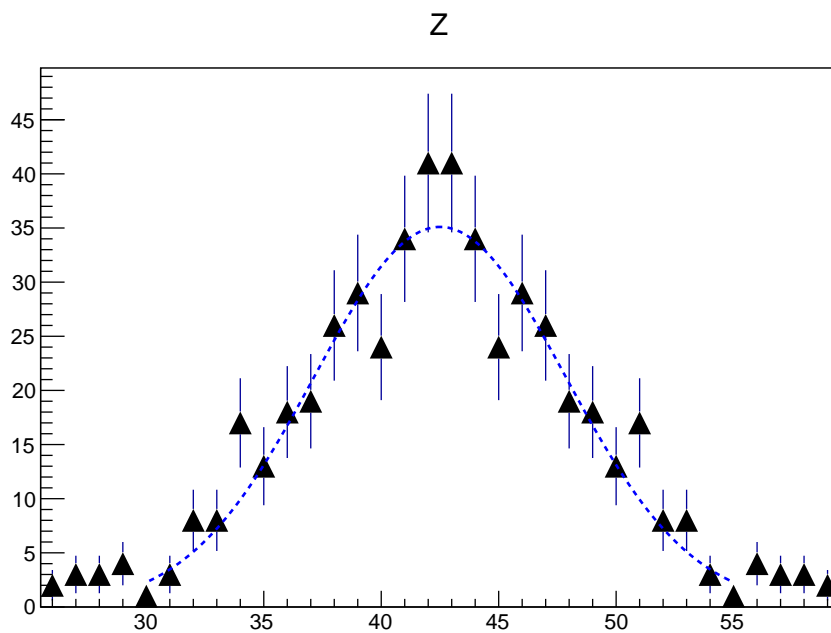

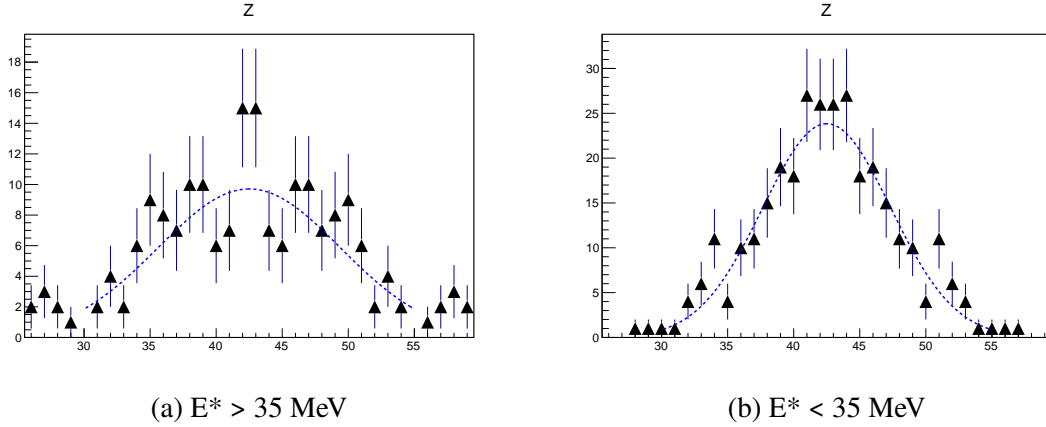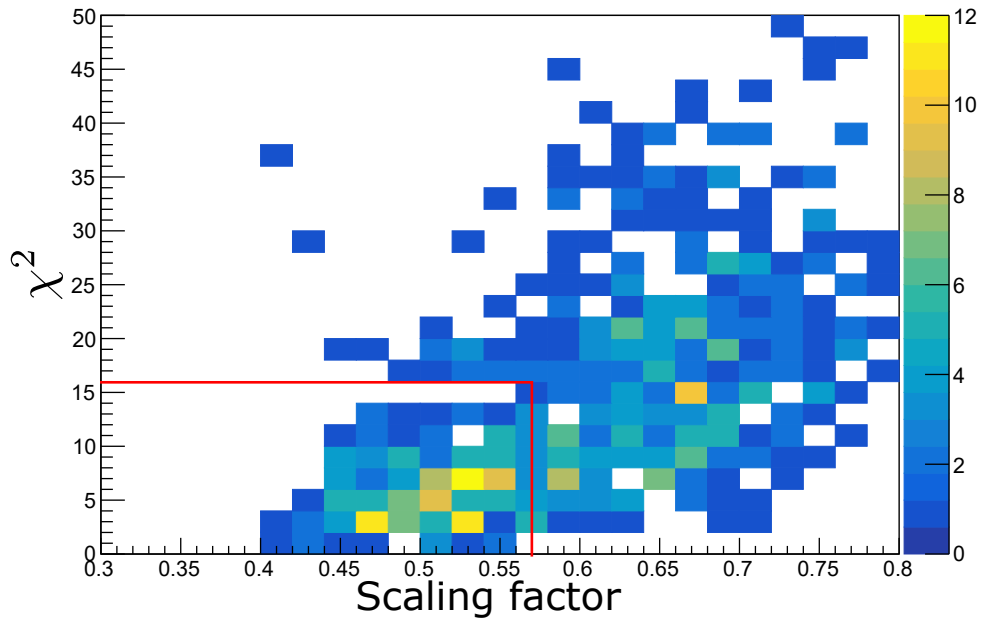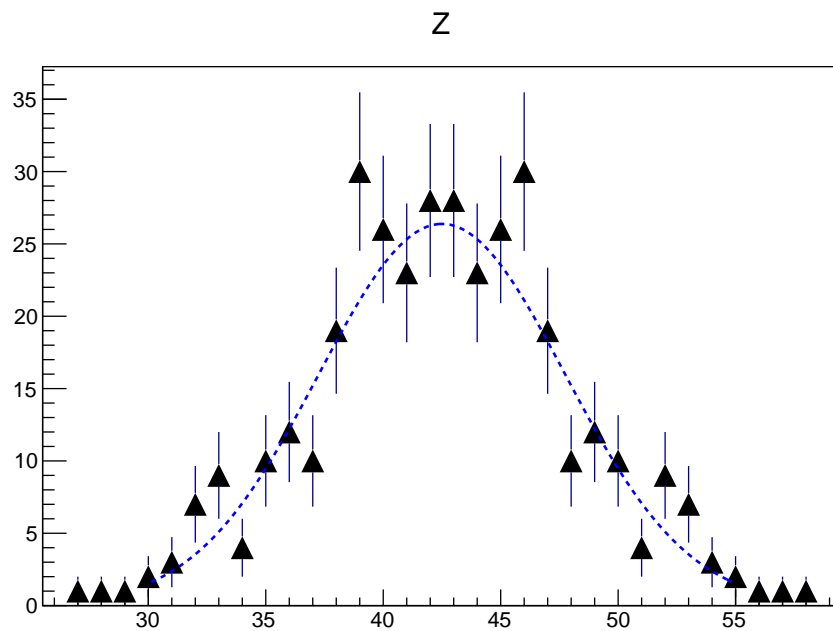Figure 4.48 Z distribution for fission of ^{204}At using LISE energy loss tables.

next heaviest At nuclei, ^{205}At and ^{206}At. Like our experiment, they only reported a single width for the charge distributions, albeit with higher statistics. Their experiment also covered a range of excitation energies, but they could not determine the excitation energy on an event by event basis. Fig. 4.49 plots the measured widths of the charge distributions measured by Schmidt et. al. for At along with the measurement in this thesis. We plot our measurement for E* < 35 MeV as it is closer to the range of excitation energy measured by Schmidt et. al. As expected for these nuclei, the width of the charge distribution increases as the mass decreases. This is demonstrated by two theoretical prediction for the width of the charge distributions plotted in the same figure, one from Moller et. al. [14] and a second from Mumpower et. al. [79]. Moller et. al. only calculated mass distributions. To estimate the charge distribution we have fit the predicted mass yields with a Gaussian to get a prediction for σ_A and assumed $\sigma_Z = Z/A\sigma_A$. Mumpower et. al. calculated the yield as function of both charge and mass. We just fit the charge yields with a Gaussian to get σ_Z to compare. The experimental measurements sit between the two theory predictions. Importantly, how the width changes as a function of mass number is consistent across the two theory predictions and data.

Figure 4.49 Width of charge distributions for At nuclei from [15] ($^{206-206}$At) and this work (^{204}At). Theory comparisons are from Moller et. al. [14] where only mass distributions were calculated and Mumpower et. al. [79] where mass and charge distributions were calculated.

CHAPTER 5

CONCLUSION AND OUTLOOK

A new detector system, the HEavy ISotope Tagger (HEIST) was developed to identify heavy, incompletely stripped beams at the NSCL, and in the future FRIB [80]. HEIST was able to successf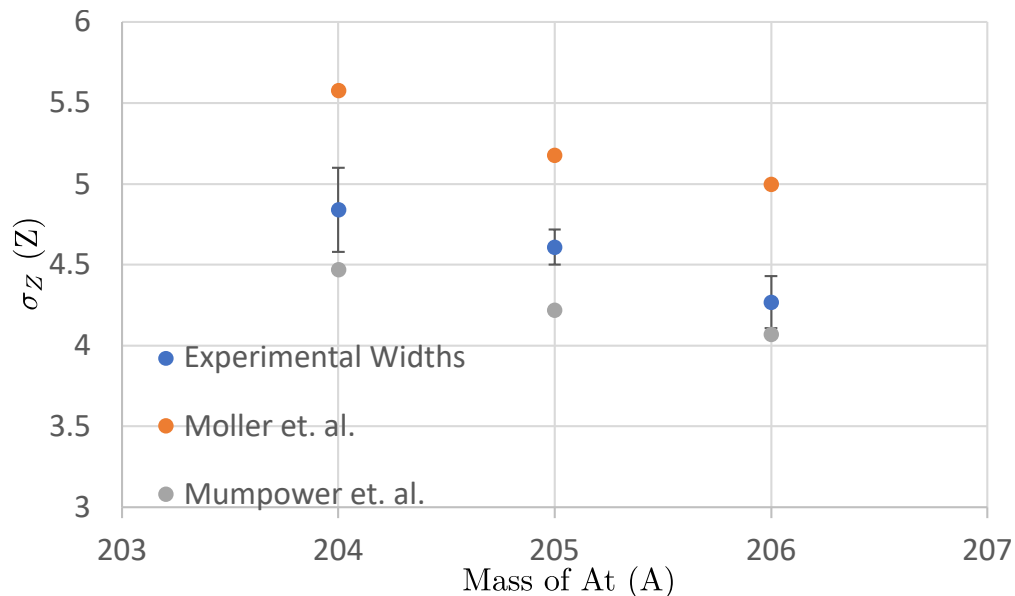ully identify beams resulting from the fragmentation of ^{208}Pb on ^{9}Be at $\sim$ 75 MeV/A. We were able to identify the isotope as well as the charge state. This allowed us to compare our measured charge state distributions with the charge state model GLOBAL. We found there was good agreement between the two if a slight adjustment was made to the energy of the beam.

HEIST was coupled with the Active-Target Time Projection Chamber (AT-TPC) to measure the fission properties of nuclei in the pre-actinide region. Fission was induced through fusion with He gas in the AT-TPC. We demonstrated for the first time the operation of the AT-TPC in the fast beam region of the NSCL and the successful linking of the HEIST DAQ with the AT-TPC DAQ. We were able to identify over 99% of the fission events captured in our trigger.

New analysis techniques were developed for the AT-TPC including the development of a new pattern recognition framework based on the RANSAC algorithm. A method to deconvolve the measured traces to recover the current collected on the pads was also developed, critical for using energy loss information to identify the charge (Z) of the fission fragments. In addition , a new Monte-Carlo based fitting technique was developed to identify the Z of the fission fragments. This was used to measure the Z distribution of the fragments from the fission of ^{204}At where we saw a predominantly symmetric distribution. The measured charge distribution is consistent with previous measurements of ^{205}At and ^{206}At, along with theoretical predictions.

There are three main thrusts to the planned future work on this experiment. First is the application of additional corrections to the traces to remove the baseline effects and improve the statistics of the measured charge distributions. Second, is applying the developed techniques to all isotopes measured in the experiment. Third, is the development of a method to measure the fission cross section as a function of excitation energy.

BIBLIOGRAPHY

[1] *National Nuclear Data Center, information extracted from the NuDat database.* URL: https://www.nndc.bnl.gov/nudat/.

[2] *Nuclear Binding Energy.* [Online; accessed 2023-06-06]. Sept. 2022.

[3] G. Gamow and Ernest Rutherford. "Mass defect curve and nuclear constitution". In: *Proceedings of the Royal Society of London. Series A, Containing Papers of a Mathematical and Physical Character* 126.803 (1930), pp. 632–644. DOI: 10.1098/rspa.1930.0032. eprint: https://royalsocietypublishing.org/doi/pdf/10.1098/rspa.1930.0032. URL: https://royalsocietypublishing.org/doi/abs/10.1098/rspa.1930.0032.

[4] C. F. v. Weizsäcker. "Zur Theorie der Kernmassen". In: *Zeitschrift für Physik* 96.7 (July 1935), pp. 431–458. ISSN: 0044-3328. DOI: 10.1007/BF01337700. URL: https://doi.org/10.1007/BF01337700.

[5] Daniel FR. *llustration of the terms of the semi-empirical mass formula in the liquid-drop model of the atomic nucleus.* [Online; accessed 6-June-2023]. 2012. URL: https://en.wikipedia.org/wiki/Semi-empirical_mass_formula#/media/File:Liquid_drop_model.svg.

[6] Lise Meitner and O. R. Frisch. "Disintegration of Uranium by Neutrons: a New Type of Nuclear Reaction". In: *Nature* 143.3615 (Feb. 1939), pp. 239–240. ISSN: 1476-4687. DOI: 10.1038/143239a0. URL: https://doi.org/10.1038/143239a0.

[7] C. Gustafsson, P. Möller, and S.G. Nilsson. "The microscopic mechanism behind the fission barrier asymmetry". In: *Physics Letters B* 34.5 (1971), pp. 349–353. ISSN: 0370-2693. DOI: https://doi.org/10.1016/0370-2693(71)90621-6. URL: https://www.sciencedirect.com/science/article/pii/0370269371906216.

[8] A. N. Andreyev et al. "New Type of Asymmetric Fission in Proton-Rich Nuclei". In: *Phys. Rev. Lett.* 105 (25 Dec. 2010), p. 252502. DOI: 10.1103/PhysRevLett.105.252502. URL: https://link.aps.org/doi/10.1103/PhysRevLett.105.252502.

[9] J. D. McDonnell et al. "Excitation-energy dependence of fission in the mercury region". In: *Phys. Rev. C* 90 (2 Aug. 2014), p. 021302. DOI: 10.1103/PhysRevC.90.021302. URL: https://link.aps.org/doi/10.1103/PhysRevC.90.021302.

[10] Takatoshi Ichikawa et al. "Contrasting fission potential-energy structure of actinides and mercury isotopes". In: *Phys. Rev. C* 86 (2 Aug. 2012), p. 024610. DOI: 10.1103/PhysRevC.86.024610. URL: https://link.aps.org/doi/10.1103/PhysRevC.86.024610.

[11] Peter Möller, Jørgen Randrup, and Arnold J. Sierk. "Calculated fission yields of neutron-

deficient mercury isotopes". In: *Phys. Rev. C* 85 (2 Feb. 2012), p. 024306. DOI: 10.1103/PhysRevC.85.024306. URL: https://link.aps.org/doi/10.1103/PhysRevC.85.024306.

[12]   Guillaume Scamps and Cédric Simenel. "Effect of shell structure on the fission of sub-lead nuclei". In: *Phys. Rev. C* 100 (4 Oct. 2019), p. 041602. DOI: 10.1103/PhysRevC.100.041602. URL: https://link.aps.org/doi/10.1103/PhysRevC.100.041602.

[13]   T. Ichikawa and P. Möller. "The microscopic mechanism behind the fission-barrier asymmetry (II): The rare-earth region 50 <Z<82 and 82<N<126". In: *Physics Letters B* 789 (2019), pp. 679–684. ISSN: 0370-2693. DOI: https://doi.org/10.1016/j.physletb.2018.12.034. URL: https://www.sciencedirect.com/science/article/pii/S0370269318309614.

[14]   Peter Möller and Jørgen Randrup. "Calculated fission-fragment yield systematics in the region $74 \leq Z \leq 94$ and $90 \leq N \leq 150$". In: *Phys. Rev. C* 91 (4 Apr. 2015), p. 044316. DOI: 10.1103/PhysRevC.91.044316. URL: https://link.aps.org/doi/10.1103/PhysRevC.91.044316.

[15]   K.-H. Schmidt et al. "Relativistic radioactive beams: A new access to nuclear-fission studies". In: *Nuclear Physics A* 665.3 (2000), pp. 221–267. ISSN: 0375-9474. DOI: https://doi.org/10.1016/S0375-9474(99)00384-X. URL: https://www.sciencedirect.com/science/article/pii/S037594749900384X.

[16]   Oleg B. Tarasov. "Observation of new neutron-rich isotopes at the NSCL". in: *AIP Conference Proceedings* 1224.1 (2010), pp. 195–205. DOI: 10.1063/1.3431415. eprint: https://aip.scitation.org/doi/pdf/10.1063/1.3431415. URL: https://aip.scitation.org/doi/abs/10.1063/1.3431415.

[17]   T Kubo et al. "The RIKEN radioactive beam facility". In: *Nuclear Instruments and Methods in Physics Research Section B: Beam Interactions with Materials and Atoms* 70.1-4 (1992), pp. 309–319.

[18]   Hans Geissel et al. "The GSI projectile fragment separator (FRS): a versatile magnetic system for relativistic heavy ions". In: *Nuclear Instruments and Methods in Physics Research Section B: Beam Interactions with Materials and Atoms* 70.1-4 (1992), pp. 286–297.

[19]   D _ J Morrissey et al. "Commissioning the A1900 projectile fragment separator". In: *Nuclear Instruments and Methods in Physics Research Section B: Beam Interactions with Materials and Atoms* 204 (2003), pp. 90–96.

[20]   J Bradt et al. "Commissioning of the active-target time projection chamber". In: *Nuclear Instruments and Methods in Physics Research Section A: Accelerators, Spectrometers, Detectors and Associated Equipment* 875 (2017), pp. 65–79.

[21]   A Gade and BM Sherrill. "NSCL and FRIB at Michigan State University: Nuclear science

at the limits of stability". In: *Physica Scripta* 91.5 (2016), p. 053003.

[22]   Emilio Segre et al. *Experimental nuclear physics. volume I*. New York : John Wiley & sons ; London : Chapman & Hall, cop. 1953., 1953, p. 253.

[23]   OB Tarasov and D Bazin. "LISE++: Radioactive beam production with in-flight separators". In: *Nuclear Instruments and Methods in Physics Research Section B: Beam Interactions with Materials and Atoms* 266.19-20 (2008), pp. 4657–4664.

[24]   James F Ziegler, Matthias D Ziegler, and Jochen P Biersack. "SRIM–The stopping and range of ions in matter". In: *Nuclear Instruments and Methods in Physics Research Section B: Beam Interactions with Materials and Atoms* 268.11-12 (2010), pp. 1818–1823.

[25]   BB Wiggins et al. "Development of a compact E× B microchannel plate detector for beam imaging". In: *Nuclear Instruments and Methods in Physics Research Section A: Accelerators, Spectrometers, Detectors and Associated Equipment* 866 (2017), pp. 202–206.

[26]   Joseph Ladislas Wiza et al. "Microchannel plate detectors". In: *Nucl. Instrum. Methods* 162.1-3 (1979), pp. 587–601.

[27]   R Schneider and A Stolz. *Technical Manual Ionization Chamber MUSIC80*. Tech. rep. Tech. Rep.(Technische Universität München, 2000), 2000.

[28]   O Bunemann, TE Cranshaw, and JA Harvey. "Design of grid ionization chambers". In: *Canadian journal of research* 27.5 (1949), pp. 191–206.

[29]   S.F. Biagi. "Monte Carlo simulation of electron drift and diffusion in counting gases under the influence of electric and magnetic fields". In: *Nuclear Instruments and Methods in Physics Research Section A: Accelerators, Spectrometers, Detectors and Associated Equipment* 421.1 (1999), pp. 234–240. ISSN: 0168-9002. DOI: `https://doi.org/10.1016/S0168-9002(98)01233-9`. URL: `https://www.sciencedirect.com/science/article/pii/S0168900298012339`.

[30]   G. F. Reinking, L. G. Christophorou, and S. R. Hunter. "Studies of total ionization in gases/mixtures of interest to pulsed power applications". In: *Journal of Applied Physics* 60.2 (1986), pp. 499–508. DOI: `10.1063/1.337792`. eprint: `https://doi.org/10.1063/1.337792`. URL: `https://doi.org/10.1063/1.337792`.

[31]   AA Sonzogni. "NuDat 2.0: Nuclear structure and decay data on the internet". In: *AIP Conference Proceedings*. Vol. 769. American Institute of Physics. 2005, pp. 574–577.

[32]   S. Agostinelli et al. "Geant4—a simulation toolkit". In: *Nuclear Instruments and Methods in Physics Research Section A: Accelerators, Spectrometers, Detectors and Associated Equipment* 506.3 (2003), pp. 250–303. ISSN: 0168-9002. DOI: `https://doi.org/10.1016/S0168-9002(03)01368-8`. URL: `https://www.sciencedirect.com/science/`

article/pii/S0168900203013688.

[33]   J. Allison et al. "Geant4 developments and applications". In: *IEEE Transactions on Nuclear Science* 53.1 (2006), pp. 270–278. DOI: `10.1109/TNS.2006.869826`.

[34]   J. Allison et al. "Recent developments in Geant4". In: *Nuclear Instruments and Methods in Physics Research Section A: Accelerators, Spectrometers, Detectors and Associated Equipment* 835 (2016), pp. 186–225. ISSN: 0168-9002. DOI: `https://doi.org/10.1016/j.nima.2016.06.125`. URL: `https://www.sciencedirect.com/science/article/pii/S0168900216306957`.

[35]   C Scheidenberger et al. "Charge states of relativistic heavy ions in matter". In: *Nuclear Instruments and Methods in Physics Research Section B: Beam Interactions with Materials and Atoms* 142.4 (1998), pp. 441–462. ISSN: 0168-583X. DOI: `https://doi.org/10.1016/S0168-583X(98)00244-4`. URL: `https://www.sciencedirect.com/science/article/pii/S0168583X98002444`.

[36]   Y. Giomataris et al. "MICROMEGAS: a high-granularity position-sensitive gaseous detector for high particle-flux environments". In: *Nuclear Instruments and Methods in Physics Research Section A: Accelerators, Spectrometers, Detectors and Associated Equipment* 376.1 (1996), pp. 29–35. ISSN: 0168-9002. DOI: `https://doi.org/10.1016/0168-9002(96)00175-1`. URL: `https://www.sciencedirect.com/science/article/pii/0168900296001751`.

[37]   M. Cortesi et al. "Multi-layer thick gas electron multiplier (M-THGEM): A new MPGD structure for high-gain operation at low-pressure". In: *Review of Scientific Instruments* 88.1 (2017), p. 013303. DOI: `10.1063/1.4974333`.

[38]   Walter Blum, Werner Riegler, and Luigi Rolandi. *Particle detection with Drift Chambers*. Springer, 2010.

[39]   Emanuel Pollacco et al. "GET: A Generic Electronic System for TPCs for Nuclear Physics Experiments". In: *Physics Procedia* 37 (2012). Proceedings of the 2nd International Conference on Technology and Instrumentation in Particle Physics (TIPP 2011), pp. 1799–1804. ISSN: 1875-3892. DOI: `https://doi.org/10.1016/j.phpro.2012.02.506`. URL: `https://www.sciencedirect.com/science/article/pii/S1875389212018974`.

[40]   M. Al-Turany and et al. *Fairroot*. URL: `https://fairroot.gsi.de/`.

[41]   fuhlig1 et al. *FairRootGroup/FairRoot: v18.8.1*. Version v18.8.1. Feb. 2023. DOI: `10.5281/zenodo.7674922`. URL: `https://doi.org/10.5281/zenodo.7674922`.

[42]   Rene Brun et al. *root-project/root: v6.18/02*. Version v6-18-02. Aug. 2019. DOI: `10.5281/zenodo.3895860`. URL: `https://doi.org/10.5281/zenodo.3895860`.

[43]   R. Brun and F. Rademakers. "ROOT: An object oriented data analysis framework". In:

Nucl. Instrum. Meth. A 389 (1997). Ed. by M. Werlen and D. Perret-Gallix, pp. 81–86. DOI: `10.1016/S0168-9002(97)00048-X`.

[44] R. Brun et al. "GEANT3". In: (Sept. 1987).

[45] I. Hrivnacova et al. *The Virtual Monte Carlo*. 2003. arXiv: `cs/0306005 [cs.SE]`.

[46] OB Tarasov and D Bazin. "LISE++: Exotic beam production with fragment separators and their design". In: *Nuclear Instruments and Methods in Physics Research Section B: Beam Interactions with Materials and Atoms* 376 (2016), pp. 185–187.

[47] Glenn F. Knoll. *Radiation detection and measurement*. Wiley, 2010.

[48] J. Giovinazzo et al. "GET electronics samples data analysis". In: *Nuclear Instruments and Methods in Physics Research Section A: Accelerators, Spectrometers, Detectors and Associated Equipment* 840 (2016), pp. 15–27. ISSN: 0168-9002. DOI: `https://doi.org/10.1016/j.nima.2016.09.018`. URL: `https://www.sciencedirect.com/science/article/pii/S0168900216309408`.

[49] T. Zerguerras et al. "Understanding avalanches in a Micromegas from single-electron response measurement". In: *Nuclear Instruments and Methods in Physics Research Section A: Accelerators, Spectrometers, Detectors and Associated Equipment* 772 (2015), pp. 76–82. ISSN: 0168-9002. DOI: `https://doi.org/10.1016/j.nima.2014.11.014`. URL: `https://www.sciencedirect.com/science/article/pii/S0168900214012789`.

[50] *What FFTW Really Computes*. URL: `https://www.fftw.org/fftw3_doc/The-1d-Real_002ddata-DFT.html`.

[51] Wikiwald. *Butterworth filter — Wikipedia, The Free Encyclopedia*. [Online; accessed 7-April-2023]. 2023. URL: `https://en.wikipedia.org/wiki/Butterworth_filter`.

[52] J.S. Randhawa et al. "Beam-induced space-charge effects in time projection chambers in low-energy nuclear physics experiments". In: *Nuclear Instruments and Methods in Physics Research Section A: Accelerators, Spectrometers, Detectors and Associated Equipment* 948 (2019), p. 162830. ISSN: 0168-9002. DOI: `https://doi.org/10.1016/j.nima.2019.162830`. URL: `https://www.sciencedirect.com/science/article/pii/S0168900219312641`.

[53] P Baille et al. "Effective collision frequency of electrons in noble gases". In: *Journal of Physics B: Atomic and Molecular Physics* 14.9 (May 1981), p. 1485. DOI: `10.1088/0022-3700/14/9/013`. URL: `https://dx.doi.org/10.1088/0022-3700/14/9/013`.

[54] T. Cover and P. Hart. "Nearest neighbor pattern classification". In: *IEEE Transactions on Information Theory* 13.1 (1967), pp. 21–27. DOI: `10.1109/TIT.1967.1053964`.

[55] P. V. C. Hough. "Machine Analysis of Bubble Chamber Pictures". In: *Conf. Proc. C* 590914 (1959). Ed. by L. Kowarski, pp. 554–558.

[56] Linda G. Shapiro and George C. Stockman. *Computer vision*. Prentice Hall, 2001.

[57] Christoph Dalitz, Jens Wilberg, and Lukas Aymans. "Triplclust: An algorithm for curve detection in 3D point clouds". In: *Image Processing On Line* 9 (2019), pp. 26–46. DOI: `10.5201/ipol.2019.234`.

[58] Martin A. Fischler and Robert C. Bolles. "Random Sample Consensus: A Paradigm for Model Fitting with Applications to Image Analysis and Automated Cartography". In: *Commun. ACM* 24.6 (1981), pp. 381–395. ISSN: 0001-0782. DOI: `10.1145/358669.358692`. URL: `https://doi.org/10.1145/358669.358692`.

[59] Radu Bogdan Rusu and Steve Cousins. "3D is here: Point Cloud Library (PCL)". in: *IEEE International Conference on Robotics and Automation (ICRA)*. Shanghai, China, 2011.

[60] Yassid Ayyad et al. "Novel particle tracking algorithm based on the Random Sample Consensus Model for the Active Target Time Projection Chamber (AT-TPC)". in: *Nuclear Instruments and Methods in Physics Research Section A: Accelerators, Spectrometers, Detectors and Associated Equipment* 880 (2018), pp. 166–173. ISSN: 0168-9002. DOI: `https://doi.org/10.1016/j.nima.2017.10.090`. URL: `https://www.sciencedirect.com/science/article/pii/S0168900217311798`.

[61] J.C. Zamora and G.F. Fortino. "Tracking algorithms for tpcs using consensus-based robust estimators". In: *Nuclear Instruments and Methods in Physics Research Section A: Accelerators, Spectrometers, Detectors and Associated Equipment* 988 (2021), p. 164899. DOI: `10.1016/j.nima.2020.164899`.

[62] R. E. Kalman. "A New Approach to Linear Filtering and Prediction Problems". In: *Journal of Basic Engineering* 82.1 (Mar. 1960), pp. 35–45. ISSN: 0021-9223. DOI: `10.1115/1.3662552`. eprint: `https://asmedigitalcollection.asme.org/fluidsengineering/article-pdf/82/1/35/5518977/35\_1.pdf`. URL: `https://doi.org/10.1115/1.3662552`.

[63] Noori Shirazi, Amir and Fleck, Ivor. "Bivariate normal distribution for finding inliers in Hough space for a Time Projection Chamber". In: *EPJ Web Conf.* 150 (2017), p. 00010. DOI: `10.1051/epjconf/201715000010`. URL: `https://doi.org/10.1051/epjconf/201715000010`.

[64] Amir Noori Shirazi. "Track reconstruction for InGrid Chips for a Time Projection Chamber". PhD thesis. 2018. URL: `https://www.hep.physik.uni-siegen.de/pubs/diss/shirazi-dr.pdf`.

[65] *Weighted arithmetic mean*. 2022. URL: `https://en.wikipedia.org/wiki/Weighted_`

`arithmetic_mean#Weighted_sample_variance`.

[66]   *Statistics*. URL: `https://www.gnu.org/software/gsl/doc/html/statistics.html#weighted-samples`.

[67]   D. H. D. West. "Updating Mean and Variance Estimates: An Improved Method". In: *Commun. ACM* 22.9 (1979), pp. 532–535. ISSN: 0001-0782. DOI: `10.1145/359146.359153`. URL: `https://doi.org/10.1145/359146.359153`.

[68]   George R. Price. "Extension of covariance selection mathematics". In: *Annals of Human Genetics* 35.4 (1972), pp. 485–490. DOI: `https://doi.org/10.1111/j.1469-1809.1957.tb01874.x`. eprint: `https://onlinelibrary.wiley.com/doi/pdf/10.1111/j.1469-1809.1957.tb01874.x`. URL: `https://onlinelibrary.wiley.com/doi/abs/10.1111/j.1469-1809.1957.tb01874.x`.

[69]   Student. "The Probable Error of a Mean". In: *Biometrika* 6.1 (1908), pp. 1–25. ISSN: 00063444. URL: `http://www.jstor.org/stable/2331554` (visited on 04/07/2023).

[70]   Ayyad, Y. et al. "Physics and technology of time projection chambers as active targets". In: *Eur. Phys. J. A* 54.10 (2018), p. 181. DOI: `10.1140/epja/i2018-12557-7`. URL: `https://doi.org/10.1140/epja/i2018-12557-7`.

[71]   "IEEE Standard Graphic Symbols for Logic Functions". In: *IEEE/ANSI 91/91a-1991* (1994).

[72]   URL: `https://docs.nscl.msu.edu/daq/newsite/home.php`.

[73]   Helmut Weick. *ATIMA*. version v1.41. Mar. 2021. URL: `http://web-docs.gsi.de/~weick/atima/`.

[74]   Wikipedia contributors. *Simpson's Rule*. [Online; accessed 24-May-2023]. 2023. URL: `%7Bhttps://en.wikipedia.org/wiki/Simpson%27s_rule%7D`.

[75]   V. E. Viola, K. Kwiatkowski, and M. Walker. "Systematics of fission fragment total kinetic energy release". In: *Phys. Rev. C* 31 (4 1985), pp. 1550–1552. DOI: `10.1103/PhysRevC.31.1550`. URL: `https://link.aps.org/doi/10.1103/PhysRevC.31.1550`.

[76]   J. R. Huizenga, R. Chaudhry, and R. Vandenbosch. "Helium-Ion-Induced Fission of Bi, Pb, Tl, and Au". In: *Phys. Rev.* 126 (1 Apr. 1962), pp. 210–219. DOI: `10.1103/PhysRev.126.210`. URL: `https://link.aps.org/doi/10.1103/PhysRev.126.210`.

[77]   Robert Vandenbosch and John R. Huizenga. *Nuclear fission*. Academic Press, 1973.

[78]   E. Prasad et al. "Systematics of the mass-asymmetric fission of excited nuclei from 176Os to 206Pb". In: *Physics Letters B* 811 (2020), p. 135941. ISSN: 0370-2693. DOI: `https://`

doi.org/10.1016/j.physletb.2020.135941. URL: https://www.sciencedirect.com/science/article/pii/S0370269320307449.

[79] M. R. Mumpower et al. "Primary fission fragment mass yields across the chart of nuclides". In: *Phys. Rev. C* 101 (5 May 2020), p. 054607. DOI: 10.1103/PhysRevC.101.054607. URL: https://link.aps.org/doi/10.1103/PhysRevC.101.054607.

[80] A. K. Anthony et al. "Beam particle identification and tagging of incompletely stripped heavy beams with HEIST". in: *Review of Scientific Instruments* 93.1 (Jan. 2022). 013306. ISSN: 0034-6748. DOI: 10.1063/5.0068180. eprint: https://pubs.aip.org/aip/rsi/article-pdf/doi/10.1063/5.0068180/16576488/013306_1_online.pdf. URL: https://doi.org/10.1063/5.0068180.